Phonon Dynamics of Ceramic $\mathbf{PbSc_{0.5}Ta_{0.5}O_3}$

by

Stephen Spencer
B.Sc. (Hons.) Memorial University of Newfoundland

A thesis submitted
in partial fulfillment of the
requirements for the degree of
Master of Science

Department of Physics and Physical Oceanography
Memorial University of Newfoundland
November 2016

St John's Newfoundland & Labrador

Abstract

This work aims to compare the optical and acoustic phonon properties between ceramic PST and previously studies crystalline PST, as such a study has never been performed. If easily fabricated ceramic PST has similar phonon properties to crystalline PST, it can serve the same purpose in industrial applications.

Inelastic light scattering experiments were performed on lead scandium tantalate to probe acoustic and optical phonons in the material. Brillouin scattering experiments were performed at room temperature using a 180° backscattering geometry. Two peaks were observed in spectra, at shifts of ∼25 GHz and ∼44 GHz, which were independent of angle of incidence. These peaks were determined to be due to the longitudinal and transverse bulk modes, respectively. Using the average frequencies of these peaks, the velocities of these modes were calculated, and subsequently elastic constants c_{11}, c_{44}, and c_{12} were calculated. Brillouin light scattering experiments performed on a lead scandium tantalate ceramic with a 40 nm aluminum coating yielded an additional Brillouin peak that was not observed in uncoated experiments which may be due to the Rayleigh surface mode.

Raman light scattering experiments were performed on lead scandium tantalate at room temperature and temperatures ranging from 200°C to 1200°C. Four Raman

peaks were observed at room temperature, at shifts of ∼45 cm^{-1}, ∼220 cm^{-1}, ∼350 cm^{-1}, and ∼825 cm^{-1}, the strongest of which determined to be due to an F_{2g} mode. At high temperatures, the intensity of the latter three peaks became significantly weaker, with the F_{2g} mode frequency increasing at temperatures ranging from 200°C to 550°C. At temperatures ranging from 550°C to 900°C, there was very little change in the position of the peaks between spectra. For temperatures above 900°, only the F_{2g} mode was observed. In these spectra, the peak frequency shift was higher, and its intensity significantly decreased compared to other high temperature spectra.

Acknowledgments

First and foremost, I'd like to thank my supervisor, Dr. Andrews, for giving me the opportunity to work with him on this project, as well as those we have worked on over the last several years. His guidance and patience have been invaluable throughout this work. I'd also like to thank him for never being strict on due dates or deadlines and letting me work at my own pace. I would also like to thank Dr. Clouter for allowing use of the Raman scattering apparatus, and teaching me how to operate it. Thanks to Dr. Whatmore for providing the samples used in these experiments, and for his guidance through e-mail correspondence over the last two years.

I would like to thank my parents for their unwavering support throughout my academic career. Thank you for packing leftovers for me, thank you for being understanding, and thank you for trying to understand what I'm working on.

I would like to also like to thank my fellow graduate students, Tyler and Chris, for being such great friends. Thanks for the coffee runs, the chats, the help in classes, and for making me feel like less of a slacker (by being equally slack). You guys seriously made it easier to come in day after day.

Finally I would like to thank Taylor. Thank you for always supporting me, thank you for being so understanding, thank you for listening to me, and most of all thank

you for being there for me when I needed it most. You've done more for me than you could ever know. I doubt I could have made it through this without you at my side.

Contents

List of Tables

List of Figures

Chapter 1

Introduction

1.1 Lead Scandium Tantalate

Lead Scandium Tantalate, $PbSc_{\frac{1}{2}}Ta_{\frac{1}{2}}O_3$, (hereafter referred to as PST), is a perovskite-like ferroelectric crystal, following the perovskite-like structure $AB'_xB''_{1-x}O_3$ [1]. PST is typically observed in a cubic phase with atomic lattice spacing of $a_0 = 4.074$ Å at standard conditions [2], however PST exhibits rhombohedral symmetry at very low temperatures [3].

There is a coexistence of ferroelectric and magnetic phase transitions in PST [1, 3, 4, 5]. PST undergoes this first order ferroelectric phase transition at 286 K [6]. PST exhibits high electrostriction and a diffuse phase transition, where composition fluctuation leads to large fluctuation in the dielectric constant [7]. The random distribution of two crystallographically equivalent B site cations, Sc^{3+} and Ta^{5+}, is the cause of diffuse phase transitions, transitioning PST into its ferroelectric phase [5].

PST has gained increasing attention in recent years due to its applications in

capacitors, actuators, and pyroelectric detectors [8, 9].

One of the interesting characteristics of PST is its order-disorder properties; the presence or absence of some space group symmetry. Disorder in the material comes from interchangeability of the B-site cations, Sc^{3+} and Ta^{5+}. For a perfectly ordered crystal, where the order parameter $S = 1$, the position of the B-site cations within a unit cell is constant for all unit cells. As the material becomes disordered, and $S \rightarrow 0$, the positioning of the B-site cations differs between unit cells, becoming more random. A schematic showing the difference between ordered and disordered crystals is shown in Figure 1.1. Due to the size and charge of the B site cations, PST may be ordered or disordered upon fabrication [5]. The degree of order is determined from the occupation factor of Sc and Ta atoms [10] and may be characterized by Raman scattering and x-ray diffraction [5]. The ordering process is characterized by the appearance of superlattice peaks in XRD spectra due to doubling of the lattice parameter ($2a_0 \times 2a_0 \times 2a_0$) in the cubic cell [3, 5, 6].

Disorder is introduced by annealing PST at high temperatures, below the sintering temperature, typically around 1800 K, and the amount of disorder is determined by the annealing time [2, 11]. Once disorder has been obtained, PST may be cooled without transitioning back to order. This means that it is possible for PST to exist with different degrees of order at the same temperature [6, 12]. For example, consider two PST samples from the same parent crystal with the same order parameter S. Both samples are annealed at the same temperature for different times, such that the order parameter S is different for each sample. Both samples are cooled to room temperature at the same rate. After this process, these samples will maintain their disorder, and thus will have different order parameters at room temperature. From

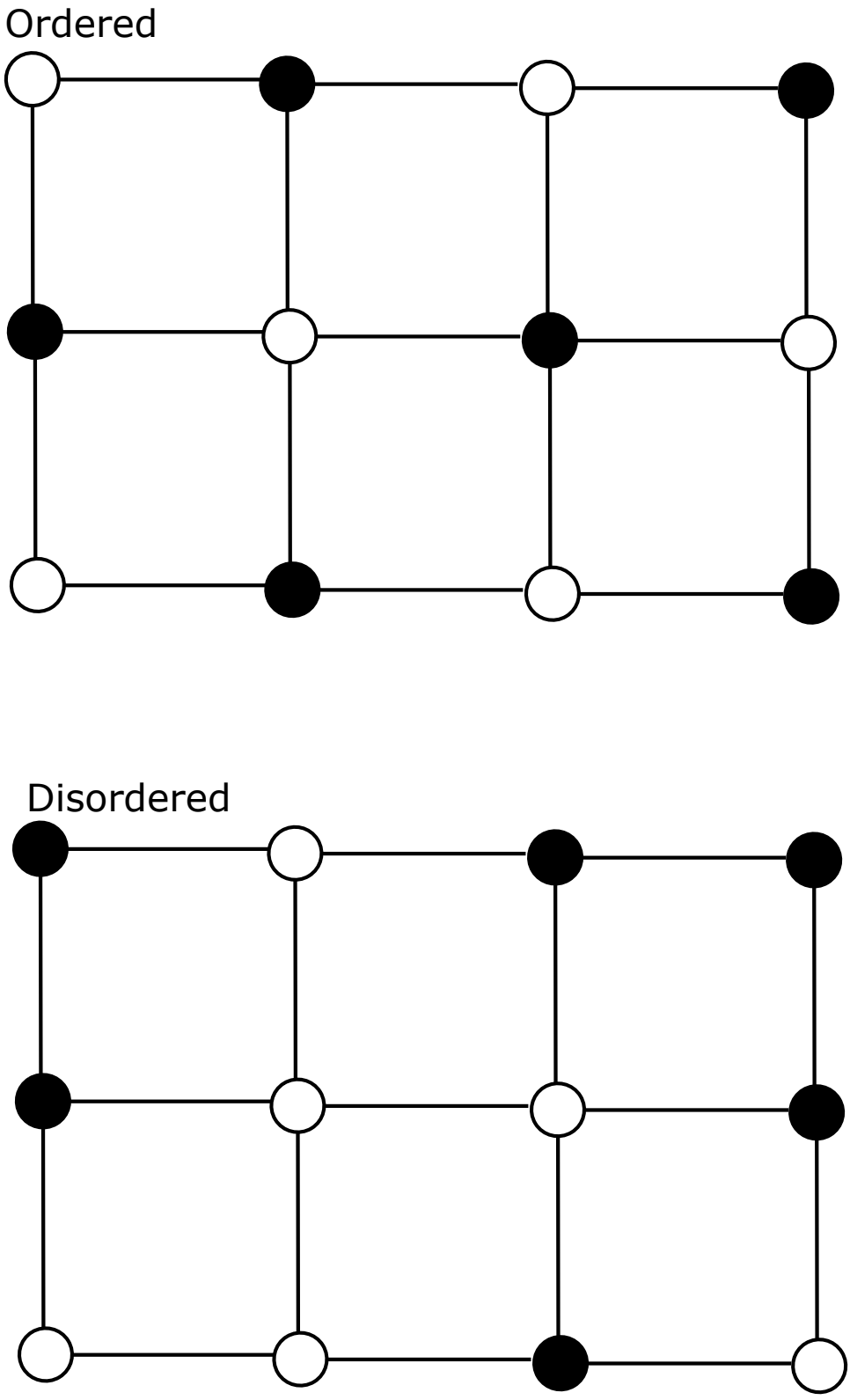

Figure 1.1: Schematic of ordered and disordered crystal cells in 2D. Black and white circles correspond to different B-site cations.

room temperature, a disordered crystal may be ordered by annealing at temperatures around 1200°C for long periods of time.

Ordered and disordered PST exhibit different properties. For example, disordered PST exhibits a diffuse phase transition near 270 K whereas ordered PST exhibits a discontinuous phase transition around 300 K [3, 13]. The phase transition temperature increases with increasing degree of order [14].

Samples of PST used in this study are polycrystalline ceramics. These ceramics are formed from sintering of crystalline powders. Polycrystalline ceramics consist of crystalline grains with different directionality. Due to the random directionality of the grains, these ceramics are isotropic in nature, and therefore light scattering experiments can be performed at any angle of incidence. Furthermore, it is not only the B-site cations that are disordered, but also the Pb and O atoms due to the random orientation of the polycrystalline grains that make up the ceramic.

Due to the interesting nature of order and disorder in PST, there have been several studies exploring these properties in PST. The degree of order in PST is commonly characterized by Raman scattering or x-ray diffraction. In the following studies, these techniques were used to characterize PST during ordering and disordering processes.

In a study by Stenger *et al*, the ordering of trivalent (Sc^{3+}) and pentavalent (Ta^{5+}) ions was observed in PST [2, 15]. Using x-ray diffraction at room temperature, Stenger *et al*. showed that PST exhibited cubic symmetry, even after annealing at ∼1000 °C. From x-ray diffraction, superstructural lines (weak diffraction peaks between stronger peaks due to an additional structure superimposed into the crystalline structure) were observed on the onset of ordering of Sc^{3+} and Ta^{5+}, increasing in intensity with annealing time. Stenger *et al*. observed the coexistence of ordered and disordered

regions. PST was partly ordered at 1450 °C and disordered at 1500 °C, suggesting that the order-disorder temperature is somewhere in between.

Similar to Stenger *et al.* [2, 15], Setter *et al.* [11] used x-ray diffraction to observe order-disorder phenomena in PST crystals, ceramics, and powders. Disorder was introduced into PST samples by heating samples between 1400 °C and 1560 °C. This produced superlattice reflections in x-ray diffraction corresponding to half-integer spacing of the disordered structure. For disordered PST, the (111) and (311) superlattice peaks were significantly stronger in intensity than the fundamental peaks.

Wang *et al.* [5] observed the ordering and disordering processes of PST crystals and ceramics. These processes were characterized quantitatively by x-ray diffraction and qualitatively by Raman spectroscopy. In this study, as-grown PST crystals showed a large degree of order, with the order parameter S ranging from 0.6 - 0.8, varying between the surface and the bulk. For ordering PST ceramics, very long annealing times were required at temperatures ranging from 1000°C - 1300°, and higher annealing temperatures, with very low lead loss in the samples. Wang *et al.* observed a sharpening of the peak at 355 cm^{-1} as the sample became more ordered.

From the results provided by Wang *et al.* [5], PST calcinated powder normally has a high degree of order. Wang suggests that order is more easily obtained in PST crystals grown at low temperatures due to this high degree of order. As with the ceramics, the degree of order measured varied from the surface to the interior of the samples. Finally, Wang *et al.* concluded that ceramics with lower vacancy content required higher annealing temperatures and longer times for ordering. This means that samples with weight loss are ordered more easily; lead vacancies aid in B-site reorientation. Furthermore, oxygen vacancies also aid in B-site reorientation. PST

ceramics with nearly zero lead loss require extremely high temperatures for ordering.

1.2 Brillouin Light Scattering on Lead Scandium Tantalate

Though PST has garnered more attention in recent years, there are very few studies of elastic properties that have been performed. In fact, there have been only four Brillouin scattering studies performed on PST, and of these, none were on ceramic PST. The four Brillouin scattering studies that have been completed are described below.

In a study by Jiang *et al.* [16], Brillouin light scattering experiments were performed on disordered [001] PST platelets at temperatures ranging from 83 K - 873 K. In this study, the only observed acoustic phonons were longitudinal bulk modes. Data for longitudinal mode frequency shift was plotted against temperature and showed a minimum in Brillouin shift at 245 K. This minimum in frequency shift coincided with a maximum in Brillouin peak width, and a sharp maximum in dielectric constant at this temperature. From this, Jiang *et al.* determined the relationship between elastic constant c_{33} and temperature. The room temperature value for longitudinal phonon velocity was 4.33×10^3 m/s in the [001] direction, and the corresponding value of c_{33} is $17.3 \times 10^{10}\mathrm{N/m^2}$.

The central peak of the Brillouin spectrum of [100] oriented PST crystals was examined by Lushnikov *et al.* [17] for temperatures ranging from 80 K - 500 K. In this work, it was determined that the central peak of the Brillouin spectrum consisted of at least two parts. The first component was attributed to elastic light

scattering, and the other components due to quasielastic light scattering from the crystal. Lushnikov *et al*. also observed a longitudinal bulk mode peak at 45.76 GHz, and an additional feature, the shape of which can be described by the Voigt function at 16 GHz. Longitudinal peak intensity increased with increasing temperature up to 290 K, where there was a sharp anomalous spike. At 290 K, full width at half maximum of this peak exhibited an anomalously low value. At temperatures greater than 290 K, peak intensity decreased with increasing temperature as full width at half maximum increased.

Fedoseev *et al*. [1] performed Brillouin scattering experiments on PST crystals in a temperature range of 80 - 500 K. For all spectra collected with an incident light wave vector parallel to the [100] direction of the crystal, only longitudinal acoustic modes were observed at ∼45 GHz. For experiments with the incident light wave vector parallel to the [111] direction, quasi-longitudinal and quasi-transverse acoustic modes were observed at ∼ 45 GHz and ∼25 GHz. There were no surface modes observed in these experiments. Fedoseev *et al*. plotted bulk phonon velocity, full width at half maximum, and integrated intensity against temperature. The velocity of the phonons studied varied smoothly over the wide temperature range, showing a minimum at 280 K. Full width at half maximum and integrated intensity of the bulk mode peak showed weak anomalies at 297 K. Fedoseev *et al*. compared their results to data collected for lead magnesium niobate, PMN, another relaxor ferroelastic crystal. Both materials showed similar temperature dependence of elastic constants c_{11} and c_{44}, whereas the behavior of elastic constant c_{12} was qualitatively different. Where PMN shows a maximum in c_{12} near the diffuse phase transition, PST shows a minimum.

Brillouin light scattering experiments were performed on highly disordered PST

by Pietraszko *et al*. [10]. These experiments were performed at room temperature on a PST platelet with a [111] orientation. Unlike Fedoseev *et al*. [1], these experiments only found peaks due to longitudinal bulk modes. There were no transverse bulk or surface modes present in Brillouin spectra. The Brillouin frequency shift of the longitudinal acoustic mode was recorded to be 44.8 GHz, and consequently its velocity was calculated to be 4742 m/s. Pietraszko *et al*. also reported a room temperature elastic constant of $c_{[111]} = c_{11} + 2c_{12} + 4c_{44} = 203$ GPa.

1.3 Raman Light Scattering on Lead Scandium Tantalate

Although Raman scattering is a useful tool for characterizing the degree of order of PST, there have been very few Raman scattering studies performed on PST. Bismayer *et al*. [14] performed Raman spectroscopy experiments over a temperature range of 102 K - 873 K. These experiments were performed on both ordered and disordered PST. Ordering was obtained by annealing at 975 K over several hours, while disordering was obtained by annealing at 1650 K for 20 minutes while preventing significant Pb loss. In the Raman spectra for the high temperature phase of ordered PST, there were four prominent bands present, with shifts of 61 cm^{-1}, 240 cm^{-1}, 370 cm^{-1}, and 830 cm^{-1}. There were also two weak bands near 150 cm^{-1} and 540 cm^{-1}. Bismayer plotted the variation of the integrated intensity, full width at half maximum, and squared frequency of the 61 cm^{-1} peak as a function of temperature. In the range of 102 K - 305 K, the squared frequency of the 61 cm^{-1} peak decreased linearly with temperature. At higher temperatures, the squared frequency and integrated intensity

of this peak was found to be independent of temperature.

Mihailova *et al.* performed polarized Raman scattering experiments on PST and PMN crystals at temperatures ranging from 160 K - 490 K [18]. Using group theory, Mihailova identified all Raman active and IR active modes in PST and PMN. Raman scattering experiments were done and peaks due to all Raman modes were identified in spectra.

In a subsequent study by Setter *et al.* B-site ordering was observed in PST samples using Raman scattering techniques [19]. By comparing their Raman scattering results to XRD spectra, it was determined that the peaks found in Raman spectra are not all equally affected by disorder. Furthermore, it was observed that the intensity of the Raman peak occurring at 365 cm^{-1} decreased with B-site disorder. The linewidth of the 365 cm^{-1} peak was considered the Raman order parameter for PST in this study.

In an experimental study by Mihailova *et al.* XRD and polarized Raman spectroscopy were performed on PST crystals and powders [20]. Modes observed in Raman spectra varied between parallel polarization and cross polarization [20]. Four modes were found in parallel polarization, located at 53 cm^{-1}, 77 cm^{-1}, 240 cm^{-1}, and 830 cm^{-1}, whereas three peaks were found in the cross-polarized spectra, located at 300 cm^{-1}, 355 cm^{-1}, and 830 cm^{-1}. The lowest frequency peak in the parallel polarized spectra was determined to be due to the F_{2g} mode in PST. This peak became weaker in intensity with increasing temperature, as this mode is involved with the structural phase transition at low temperatures. Furthermore, it was shown that the intensity of the mode found at 240 cm^{-1} decreases rapidly with increasing temperature.

As a complement to their Brillouin scattering experiments, Lushnikov *et al.* [17] performed Raman scattering experiments on PST at temperatures ranging from 80

K - 500 K. As with their Brillouin scattering work, they observed two components in the central peak of their Raman spectra, corresponding to elastic and quasielastic scattering. A peak was also observed in these spectra around 50 cm^{-1}. The intensity and full width at half maximum of the 50 cm^{-1} peak increased with a decrease in temperature.

1.4 Motivation

PST has garnered an increasing amount of attention in recent years. Although there have been a small number of Brillouin scattering and Raman scattering studies on PST crystals, there have been no such studies on ceramic PST. With this work, we will compare the phonon behavior and elastic properties of ceramic PST with PST crystals at room temperature. Furthermore, although PST has been used as a thermal detector [8, 21], there have been no studies of optical phonon behaviour in PST in the high temperature regime. Therefore, Raman light scattering experiments were also performed at temperatures ranging from 200°C - 1200°C.

This work aims to compare the acoustic and optical phonon properties of ceramic and crystalline PST. While the motivation behind this work is primarily scientific, a greater understanding of the phonon dynamics in ceramic PST, and how it compares to that in its crystalline counterpart, can lead to industrial applications which have typically used crystals [8, 9]. If easily fabricated ceramics can serve the same purpose, large crystals will not need to be grown for industrial application.

1.5 Scope

The research presented in this thesis consisted of inelastic laser light scattering studies of ceramic PST. Brillouin spectroscopy was used to explore the elastic properties of ceramic PST at room temperature. Acoustic phonon frequencies found from Brillouin spectra were used to calculate phonon velocities, and subsequently elastic constants c_{11}, c_{12}, and c_{44}. Brillouin light scattering experiments were also carried out on a PST ceramic sample with a 40 nm aluminum coating in an attempt to identify surface acoustic modes. To date, surface modes have not been observed in PST crystals or ceramics. Raman spectroscopy experiments were also performed on PST ceramics at room temperature and high temperatures to investigate optical phonon behaviour over a wide range of temperatures.

Chapter 2

Theory

2.1 Phonon Dynamics

In a crystal lattice, atoms are constantly vibrating about their equilibrium positions. When atoms vibrate with the same frequency and phase as each other, the result is a phonon, called a normal mode [22]. To discuss normal modes, it is easiest to begin by considering a one dimensional chain of atoms.

Consider a chain of atoms, each of mass M, separated by springs with spring constant K and equilibrium distance a. The motion of this system is described by the equation

$$M\frac{\partial^2 u}{\partial t^2} = K(u^{m+1} - u^m) + K(u^{m-1} - u^m) = K(u^{m+1} - 2u^m + u^{m-1}) \tag{2.1}$$

where u^m is the displacement of the m^{th} atom with respect to its equilibrium position [23], given by

$$u^m = Ue^{ikma - i\omega t} \tag{2.2}$$

where U is a constant, k is the wave number, ω is the angular frequency, and t is time. By substituting Equation (2.2) into Equation (2.1), the solution for frequency is

$$\omega = 2\sqrt{\frac{K}{M}}\sin\left(\frac{ka}{2}\right). \tag{2.3}$$

The solution given by Equation (2.3) has two defining characteristics. First, for small values of k, ω is proportional to the absolute value of k. The slope of the dispersion curve in the low k region is $d\omega/dk = a\sqrt{K/M} = v$ [23], where v is the speed of phonon propagation in the material. The second characteristic of this solution is that it repeats periodically as a function of k, such that the period is equal to $2\pi/a$, the side length of the first Brillouin zone.

Expanding on the previous example, we now consider a diatomic chain of atoms with an ABAB pattern, with masses M_1 and M_2. The equations of motion for this system are

$$M_1\frac{\partial^2 u_1}{\partial t^2} = K(u_2^m - 2u_1^m - u_2^{m-1}) \tag{2.4}$$

$$M_2\frac{\partial^2 u_2}{\partial t^2} = K(u_1^{m+1} - 2u_2^m + u_1^m). \tag{2.5}$$

Since there are now two equations of motion, there are two solutions for frequency. These solutions are given by [23]

$$\omega(k) = \sqrt{K}\sqrt{\frac{M_1 + M_2 \pm \sqrt{M_1^2 + 2M_1M_2\cos(ka) + M_2^2}}{M_1M_2}}. \tag{2.6}$$

The solutions to Equation (2.6) are shown in Figure 2.1. The two solutions represent acoustic phonons and optical phonons, respectively. Acoustic phonons correspond to the low energy solution to Equation (2.6). Acoustic phonons occur when atoms

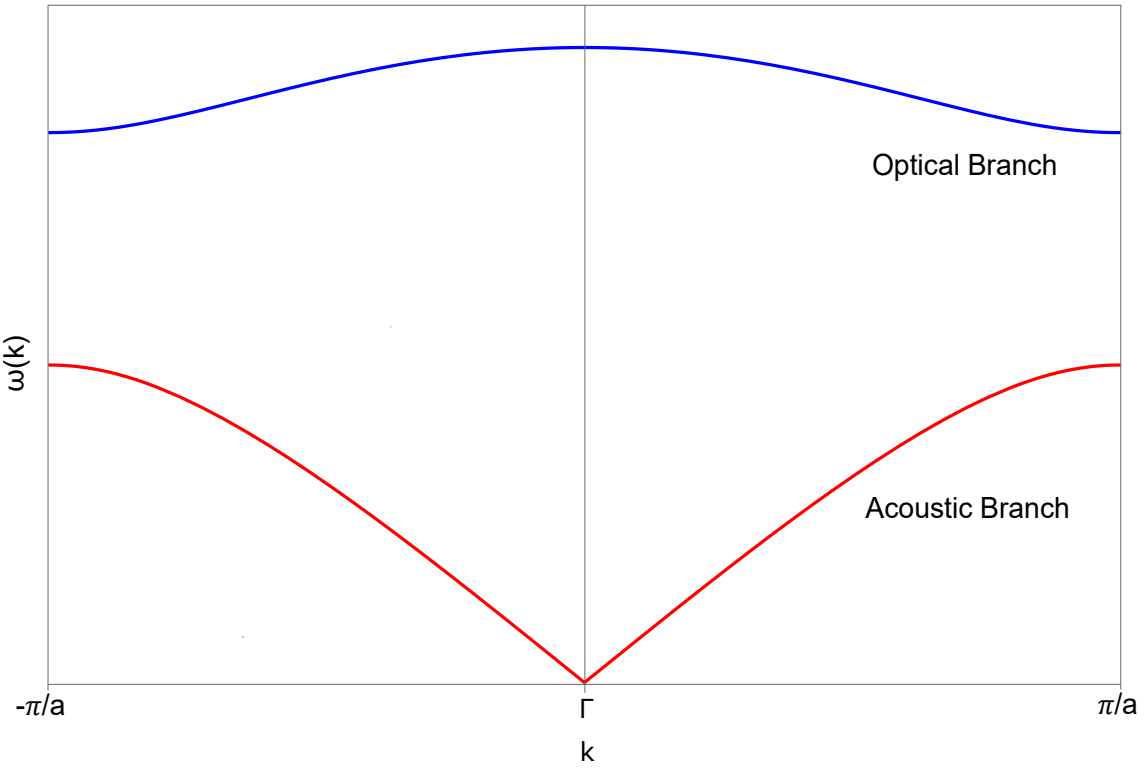

Figure 2.1: Phonon dispersion curves provided by Equation (2.6). Γ, $-\pi/a$, and π/a are the center and ends of the first Brillouin zone, respectively.

within a unit cell vibrate in unison with each other. As can be seen in Figure 2.1, the frequency of acoustic modes vanishes as k approaches zero. The high energy solution to Equation (2.6) corresponds to optical phonons. These occur when atoms within the unit cell vibrate out of phase with respect to each other.

When expanding this solution to three dimensions, there are $3n$ modes occurring in a given crystal [23], where n is the number of different atoms in a unit cell. Of the $3n$ modes, there are $3n - 3$ optical modes and 3 acoustic modes.

Provided $\lambda \gg a$, k is significantly smaller than the side length of the first Brillouin zone. When this condition is met, we may assume $k \simeq 0$, such is the case for Brillouin and Raman light scattering.

In inelastic light scattering, there are two types of scattering events which may occur. The first occurs when the incident photon generates a phonon in the material. In this process, the incident photon loses energy and momentum as it is scattered. This process is called Stokes scattering. The second scattering process is the opposite of the first. In this process, the incident photon annihilates a phonon in the material, thus increasing the energy and momentum of the photon as it is scattered. This is known as anti-Stokes scattering. These scattering events are illustrated in Figure 2.2.

2.2 Brillouin Spectroscopy

Brillouin spectroscopy is an inelastic light scattering technique which is used to probe thermally excited acoustic phonons in a material. Brillouin scattering is governed by

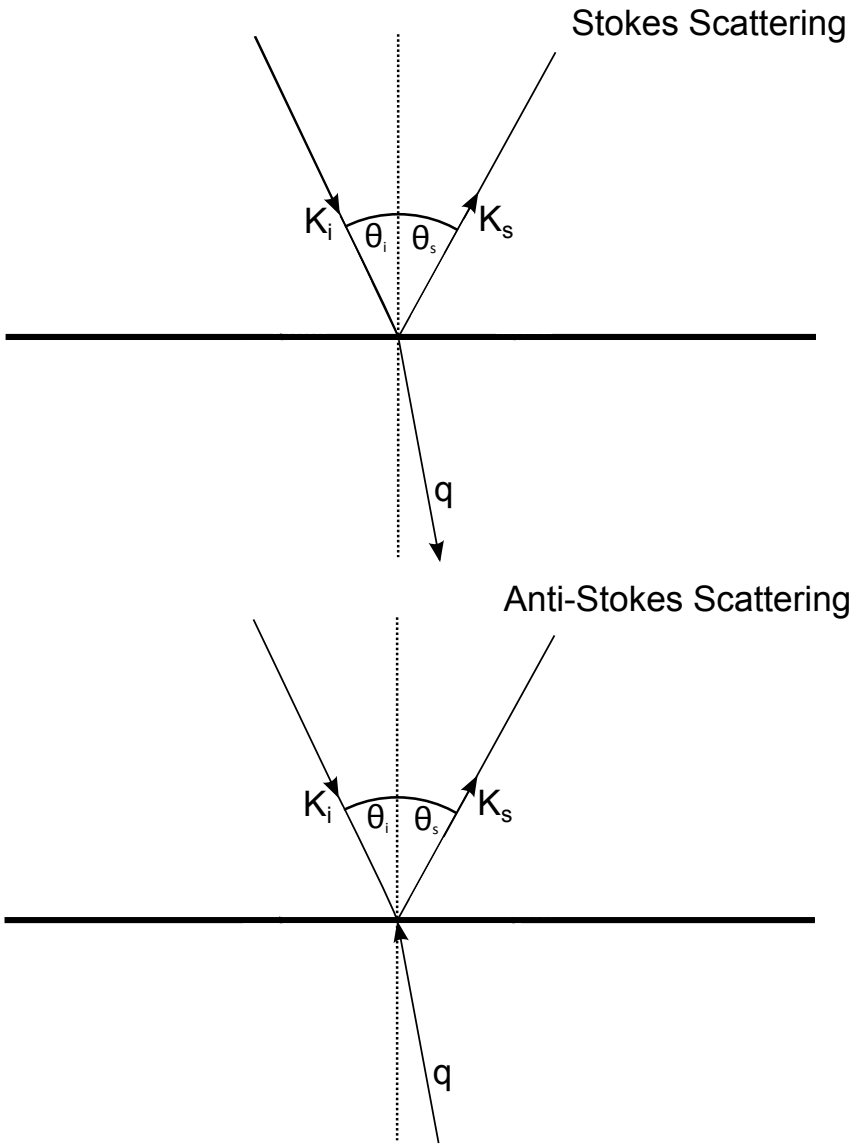

Figure 2.2: Schematic of Stokes and Anti-Stokes scattering mechanisms. K is the photon wave vector, θ is the angle of the incident light beam with respect to the surface normal, q is the phonon wave vector, and the subscripts i and s denote the incident and scattered photons, respectively.

conservation of energy and momentum [24], such that

$$\hbar\omega_s = \hbar\omega_i \pm \hbar\Omega \tag{2.7}$$

$$\hbar\vec{K}_s = \hbar\vec{K}_i \pm \hbar\vec{q} \tag{2.8}$$

where ω and $\vec{K}$ are photon angular frequency and wave vector, respectively, Ω and $\vec{q}$ are the angular frequency and wave vector of the phonon, respectively, and the subscripts i and s denote the incident and scattered light. The angular frequency of the phonon is given by

$$\Omega = 2\pi f = vq \tag{2.9}$$

where v is the speed of the phonon. Since v is significantly smaller than c, the speed of light, we can make the assumption that $\omega_s \simeq \omega_i$ and $k_s \simeq k_i$, where k_x is the magnitude of $\vec{K}_x$.

There are two types of phonons that can be probed by Brillouin scattering. The first process occurs in the bulk of the material, caused by fluctuations in the dielectric constant due to fluctuations in the strain field, represented by $\vec{q_B}$ in Figure 2.3. Bulk modes are described with components parallel and perpendicular to the surface of the sample. The magnitudes of the phonon wave vector components are given by

$$q_B^{\parallel} = n[k_i \sin\theta_i' + k_s \sin\theta_s'] \tag{2.10}$$

$$q_B^{\perp} = n[k_i \cos\theta_i' + k_s \cos\theta_s'] \tag{2.11}$$

where n is the refractive index of the material, and θ_i' and θ_s' are the incident and scat-

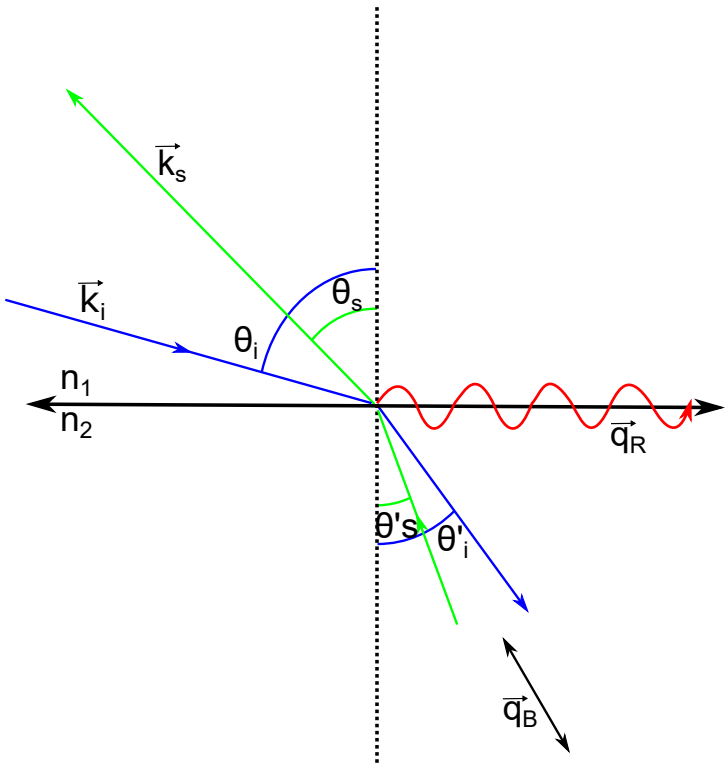

Figure 2.3: Diagram of vectors involved in Brillouin scattering process. $\vec{k_i}$ and $\vec{k_s}$ are the incident and scattered light wave vectors, θ_i, θ_s θ'_i, θ'_s are the external and internal incident and scattered light angles with respect to the normal of the sample, $\vec{q_B}$ is the wave vector of the acoustic bulk mode, and $\vec{q_R}$ is the wave vector of the Rayleigh surface mode.

tered angles of light in the material, governed by Snell's law. Combining Equations (2.10) and (2.11), the magnitude of the bulk phonons wave vector is

$$q_B = [(q_B^{\parallel})^2 + (q_b^{\perp})^2]^{\frac{1}{2}} = n[k_i^2 + k_s^2 + 2k_i k_s\{\sin\theta_i' \sin\theta_s' + \cos\theta_i' \cos\theta_s'\}]^{\frac{1}{2}}. \quad (2.12)$$

Remembering that $k_s \simeq k_i$, Equation [2.12] may be expressed as

$$q_B = n[2k_i^2\{1 + \sin\theta_i' \sin\theta_s' + \cos\theta_i' \cos\theta_s'\}]^{\frac{1}{2}}. \quad (2.13)$$

From here, it can be shown that

$$q_B = 2nk_i \cos\left(\frac{\theta_s' - \theta_i'}{2}\right). \quad (2.14)$$

In 180° backscattering, $\theta_s = \theta_i$, and consequently $\theta_s' = \theta_i'$, therefore $q_B = 2nk_i$. By applying Equation (2.9), and the fact that $k = \frac{2\pi}{\lambda}$, the frequency of a bulk mode can be expressed as

$$f_B = \frac{2nv_B}{\lambda_i} \quad (2.15)$$

where λ_i is the wavelength of the incident photon. By rearranging Equation (2.15), one can solve for the velocity of a bulk mode as

$$v_B = \frac{f_B \lambda_i}{2n}. \quad (2.16)$$

For isotropic media, such as those used in the present work, the frequency of a bulk mode does not depend on θ_i.

There are two types of bulk modes which may occur in a material. These are

transverse bulk modes, which may have two polarizations, and longitudinal bulk modes, which have one polarization.

The other type of phonon produced is a wave that propagates along the surface of the material, called the Rayleigh surface mode. The Rayleigh surface mode is caused by deformations on the sample surface, represented by $\vec{q_R}$ in Figure 2.3. These surface modes decay very rapidly into the bulk of the material, so the only component considered is that which is parallel to the surface of the material. The magnitude of the surface mode wave vector can therefore be expressed as just the parallel component, similar to Equation (2.10).

$$q_R = q_R^{\parallel} = k_i \sin\theta_i + k_s \sin\theta_s \tag{2.17}$$

Since $\theta_s = \theta_i$ in 180° backscattering, and $k_s \simeq k_i$, Equation (2.17) becomes

$$q_R = 2k_i \sin\theta_i. \tag{2.18}$$

The frequency of the Rayleigh surface mode is therefore given by

$$f_R = \frac{2v_R \sin\theta_i}{\lambda_i}. \tag{2.19}$$

Again, one may solve for the velocity of the surface mode as

$$v_R = \frac{f_R \lambda_i}{2\sin\theta_i}. \tag{2.20}$$

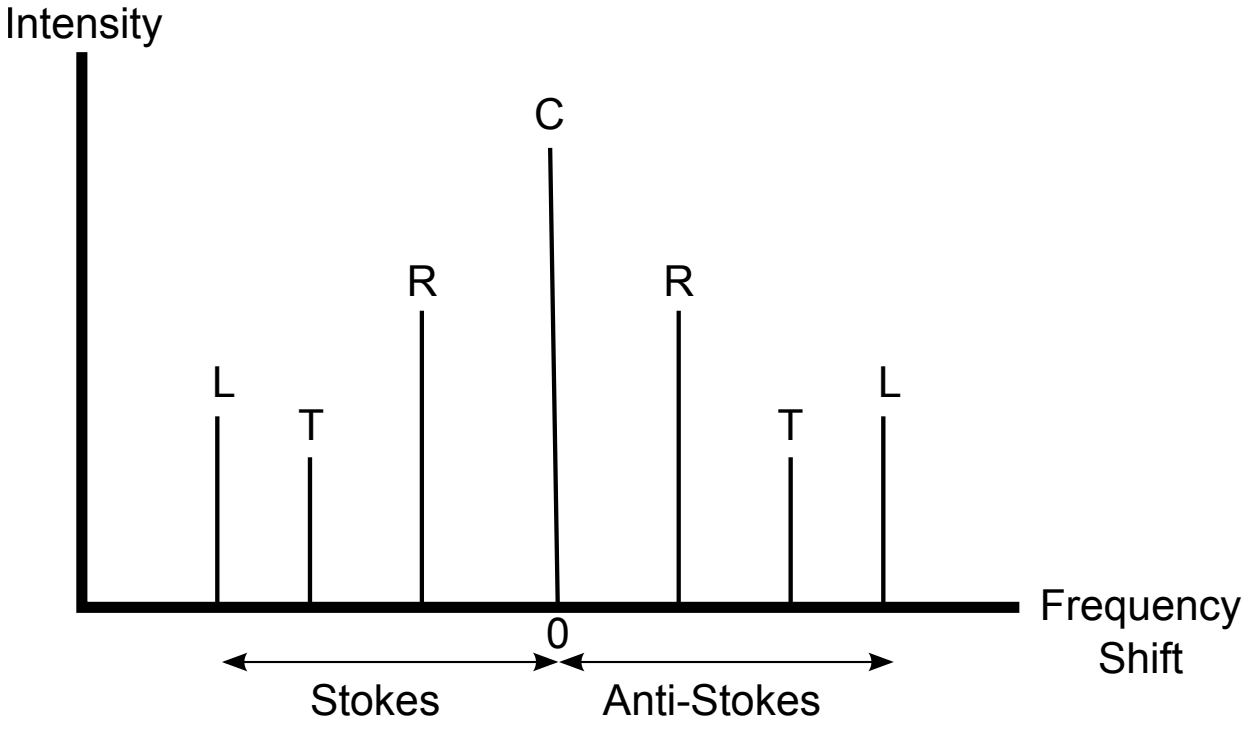

Figure 2.4: Schematic of a typical Brillouin spectrum. C is the central elastic peak, R is due to the Rayleigh surface mode, T is due to the transverse bulk mode, and L is due to the longitudinal bulk mode.

A typical Brillouin spectrum consists of peaks due to transverse bulk modes, longitudinal bulk modes, and surface modes. A simple schematic of a Brillouin spectrum is shown in Figure 2.4. The central peak occurs at the frequency of the incident laser, with an assigned shift of 0 GHz, and Brillouin peaks occur at frequencies on the order of tens of GHz shifted from the central peak. To the left of the central peak are the peaks caused by Stokes scattering, wherein a phonon is generated, and to the right of the central peak are the peaks corresponding to anti-Stokes scattering events, wherein a phonon is annihilated. In accordance with Equation (2.19), the frequency

shift of the surface mode, labeled as R in Figure 2.4, will shift with a change in angle of incidence. Since these experiments only occur at angles of incidence less than 90°, the frequency shift of the surface mode increases with increasing angle of incidence. The frequency shifts of peaks corresponding to the bulk modes, represented by T and L in Figure 2.4, are independent of angle of incidence. This is due to the isotropic nature of the PST ceramics.

2.3 Elastic Constants

In Brillouin scattering, the phonons that are probed have wavelengths that are significantly larger than the dimensions of the primitive unit cell, and can therefore be treated as sound waves in a continuous medium. As such, the general equation of motion for phonons is given by [25, 26]

$$\rho \frac{\partial^2 u}{\partial t^2} = \frac{\partial \sigma_{ij}}{\partial x_j} \tag{2.21}$$

where σ_{ij} is the second-rank stress tensor. The stress tensor is a product of the second-rank strain tensor s_{kl} and the fourth-rank elastic stiffness tensor C_{ijkl}, as

$$\sigma_{ij} = C_{ijkl} s_{kl}. \tag{2.22}$$

The components of the strain tensor s_{kl} are defined as

$$s_{kl} = \frac{1}{2}\left(\frac{\partial u_k}{\partial x_l} + \frac{\partial u_l}{\partial x_k}\right), \tag{2.23}$$

therefore Equation (2.21) becomes

$$\rho \frac{\partial^2 u}{\partial t^2} = C_{ijkl} \frac{\partial^2 u_k}{\partial x_j \partial x_l}. \tag{2.24}$$

We seek to obtain a plane wave solution for u, such that $u \sim e^{i(\vec{q}\cdot\vec{r}-\omega_q t)}$, which leads to a new solution for Equation (2.24)

$$\rho \omega_q^2 u_i = C_{ijkl} q_j q_l u_k. \tag{2.25}$$

Using $v_q = \omega_q / q$,

$$\rho v_q^2 u_i = C_{ijkl} \hat{q}_j \hat{q}_l u_k \tag{2.26}$$

giving an expression that relates bulk phonon velocity to the elastic stiffness tensor. Furthermore, since σ_{ij} and s_{kl} are symmetric, we may say $\sigma_i = C_{ij} s_j$, allowing us to express C_{ij} as a rank-two tensor. The form of the C_{ij} matrix for a cubic unit cell is given by Hayes [26], and contains only three elastic constants, c_{11}, c_{12}, and c_{44}.

$$C_{ij} = \begin{bmatrix} c_{11} & c_{12} & c_{12} & 0 & 0 & 0 \\ c_{12} & c_{11} & c_{12} & 0 & 0 & 0 \\ c_{12} & c_{12} & c_{11} & 0 & 0 & 0 \\ 0 & 0 & 0 & c_{44} & 0 & 0 \\ 0 & 0 & 0 & 0 & c_{44} & 0 \\ 0 & 0 & 0 & 0 & 0 & c_{44} \end{bmatrix} \tag{2.27}$$

By comparing Equations (2.26) and (2.27), we obtain expressions which relate phonon velocities to elastic constants in a cubic crystal. These expressions are shown in Table

Table 2.1: Relationship between bulk phonon velocity and elastic constant for the high symmetry directions of a cubic crystal.

q	$\rho\, v_q^2$	Bulk Mode
[100]	c_{11}	[100] Longitudinal
	c_{44}	[010] Transverse
	c_{44}	[001] Transverse
[110]	$\frac{1}{2}(c_{11} + c_{12} + 2c_{44})$	[110] Longitudinal
	$\frac{1}{2}(c_{11} - c_{12})$	$[1\bar{1}0]$ Transverse
	c_{44}	[001] Transverse
[111]	$\frac{1}{3}(c_{11} + 2c_{12} + 4c_{44})$	[111] Longitudinal
	$\frac{1}{3}(c_{11} - c_{12} + c_{44})$	$[1\bar{1}0]$ Transverse
	$\frac{1}{3}(c_{11} - c_{12} + c_{44})$	$[11\bar{2}]$ Transverse

2.1 for phonons propagating in high symmetry directions.

In a cubic crystal, the isotropy factor is given by

$$\eta = \frac{c_{11} - c_{12}}{2c_{44}}. \tag{2.28}$$

For an isotropic material, such as a ceramic, $\eta = 1$, therefore

$$c_{44} = \frac{c_{11} - c_{12}}{2}. \tag{2.29}$$

Using the expression in Table 2.1 and Equation (2.29), we now have equations to

describe all three elastic constants, as

$$c_{11} = \rho v_L^2 \tag{2.30}$$

$$c_{44} = \rho v_T^2 \tag{2.31}$$

$$c_{12} = c_{11} - 2c_{44} \tag{2.32}$$

where c_{11} and c_{44} are independent elastic constants.

2.4 Fabry-Perot Interferometry

The Fabry-Perot etalon (interferometer) is considered one of the best examples of an optical resonator. It consists of two parallel plane mirrors, of refractive index n, which are separated by a distance l and submerged in a medium of refractive index n'. A schematic of a Fabry-Perot interferometer is shown in Figure 2.5. To describe the interferometer, we must treat the mirror cavity as a transmission and reflection problem by considering an infinite number of partial waves caused by internal reflections [27].

Consider a plane wave incident on the Fabry-Perot etalon at an angle θ'. When the beam enters the mirror chamber, it undergoes multiple reflections until a partial wave exhibits the conditions for transmission. The phase delay between two partial waves is given by

$$\delta = \frac{4\pi n l \cos\theta}{\lambda} = 2k_x l \tag{2.33}$$

where λ is the wavelength of incident light, θ is the internal angle of incidence given by

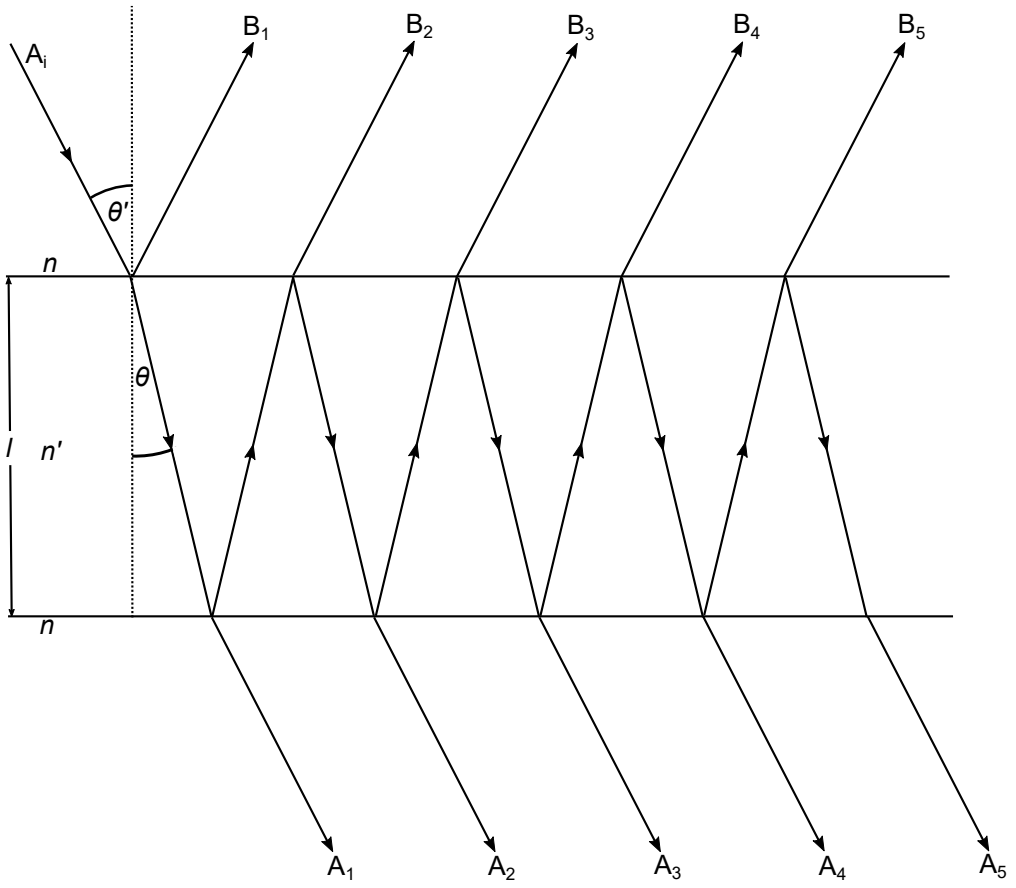

Figure 2.5: Schematic diagram of a Fabry-Perot interferometer.A_i is the amplitude of incident light beam, A_n are amplitudes of the transmitted partial waves, B_n are the amplitudes of the reflected partial waves, θ' and θ are the incident and refracted angles of light, n and n' are the refractive indicies of the mirrors and the medium, and l is the separation distance between the mirrors.

Snell's law, and k_x is the component of the incident light wave vector perpendicular to the surface of the mirrors. At normal incidence the phase delay simplifies to $\delta = 2kl$, where k is the incident wave vector.

To continue the example of multiple reflections, we must consider the change in light intensity throughout the reflections. Take the complex amplitude of the incident light beam to be A_i, as shown in Figure 2.5. The amplitudes of the partial reflections B_n are given by

$$B_1 = rA_i$$

$$B_2 = tt'r'A_i e^{-i\delta}$$

$$B_3 = tt'r'^3 A_i e^{-i2\delta}$$

$$B_4 = tt'r'^5 A_i e^{-i3\delta}$$

$$B_5 = tt'r'^7 A_i e^{-i4\delta} \cdots$$

where r and t are the reflection and transmission coefficients at the mirror interface, respectively, and r' and t' are the corresponding quantities within the mirror cavity. The total complex amplitude of reflected waves is the sum of the partial reflection

amplitudes, such that $A_r = B_1 + B_2 + B_3 + \cdots$, or

$$A_r = A_i[r + tt'r'e^{-i\delta}(1 + r'^2e^{-i\delta} + r'^4e^{-i2\delta} + r'^6e^{-i3\delta} + \cdots)]. \tag{2.34}$$

Similarly, the transmitted partial wave complex amplitudes, A_n, can be written as

$$A_1 = tt'A_ie^{-i\frac{\delta}{2}}$$

$$A_2 = tt'r'^2A_ie^{-i\delta}e^{-i\frac{\delta}{2}}$$

$$A_3 = tt'r'^4A_ie^{-i2\delta}e^{-i\frac{\delta}{2}}$$

$$A_4 = tt'r'^6A_ie^{-i3\delta}e^{-i\frac{\delta}{2}}$$

$$A_5 = tt'r'^8A_ie^{-i4\delta}e^{-i\frac{\delta}{2}}\cdots$$

where the term $e^{-i\frac{\delta}{2}}$ corresponds to a wave making a single traversal through the mirror cavity. As with the total complex amplitude of reflected light, the total complex amplitude of transmitted light, A_t, can be written as the sum of the partial

transmission complex amplitudes, giving $A_t = A_1 + A_2 + A_3 + \cdots$, or

$$A_t = tt' A_i e^{-i\frac{\delta}{2}}(1 + r'^2 e^{-i\delta} + r'^4 e^{-i2\delta} + r'^6 e^{-i3\delta} + r'^8 e^{-i4\delta} + \cdots). \tag{2.35}$$

The expressions for A_r and A_t are both in the form of a geometric series [28]. By using the fact that $r' = -r$, $R = r^2 = r'^2$, $T = tt'$, and $R + T = 1$ [29], Equations (2.34) and (2.35) may be expressed as

$$A_r = \frac{(1 - e^{-i\delta})\sqrt{R}}{1 - Re^{-i\delta}} A_i \tag{2.36}$$

$$A_t = \frac{Te^{-\frac{\delta}{2}}}{1 - Re^{-i\delta}} A_i. \tag{2.37}$$

The intensity of a beam of light is given by $I = AA^*$, therefore the ratios of reflected and transmitted light intensities are given by

$$\frac{I_r}{I_i} = \frac{A_r A_r *}{A_i A_i^*} = \frac{4R\sin^2(\frac{\delta}{2})}{(1-R)^2 + 4R\sin^2(\frac{\delta}{2})} \tag{2.38}$$

$$\frac{I_t}{I_i} = \frac{A_t A_t *}{A_i A_i^*} = \frac{(1-R)^2}{(1-R)^2 + 4R\sin^2(\frac{\delta}{2})}. \tag{2.39}$$

From Equations (2.38) and (2.39), it is clear that $I_r/I_i + I_t/I_i = 1$, or $I_r + I_t = I_i$. According to Equation (2.39), the transmission ratio becomes unity when $\delta = 2\pi m$, where m is any integer. Using Equation (2.33), the transmission condition becomes

$$\frac{4\pi nl\cos\theta}{\lambda} = 2\pi m \tag{2.40}$$

or

$$\lambda_m = \frac{2nl\cos\theta}{m}. \tag{2.41}$$

Knowing that $c = f\lambda$, the maximum transmission frequencies may be expressed as

$$f_m = m\frac{c}{2nl\cos\theta}. \tag{2.42}$$

When l and θ are fixed, the frequency interval between successive transmission maxima is given by

$$\delta f = f_{m+1} - f_m = \frac{c}{2nl\cos\theta}. \tag{2.43}$$

This is referred to as the free spectral range of the interferometer.

In the case of normal incidence, we may change the resonance frequency by changing the mirror separation of the Fabry-Perot, such that

$$\frac{df}{dl} = -\frac{\Delta f}{\lambda/2n} \tag{2.44}$$

where Δf is the intermode spacing. Therefore, by scanning over a range $dl < \lambda/2n$ we may scan over the range of wavelengths within the free spectral range. If we take $\delta f_{1/2}$ to be the separation between two frequencies at which the transmission is half its peak value, Equation (2.39) gives us

$$\sin^2\left(\frac{\delta_{1/2} - 2m\pi}{2}\right) = \frac{(1-R)^2}{4R} \tag{2.45}$$

where $\delta_{1/2}$ is the value of δ where the value of the denominator of Equation (2.39) is

$2(1-R)^2$. By assuming $\delta_{1/2} - 2m\pi \ll \pi$, we obtain

$$\Delta f = \frac{c}{2\pi nl\cos\theta}(\delta_{1/2} - 2m\pi) = \frac{c}{2\pi nl\cos\theta}\frac{1-R}{\sqrt{R}} \tag{2.46}$$

From Equation (2.46), we define the parameter

$$F = \frac{\pi\sqrt{R}}{1-R} \tag{2.47}$$

as the finesse of the Fabry-Perot interferometer. The finesse is a measure of the resolution of a Fabry-Perot interferometer. This is the ratio of the separation between peaks to the width of a transmission bandpass, as

$$\Delta f_{1/2} = \frac{c}{2nl\cos\theta F} = \frac{\Delta f}{F}. \tag{2.48}$$

Therefore, finesse can be expressed as

$$F = \frac{\Delta f}{\Delta f_{1/2}}. \tag{2.49}$$

2.5 Raman Spectroscopy

Raman spectroscopy is an inelastic light scattering technique which probes optical phonons in a material. This technique is commonly used for characterization of materials. There are several different Raman scattering techniques, such as resonance Raman spectroscopy, surface enhanced Raman spectroscopy (SERS), spontaneous Raman spectroscopy, and hyper-Raman spectroscopy. In Raman scattering, changes

in photon energy are recorded in wave numbers, with shifts on the order of ≥ 1 cm^{-1}.

As with Brillouin scattering, the incident photon may either annihilate an optical phonon (Stokes scattering) or generate an optical phonon (anti-Stokes scattering) [30]. These phonons are described as periodic functions of atomic displacement, given by

$$r = r_0 \cos(\omega_L t) \tag{2.50}$$

where r_0 is the amplitude of atomic vibration and ω_L is the vibrational frequency of atoms in the material.

In the classical model, the electric field of light is periodic, with angular frequency ω_i. This is given by the expression

$$E = E_0 \cos(\omega_i t) \tag{2.51}$$

where E_0 is the amplitude of the electric field. This incident electric field induces a dipole moment in the target material, as

$$P = \alpha E = \alpha E_0 \cos(\omega_i t) \tag{2.52}$$

where α is a second rank tensor known as the polarizability. The polarizability may be written as a linear function of r [30], such that

$$\alpha = \alpha_0 + \left(\frac{\partial \alpha}{\partial r}\right)_0 r + \cdots \tag{2.53}$$

where α_0 is the polarizability of the material at equilibrium and $\left(\frac{\partial \alpha}{\partial r}\right)_0$ is the rate of

change of the polarizability with respect to displacement, evaluated at equilibrium. By substituting Equation (2.50) into Equation (2.53), we obtain

$$\alpha = \alpha_0 + \left(\frac{\partial \alpha}{\partial r}\right)_0 r_0 \cos(\omega_L t). \tag{2.54}$$

In this equation, the higher order terms are treated as negligible.

With this information, the dipole moment of the material may now be expressed as

$$P = \alpha_0 E_0 \cos(\omega_i t) + \left(\frac{\partial \alpha}{\partial r}\right)_0 r_0 E_0 \cos(\omega_i t)\cos(\omega_L t). \tag{2.55}$$

The first term in this expression represents an oscillating dipole which radiates light with a frequency equal to that of the incident light. This corresponds to elastic light scattering. The second term in Equation (2.55) is the inelastic scattering expression. This second term yields the results of Raman scattering. Using the trigonometric identity

$$\cos(\theta)\cos(\phi) = \frac{1}{2}[\cos(\theta+\phi) + \cos(\theta-\phi)] \tag{2.56}$$

Equation (2.55) becomes

$$P = \alpha_0 E_0 \cos(\omega_i t) + \frac{1}{2}\left(\frac{\partial \alpha}{\partial r}\right)_0 r_0 E_0 \{\cos[(\omega_i - \omega_L)t] + \cos[(\omega_i + \omega_L)t]\}. \tag{2.57}$$

In the second term of the above expression, the component with $\cos[(\omega_i - \omega_L)t]$ corresponds to Stokes scattering and the component with $\cos[(\omega_i + \omega_L)t]$ corresponds to anti-Stokes scattering.

As can be seen from Equation (2.57), not all vibrations will be Raman active. Only vibrations where $(\partial\alpha/\partial r)_0 \neq 0$ are observed in Raman scattering.

In Raman scattering experiments, Stokes lines are typically more intense than anti-Stokes lines. This is due to the fact that the incident laser beam generates phonons in Stokes scattering. Naturally occurring optical phonons are much more rare, causing anti-Stokes lines to be significantly weaker. Because of this, Stokes lines are usually chosen to be examined.

Chapter 3

Experimental Details

3.1 Sample Preparation

PST ceramic samples were fabricated by Dr. Roger Whatmore using the second method discussed in the paper by Osbond and Whatmore [31]. This method involved initial formation of single-phase $ScTaO_4$ using a high-temperature wolframite, $(Fe,Mn)WO_4$, preparation stage. PST and lead-zirconate (PZ) powders were prepared separately using standard milling and calcination techniques, and were subsequently milled together. The combined powders were then calcinated at 900°C and hot pressed. The resulting ceramic was annealed between 1200°C - 1400°C, and cooled at a rate of 100°C/h. A photograph of the sample is shown in Figure 3.1. Two such samples were used in the present work.

One PST ceramic was coated with a 40 nm layer of aluminum and was used in Brillouin scattering experiments in an attempt to find surface modes in the material. Before deposition of aluminum film, the PST ceramic was cleaned by a four step

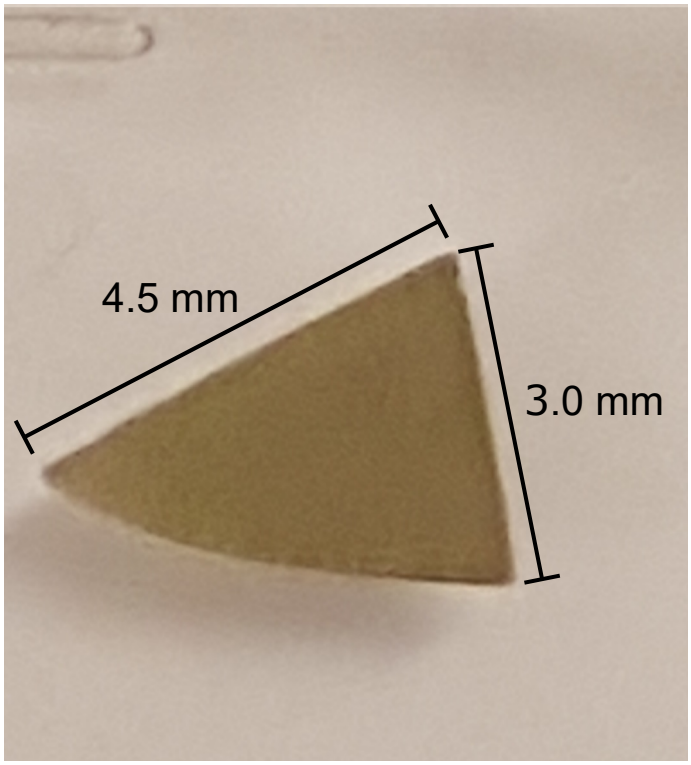

Figure 3.1: PST ceramic sample used in Brillouin scattering and Raman scattering experiments.

process. First, the ceramic sample was placed in a 10 minute ethanol bath, followed by 10 minute acetone bath. The sample was then scrubbed using a 5% volumetric solution of cleaner Decon 90. Finally, the ceramic was rinsed using deionized water. After cleaning, the ceramic was placed in the aluminum coating chamber.

The aluminum film was deposited onto the PST ceramic by Dr. Abdullah Alodhayb using a commercial DC magnetron sputtering system. The ceramic was placed on the substrate table, such that it was aligned with the Al target, located on the door of the chamber. A turbo pump, connected to the chamber, was used to evacuate the chamber. Aluminum deposition began once the chamber pressure was reduced to $\sim 10^{-6}$ torr. Deposition rate was measured by a quartz crystal monitor at a rate of ~ 1 Å/s, and thickness of the resulting aluminum film was 40 nm. Aluminum was chosen as it is inexpensive, has known deposition parameters, and has been previously shown to amplify surface mode peaks in Brillouin spectra collected for transparent materials [32]. Furthermore, a native oxide layer forming on aluminum would be very thin (on the order of a couple Å) and would thus not affect Brillouin scattering results.

3.2 Brillouin Scattering

3.2.1 Optical System

To collect room temperature spectra, PST samples were mounted directly into a Brillouin light scattering apparatus with a 180° backscattering geometry, shown in Figure 3.2. The light source used in these experiments was a Nd:YVO_4 solid state laser with a wavelength of 532 nm and output power of 2 W. As shown in Figure 3.2, the beam passed through variable neutral density filter V_1 to reduce beam power.

The beam then passed through half wave plate H which rotated the polarization of the beam 90°, such that the beam was polarized horizontally, before hitting beam splitter B. The reflected portion of the beam acted as the reference beam for the tandem Fabry-Perot interferometer. After being reflected by the beam splitter, this beam passed through aperture A which focused the beam onto mirror M_2. This mirror redirected the beam through variable density filter V_3, which allowed the power of the reference beam to be controlled. Finally, the reference beam passed through the reference pinhole of the tandem Fabry-Perot interferometer.

The beam transmitted through the beam splitter was reflected 90° by mirror M_1. This beam passed through filters F_1 and F_2 to further reduce beam power before passing through final variable neutral density filter V_2. After passing through V_2, the beam power was on the order of 10-100 mW. This beam was reflected 90° by prism P and focussed on the sample S by camera lens C, with a focal length of 5 cm. The camera lens was chosen due to its anti-reflectance coating and built-in adjustable aperture, set to f/2.8.

Scattered light was collected and collimated by the camera lens. Finally, the beam was focused onto the 450 μm diameter entrance pinhole of the tandem Fabry-Perot interferometer by lens L, with a focal length of 40 cm.

The scattered light was examined by a six-pass tandem Fabry-Perot interferometer manufactured by JRS Scientific Instruments. This interferometer contains two Fabry-Perot mirror chambers, shown in Figure 3.2.1, with slightly different mirror spacings.

Light entered the interferometer via the pinhole, as represented in Figure 3.2. Upon entry, mirrors M_1 and M_2 directed the beam through the first hole of aperture A_1 and into the first Fabry-Perot etalon FP_1. Once light entered the first Fabry-

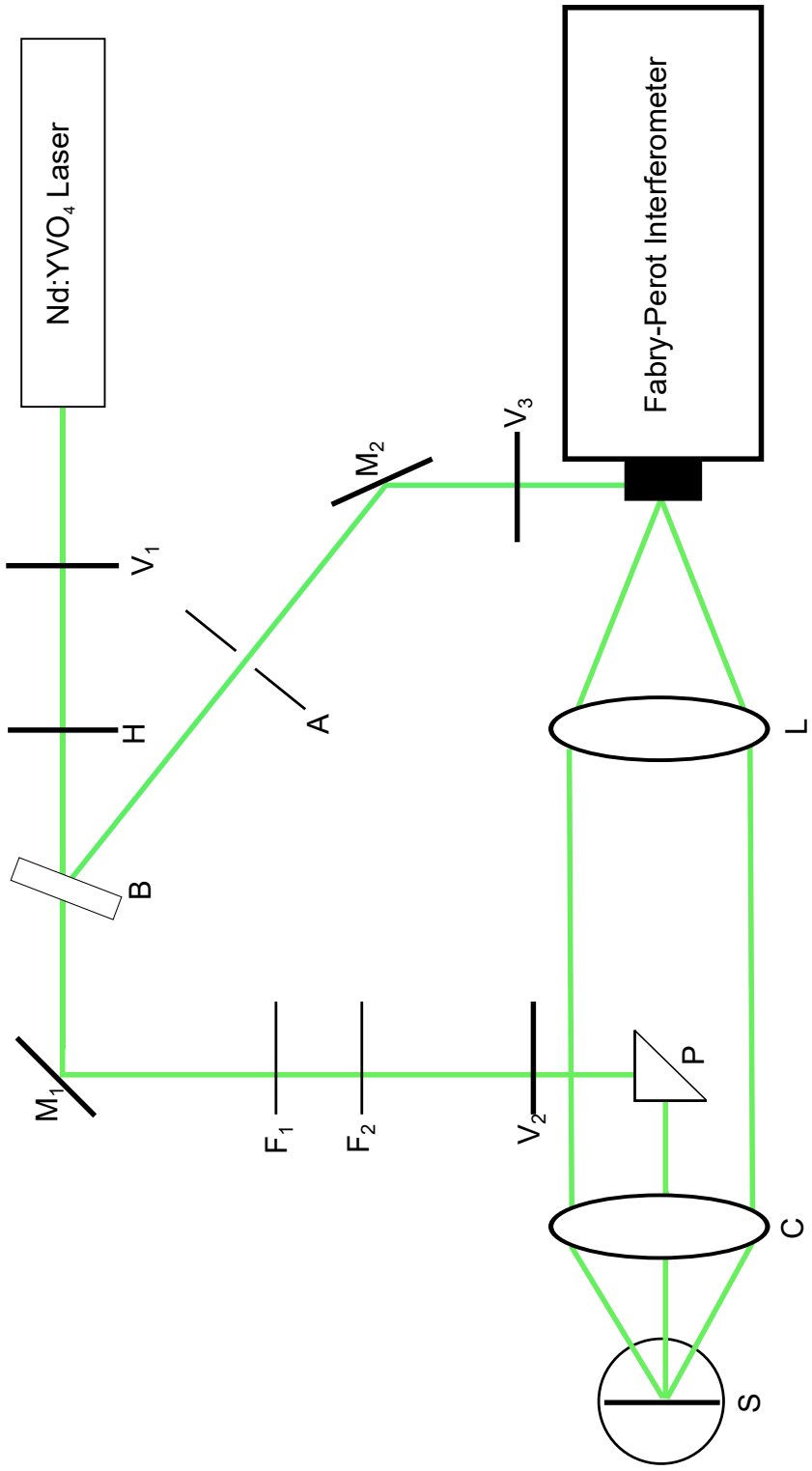

Figure 3.2: Room temperature Brillouin spectroscopy setup. V - variable neutral density filter, H - half wave plate, B - beam splitter, M - mirror, A - aperture, F - filter, P - prism, C - camera lens, S - sample, L - lens.

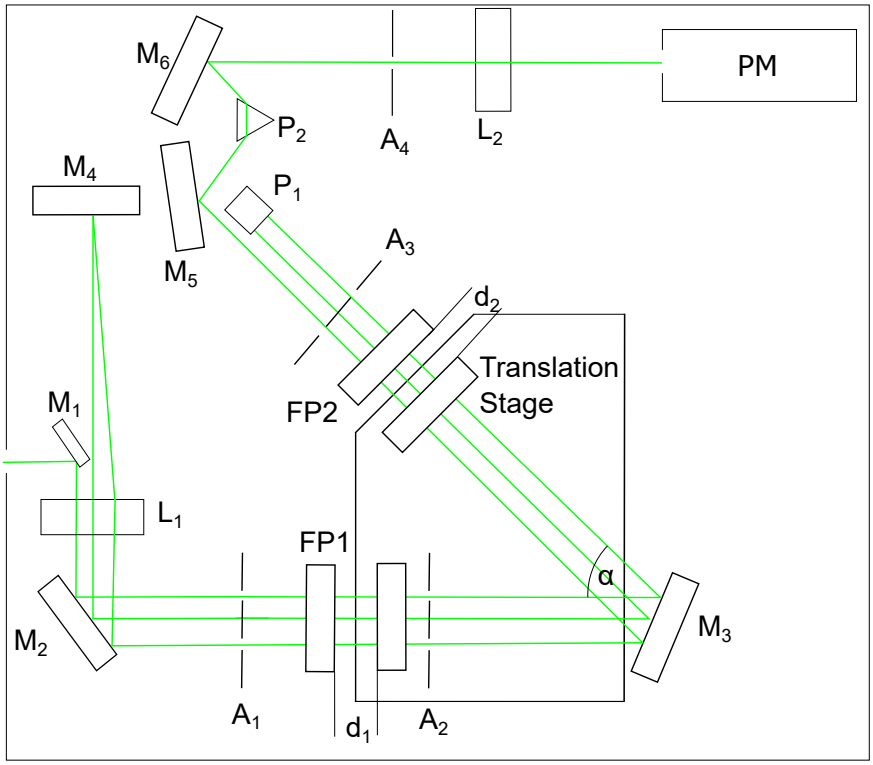

Figure 3.3: Optics of six pass tandem Fabry-Perot interferometer. M_i - mirror, L_i - lens, A_i - aperture, FP_i - Fabry-Perot interferometer, d_i - spacing of interferometer i, α - angle between FP_1 and FP_2, P - prism, PM - photomultiplier tube.

Perot etalon, only frequencies which satisfied Equation (2.42) were transmitted, which passed through the corresponding hole of aperture A_2. It is important to note that apertures A_1, A_2, and A_3 each had three holes, allowing for three passes through each of the Fabry-Perot etalons. Transmitted light was reflected by mirror M_3, redirecting the transmitted beam to Fabry-Perot etalon FP_2. As in FP1, only frequencies satisfying Equation (2.42) were transmitted and passed through the first hole of aperture A_3. The beam was then incident on prism P_1, which redirected the beam back through the second hole of aperture A_3, such that it was anti-parallel to the beam transmitted from FP_2.

The beam that was redirected by prism P_1 passed through the Fabry-Perot etalons, and corresponding holes in apertures A_2 and A_1. The beam transmitted back through FP_1 was reflected by M_2, where it was focused by lens L_1 onto mirror M_4. M_4 reflected the beam back through L_1, where the beam went through a final pass through the Fabry-Perot mirror chambers.

After passing through the final hole of A_3, the beam was incident on mirror M_5, and was then directed through aperture A_4 and onto lens L_2. L_2 focused the beam onto the Fabry-Perot interferometer output pinhole of the photomultiplier PM, which sends information through the electronics, generating a spectrum.

The benefit to using a tandem Fabry-Perot interferometer is that the addition of additional passes through the etalons drastically increases the finesse of a spectrum, yielding much stronger peak intensity in the spectrum corresponding to inelastic scattering events.

3.2.2 Alignment of Fabry-Perot Interferometer

With the photomultiplier tube turned off, the optics inside the tandem Fabry-Perot interferometer were re-aligned before proceeding with experiments. With a reflective surface in the sample holder, the scattered light beam was focused on the entrance pinhole of the interferometer, with a diameter of 1000 μm, such that the aperture was fully illuminated.

By placing a card behind A_1, we were able to check the focusing of the scattered beam. The external optics were focused until the shadow of the prism, from Figure 3.2, was visible on the card. The card was placed in front of M_3. With the electronics in tandem mode, the Z parameter, corresponding to the mirror spacing of the first Fabry-Perot etalon, was adjusted until a fringe pattern was visible on the card. The parameter Y1, the vertical tilt of the mirror in FP_1 was adjusted until the fringe pattern was completely vertical, and X1, the horizontal tilt, was adjusted until the fringe filled the field of view. The card was moved behind the first hole of A_3. δ Z was adjusted until the fringe pattern was visible on the card. As with Y1 and X1, Y2 and X2 were adjusted such that the fringe was vertical and filled the field of view.

The card was then placed behind the third hole of A_3 to ensure that the scattered light had undergone all six passes through the interferometer. At this point, parameters X1, Y1, X2, and Y2 were tweaked to produce maximum transmission. Finally the card was used to ensure the beam passes through A_4 and L_2, and into the pinhole of the photomultiplier. Once alignment of the internal optics was complete, the interferometer was ready to undergo routine alignment for an experiment.

3.3 Raman Scattering

3.3.1 Optical System

For both room temperature and high temperature Raman scattering, PST samples were placed in a high temperature cell (see Section 3.4) within the Raman scattering apparatus, as shown in Figure 3.4. In these experiments, the light source used was a 514.5 nm Ar^+ laser. The beam first passed through a variable neutral density filter, reducing the power of the laser beam to 20 mW. The next piece of the apparatus is the parabolic mirror M_P. This mirror has a 3 mm coaxial pinhole located at its center, allowing the incident beam to pass through it. Once the beam passed through the pinhole of the parabolic mirror, it was incident on aperture A, then entered the high temperature cell. Inside the high temperature cell, there was a lens which focuses the incident beam onto the sample. This will be discussed in further detail in Section 3.4.

A 180° backscattering geometry was used, thus scattered light was collected by the internal lens of the high temperature cell, and sent back through the entrance of the cell. The scattered beam passed through the same aperture A, which directs the scattered beam onto the parabolic mirror. The mirror reflected the scattered beam onto lens L_1, which collimated the beam. The collimated beam then passed through another aperture, before being focused onto the pinhole of the double grating interferometer by a second lens L_2, with a focal length of 10 cm.

A schematic of the spectrometer is shown in Figure 3.5. The double grating spectrometer used in Raman experiments, manufactured by Spex Industries, consisted of two holographic gratings with 1800 grooves/mm and dimensions of 102 mm × 102 mm, and has a focal length of 0.85 m and aperture of $f/7.8$.

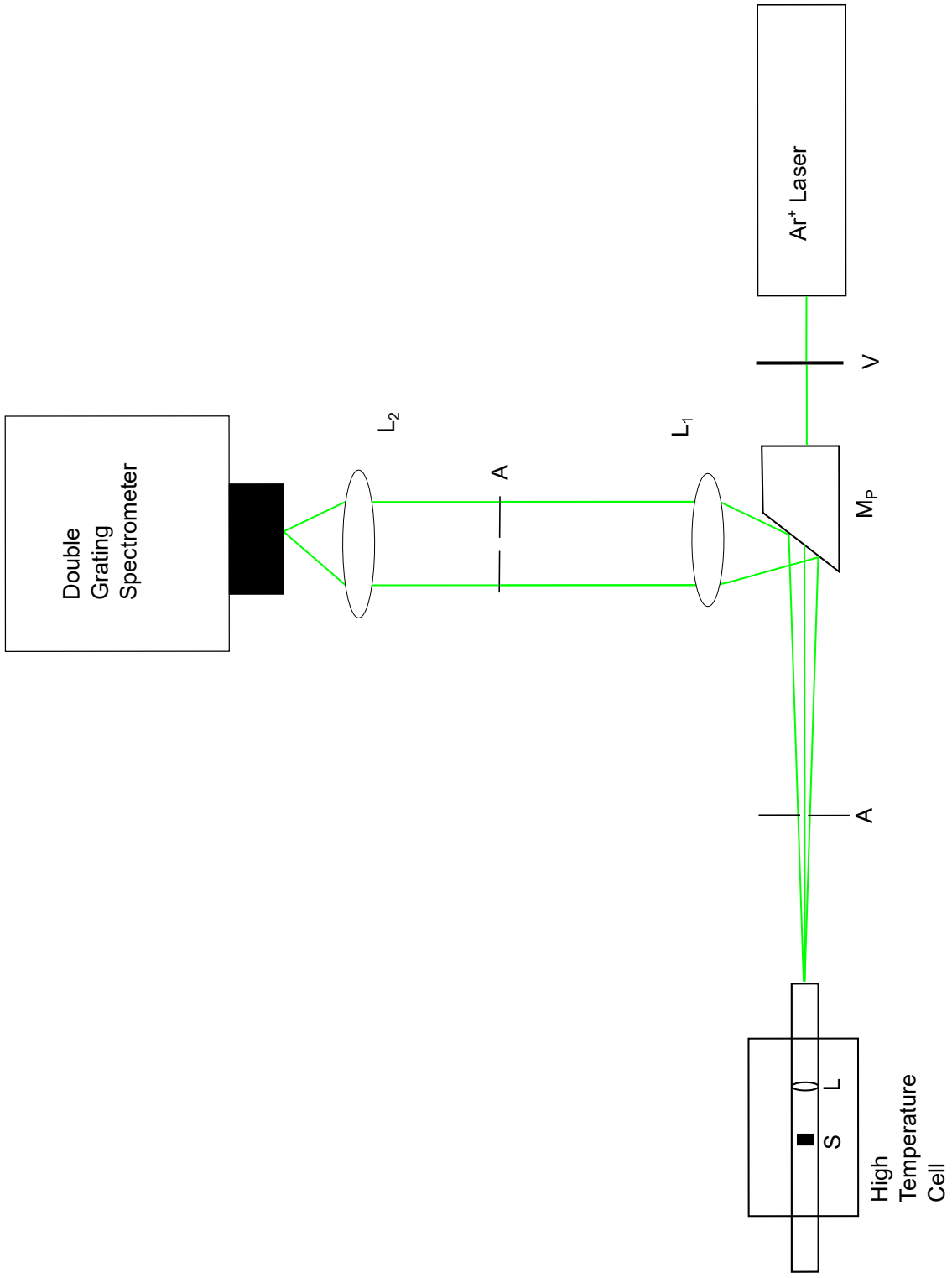

Figure 3.4: Raman spectroscopy setup. V - variable neutral density filter, M_P - parabolic mirror, A - aperture, L - lens.

The scattered light beam entered the spectrometer through the entrance slit of width 300 μm and completely filled the first collimating mirror M_1. M_1 reflected the light beam onto the first grating G_1, which dispersed the light. This dispersed light was focused by the second collimating mirror M_2 onto a plane mirror which reflected the dispersed beam through a slit and into the second grating chamber. In this chamber, a plane mirror reflected the dispersed beam onto collimating mirror M_3 such that it was completely filled. This mirror directs the beam onto the second grating G_2 which further dispersed the beam. Finally, the dispersed light was focused by the last collimating mirror M_4 onto the output pinhole, which was then collected by the photomultiplier tube. The information recorded by the photomultiplier tube was then sent to the computer, with interfaced electronics and software, to create a digital spectrum.

3.4 High Temperature Cell

The high temperature cell used in these experiments, shown in Figure 3.6, was built by Dr. Maynard Clouter. The PST sample was placed on the holder in a quartz tube, as shown in Figure 3.6(d), and was positioned using the positioning dial D. The quartz tube was flooded with inert He gas, which was used to transfer heat from the surface of the tube to the sample. The cell was heated through the use of coiled wires surrounding the quartz tube C, as shown in Figure 3.6(c) and was heavily insulated, shown by I. The temperature control knob located on the bottom of the cell was used to adjust temperature, with a range of 273 K - 1673 K. Outside the cell, the exterior of the tube was cooled with the use of a refrigerated circulating bath, which generated

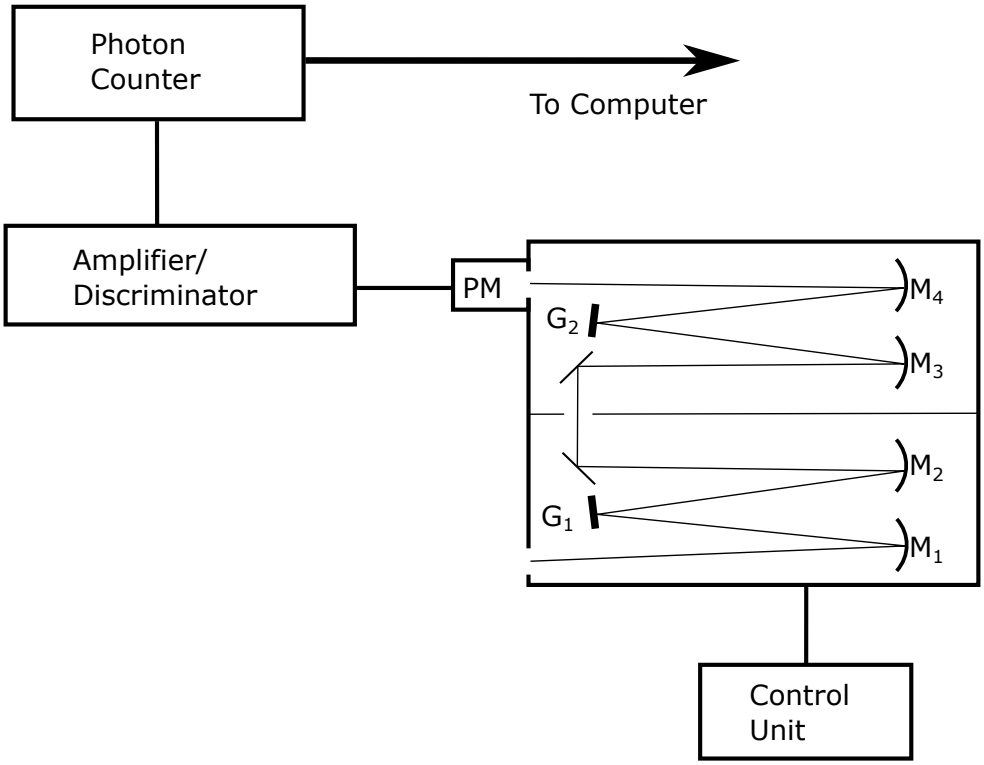

Figure 3.5: Schematic of double grating interferometer used in Raman scattering experiments. M_i - collimating mirror, G_i - holographic grating, PM - photomultiplier tube.

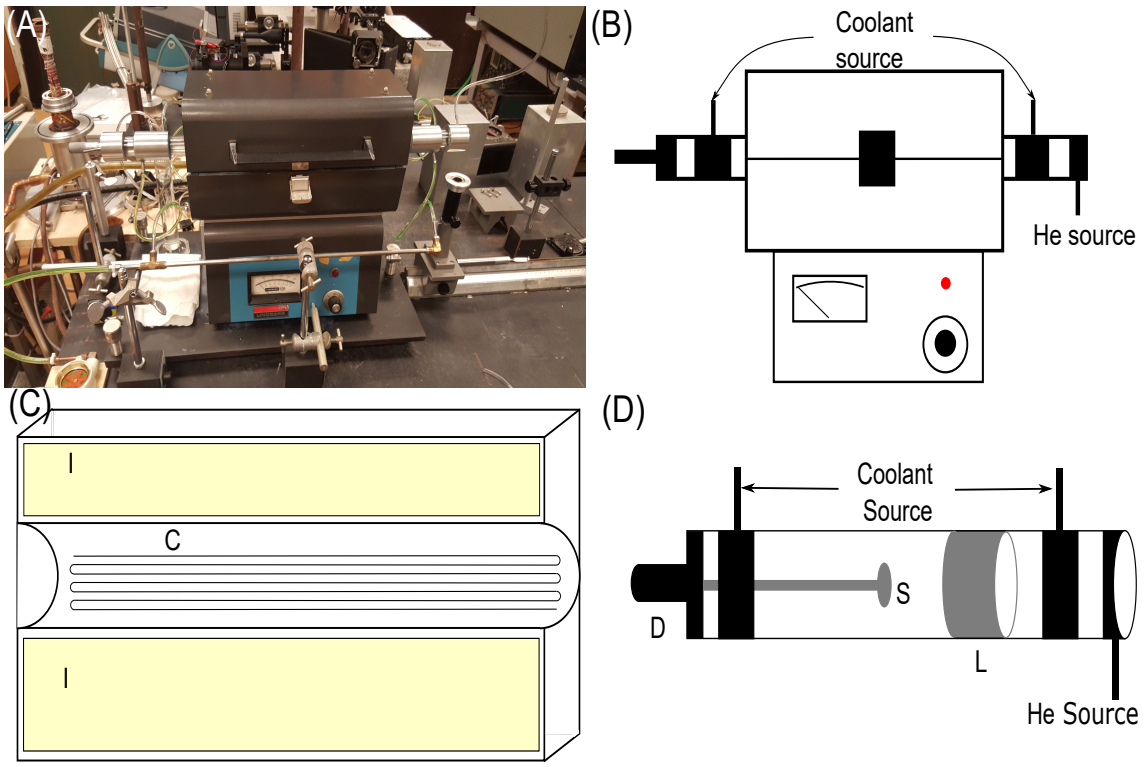

Figure 3.6: (a) Photograph of high temperature cell. (b) Schematic view of high temperature cell. (c) Schematic of the inside of the high temperature cell. I - insulation, C - wire coils. (d) Schematic of quartz tube in high temperature cell. D - positioning dial, S - sample, L - lens.

a flow of cooled water around both sides of the quartz tube.

Chapter 4

Results and Discussion

4.1 Room Temperature Brillouin Scattering

Brillouin light scattering experiments were performed on two PST ceramic samples with equal disorder at room temperature, with angles of incidence ranging from 20° to 70°, which corresponds to a range of internal angles of 8° to 22° with respect to the normal to the sample surface, using a 180° backscattering geometry. In each spectrum, two sets of Brillouin peaks were observed, which were labeled T and L.

Table 4.1: Frequencies of Stokes and Anti-Stokes peaks for transverse and longitudinal bulk modes for PST ceramic #1 collected at room temperature.

θ_i ($\pm 1°$)	f_T^S ($\pm$ 1 GHz)	f_T^A ($\pm$ 1 GHz)	f_L^S ($\pm$ 0.1 GHz)	f_L^A ($\pm$ 0.1 GHz)
20	25	24	43.6	43.3
30	25	25	43.3	43.3
40	24	25	43.1	42.7
50	24	25	43.4	43.3
60	24	25	43.7	43.0
70	24	25	43.4	42.8

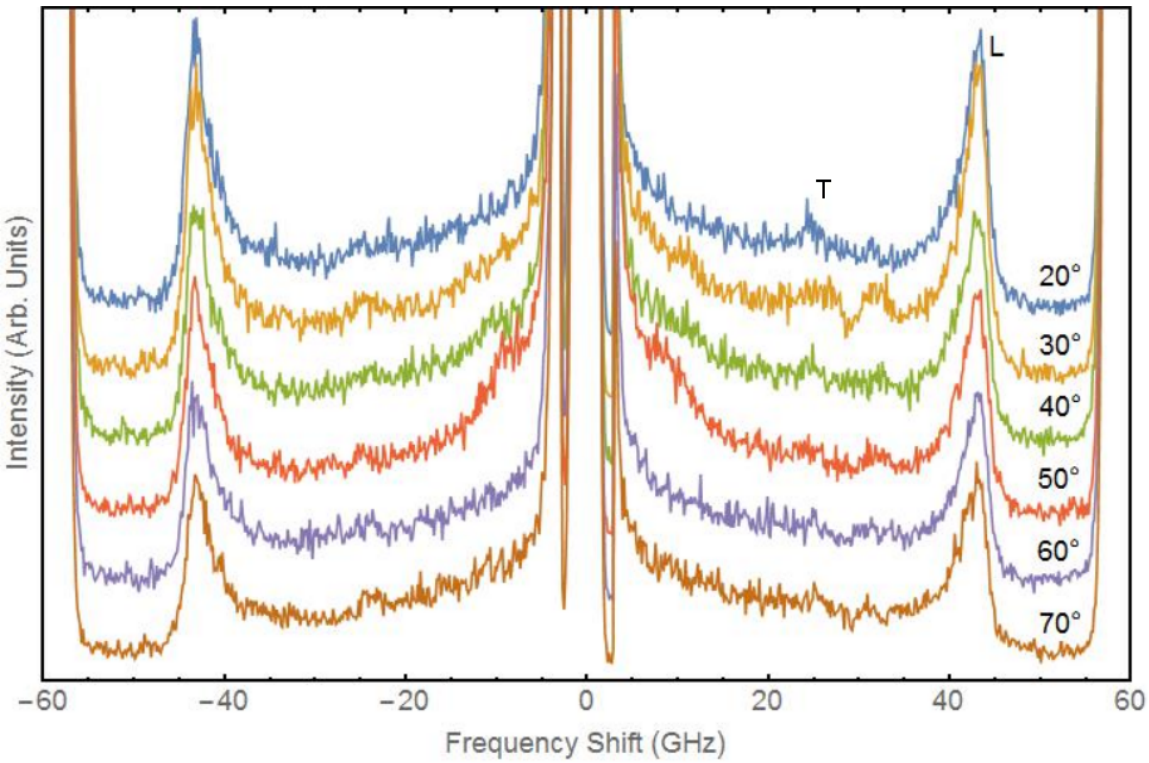

Figure 4.1: Spectra collected from PST ceramic #1 at room temperature. T corresponds to the transverse bulk mode, L corresponds to the longitudinal bulk mode.

Spectra collected from PST ceramic #1 are shown in Figure 4.1. Table 4.1 presents the frequency shifts of the Stokes and anti-Stokes peaks located in these Brillouin spectra. Using the average frequency shifts of Table 4.1, bulk mode frequency shift was plotted against $\sin\theta_i$, as shown in Figure 4.2. Since there was no change in Brillouin frequency shift with change in angle, by Equation 2.15, these peaks were determined to be due to the transverse and longitudinal bulk modes, respectively. The average values from Table 4.1 were used to calculate phonon velocities, by applying Equation (2.16). These velocities were used in the relationship given by Equations (2.30 - 2.32) to calculate elastic constants c_{11}, c_{44}, and c_{12}. These values are shown in Table 4.3. As can be seen, the values for v_L and c_{11} calculated from these results are comparable to those for crystalline PST obtained in previous studies. It should be noted that Jiang *et al.* performed experiments on [001] oriented PST and calculated $c_{33} = \rho v^2$ [16]. They calculated a value of $c_{33} = 173$ GPa, which is very close to the value of c_{11} provided by Fedoseev *et al.* [1]. The values calculated for v_T, c_{44} and c_{12} are similar to the values provided by Fedoseev *et al.* [1] for crystalline PST.

Brillouin light scattering experiments were performed on PST ceramic #2 under identical conditions. Spectra collected with angles of incidence ranging from 20° - 70° are shown in Figure 4.3. As with PST ceramic #1, two peaks were found in these spectra. These peaks were found to be independent of angle of incidence, as shown in Figure 4.4, therefore these peaks were determined to be due to the transverse and longitudinal bulk modes. Frequencies of the bulk mode peaks in these spectra are shown in Table 4.2. The difference in spectra quality was caused by a replacement of the photomultiplier tube in the tandem Fabry-Perot interferometer. The new photomultiplier tube allowed spectra with less noise to be collected with shorter

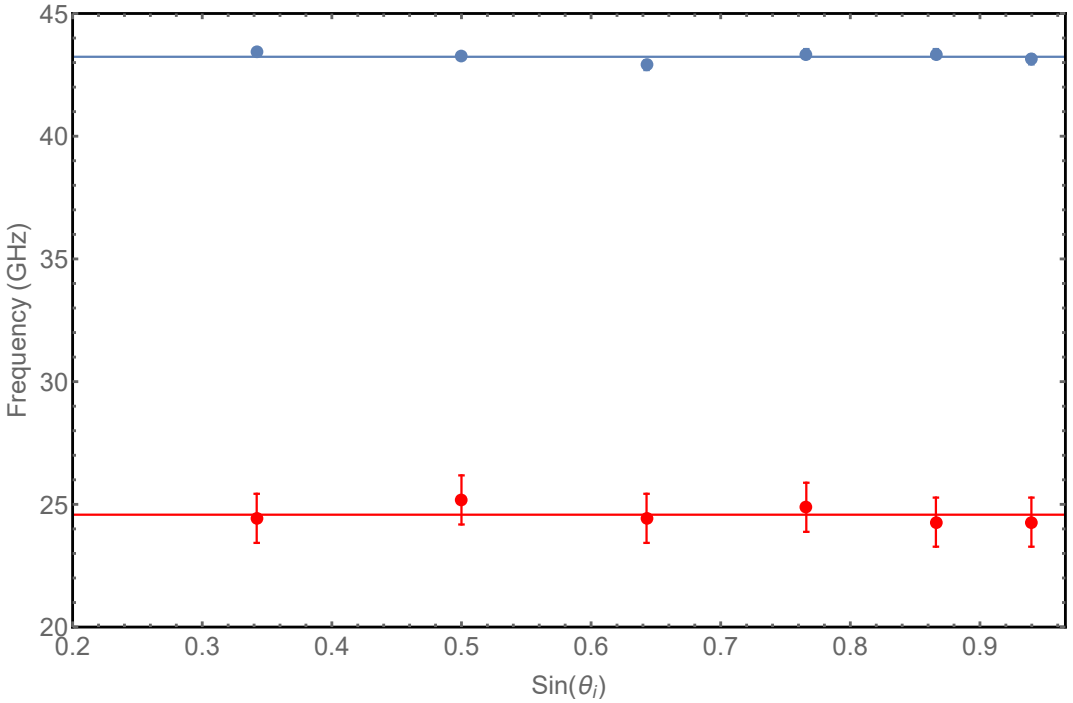

Figure 4.2: Longitudinal (blue) and transverse (red) bulk mode frequencies at angles of incidence ranging from 20° - 70° for PST ceramic #1. Horizontal line corresponds to the average bulk mode frequencies.

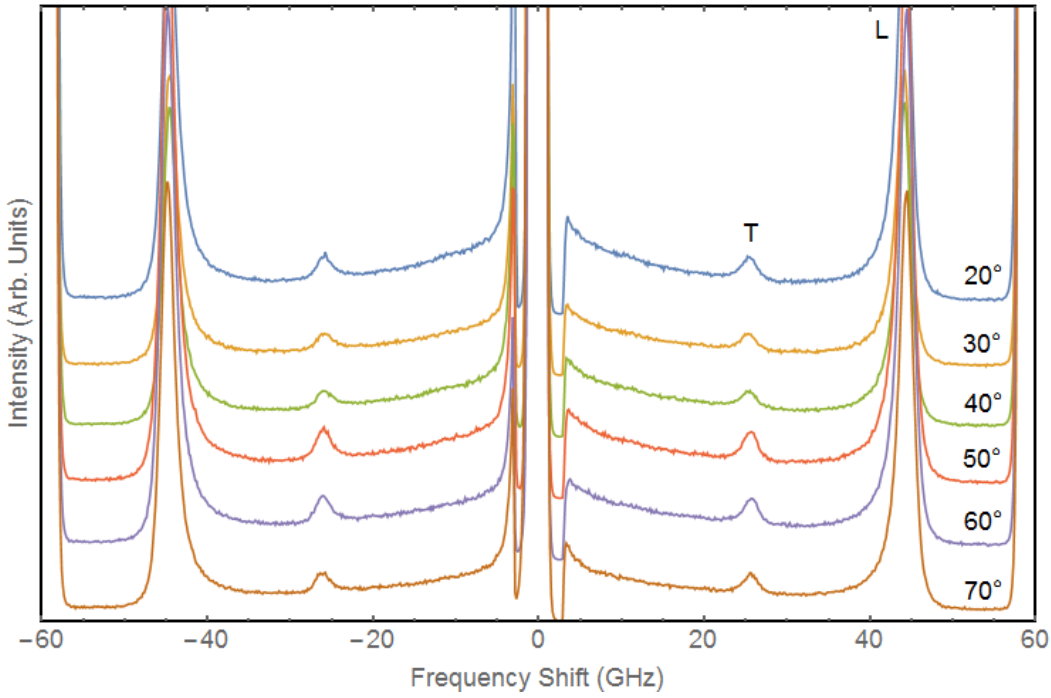

Figure 4.3: Spectra collected on PST ceramic #2 at room temperature. T corresponds to the transverse bulk mode, L corresponds to the longitudinal bulk mode.

collection times.

Using the average frequency shift of peaks from Table 4.2, the velocities of the transverse and longitudinal bulk modes were calculated using Equation (2.16), and are listed in Table 4.3. The value for v_L for this sample is similar to the values provided by literature for crystalline PST, and is within uncertainty of the value calculated for PST ceramic #1. The value for v_T for PST ceramic #2 is larger than the value provided by Fedoseev *et al.* on crystalline PST, however it is within 6% of the value calculated for PST ceramic #1.

As with PST ceramic #1, elastic constants c_{11}, c_{44}, and c_{12} were determined using

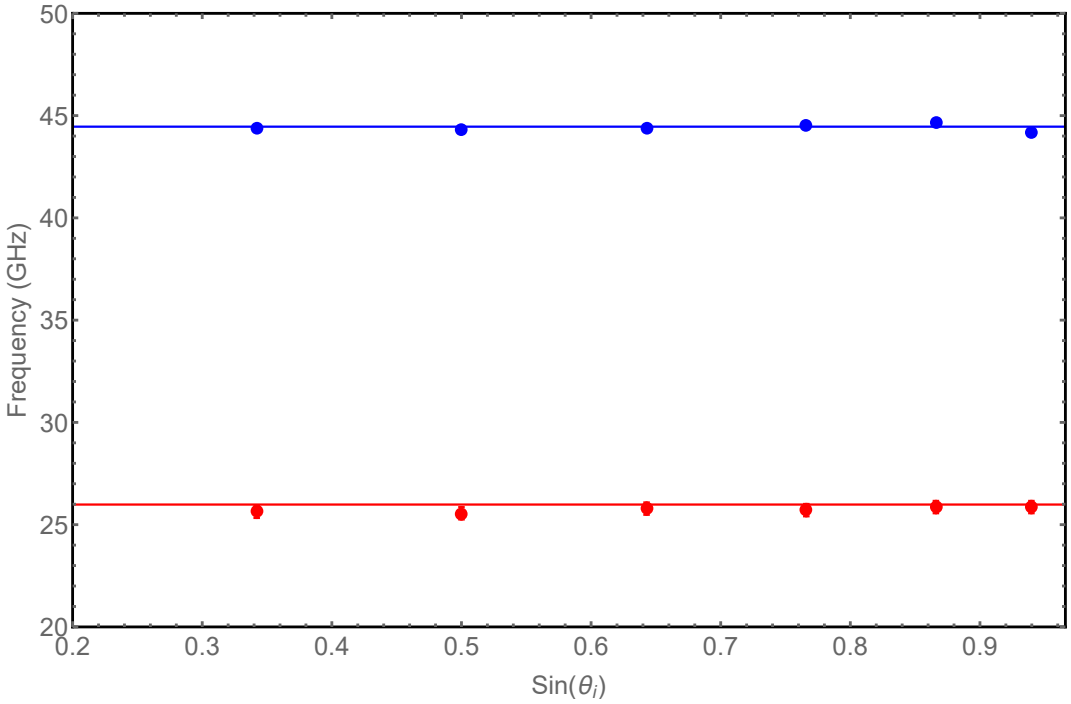

Figure 4.4: Longitudinal (blue) and transverse (red) bulk mode frequencies at angles of incidence ranging from 20° - 70° For PST ceramic #2. Horizontal line corresponds to the average bulk mode frequencies.

Table 4.2: Frequencies of Stokes and Anti-Stokes peaks for transverse and longitudinal bulk modes for PST ceramic #2 collected at room temperature.

θ_i ($\pm 1°$)	f_T^S ($\pm$ 0.3 GHz)	f_T^A ($\pm$ 0.3 GHz)	f_L^S ($\pm$ 0.1 GHz)	f_L^A ($\pm$ 0.1 GHz)
20	25.8	25.5	44.2	44.6
30	25.2	26.0	44.0	44.6
40	25.3	26.2	44.0	44.8
50	26.1	25.3	44.9	44.2
60	26.5	25.5	44.9	44.3
70	26.4	25.3	44.1	44.3

Table 4.3: Bulk mode velocities and corresponding elastic constants from current work and previous studies.

	v_L (m/s)	c_{11} (GPa)	v_T (m/s)	c_{44} (GPa)	c_{12} (GPa)
Present Work	4600 ± 100	189 ± 8	2600 ± 100	61 ± 5	70 ± 20
(ceramic)	4700 ± 100	200 ± 9	2750 ± 90	68 ± 4	60 ± 20
Jiang *et al.*[16] (crystal)	4330	-	-	-	-
Fedoseev *et al.*[1] (crystal)	∼4370	∼ 176	∼2510	∼57	∼59
Pietraszko *et al.*[10]) (crystal)	4742	203	-	-	-
Zinenko *et al.* [33] (crystal)	-	209	-	74	75

the relations given in Equations (2.30 - 2.32). The value for c_{11} is similar to the values provided by literature for crystalline PST, and is within 6% of the value calculated for the PST ceramic #1. The value of c_{44} is larger than the crystalline value provided by Fedoseev *et al.* [1], however it overlaps with the value calculated for the first PST ceramic in this work, within uncertainty. The range of elastic constant c_{12} overlaps with the value for crystalline PST from Fedoseev *et al.* [1].

The similarity between the elastic constants calculated for the ceramics used in this work and those found for crystalline PST in previous studies [1, 10, 16] is due to the polycrystalline nature of the ceramics used. As discussed earlier, these ceramics were fabricated through the use of PST powders and thus the ceramics are comprised of crystalline grains. By probing acoustic phonons in the ceramic, we thus probe acoustic phonons in these randomly distributed crystalline regions.

In an attempt to observe surface acoustic waves in PST, Brillouin scattering experiments were also performed on PST ceramic with a 40 nm Al coating. This process

was used by Mroz *et al.* to observe surface modes in transparent and semi-transparent media [32]. A spectrum collected at 60° with a free spectral range of 60 GHz is shown in Figure 4.5. This spectrum was collected with higher incident beam power than in previous experiments and, as a result, should be interpreted with caution due to the potential for sample damage due to heating by the laser. An additional peak was observed in this spectrum with a frequency shift of $f_R \simeq 11$ GHz. The peak is significantly wider than typical surface mode peaks. Using Equation (2.20) and the value of the Rayleigh surface mode frequency shift of aluminum from Sandercock *et al.* [34], the frequency shift of the surface mode of aluminum for an angle of incidence of 60° was calculated to be ~ 8.9 GHz, which is much lower than the frequency shift of the peak found in this spectrum. It is therefore unlikely that this peak is due to the aluminum film and may in fact be due to the Rayleigh surface mode of PST.

Unfortunately, the Al coating on the sample degraded with time. This degradation is likely due to long exposure to the high power laser beam. Subsequent spectra show signs of this damage, as shown in Figure 4.6, and thus this sample could not be used to further explore the potential Rayleigh surface mode in Figure 4.5.

4.2 Raman Light Scattering

4.2.1 PST Ceramic #1

Room Temperature Raman Scattering

Raman light scattering experiments were performed on PST ceramic at room temperature. Experiments were performed over a range of 1000 cm^{-1}, starting at the

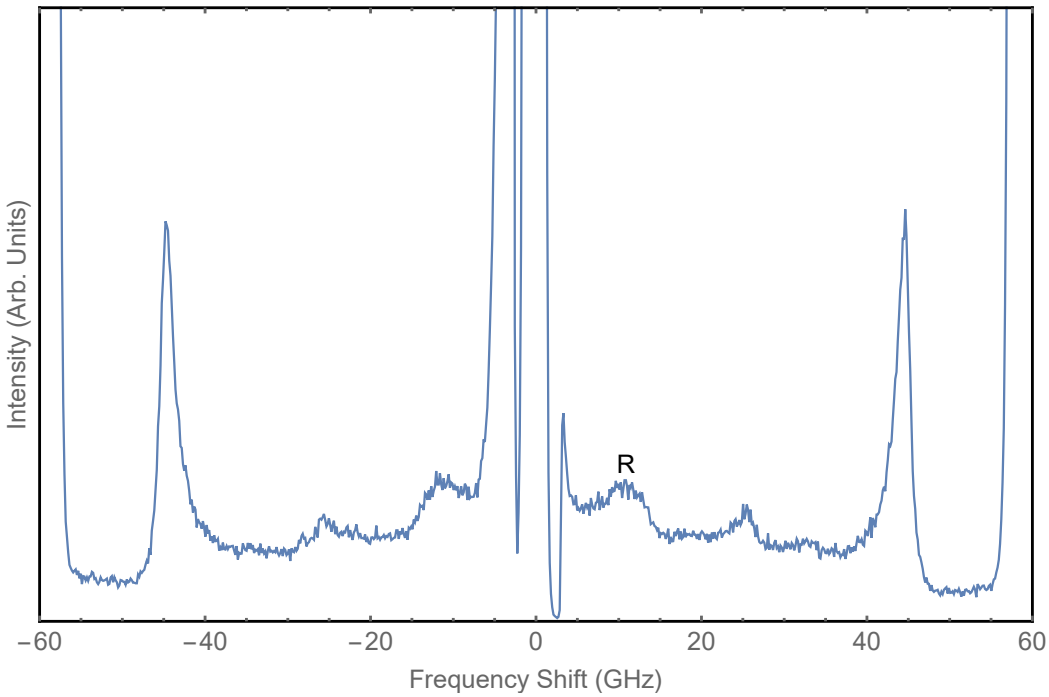

Figure 4.5: Brillouin spectra collected on PST ceramic with Al coating at room temperature with an angle of incidence of 60° and free spectral range of 60 GHz.

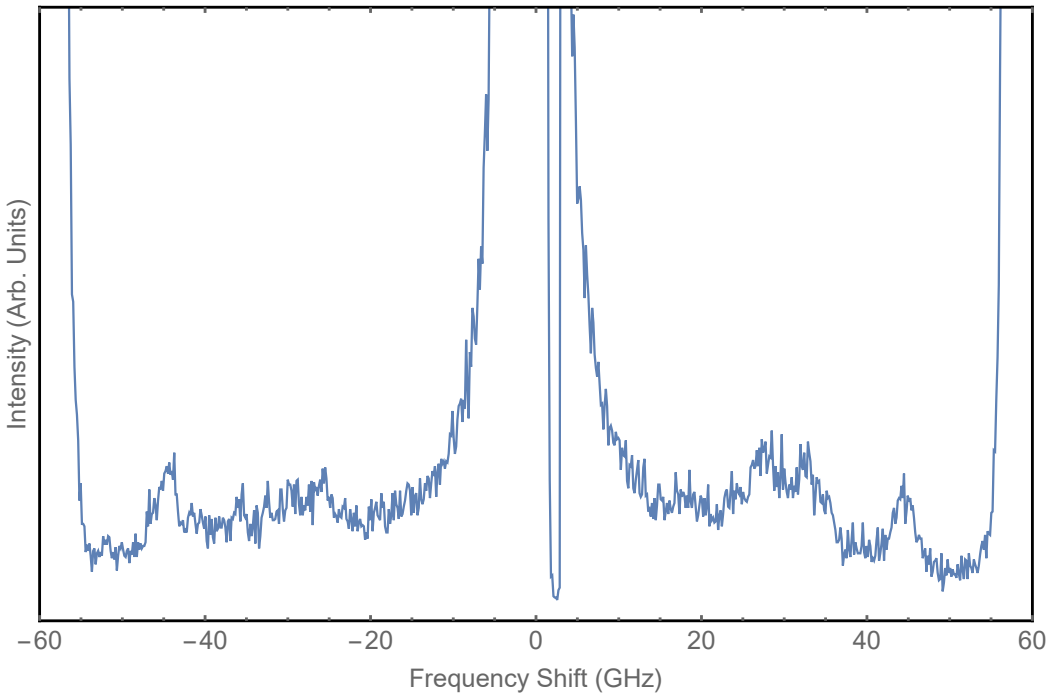

Figure 4.6: Brillouin spectra collected on PST ceramic with Al coating at room temperature with an angle of incidence of 60° and free spectral range of 60 GHz. This spectrum does not share features with the spectrum in Figure 4.5. Upon closer inspection, the damage to the sample was revealed.

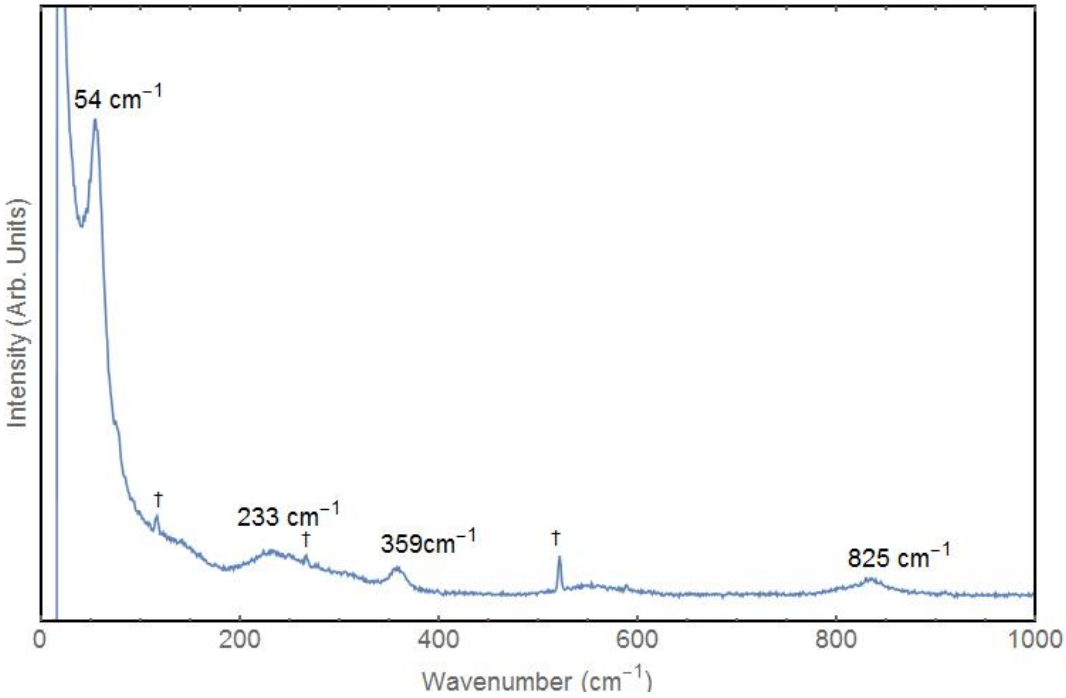

Figure 4.7: Raman spectra collected from PST ceramic #1 at room temperature. Raman peaks are labeled with shift values. Peaks labeled with † are laser plasma lines.

wavenumber of the laser, 19430 cm^{-1}. The room temperature spectrum for PST ceramic #1 is shown in Figure 4.7. There were four major peaks observed in this spectrum. As is shown in Table 4.4, the Raman shifts for three of these peaks were consistently lower than the values provided by Bismayer [14] and Setter [19], but within range of the values provided by Mihailova [18, 20], for crystalline PST. The peak at 835 cm^{-1} has a comparable shift to the values obtained for crystalline PST.

The strongest peak, occurring at 54 cm^{-1}, is the F_{2g} mode [35, 36], corresponding to vibrations of the octahedron formed by oxygen atoms within the PST unit cell [17]. The F_{2g} mode is threefold degenerate, symmetric with respect to a fourfold rotation,

Table 4.4: Raman shift of peaks observed in room temperature Raman experiments of PST ceramic compared to values provided by literature for PST crystals

	F_{2g} (cm^{-1})	F_{1g} (cm^{-1})	F_{2u} (cm^{-1})	A_{1g} (cm^{-1})
Present Work	54 ± 2	230 ± 10	359 ± 5	835 ± 5
	55 ± 2	232 ± 10	358 ± 5	837 ± 10
Bismayer *et al.* [14]	61	240	370	830
Mihailova *et al.*[18]	54	230	350	823
Mihailova *et al.* [20]	53	240	350	830
Setter *et al.* [19]	60	238	365	835

and has an inversion center which is kept throughout the vibration. This is the peak that was primarily observed in high temperature experiments.

The peak at 230 cm^{-1} is due to the F_{1g} mode. This mode corresponds to rotation of BO_3 bonds in the material, where B is either Sc or Ta [18]. The peak located at 359 cm^{-1} corresponds to an F_{2u} mode [18]. This mode is caused by vibrations along the PbO bonds in the material, and can be used to observe a change in the order of B-site cations in PST [19]. The final peak, located at 835 cm^{-1}, is caused by symmetric B-O stretching in the BO_6 octahedra, and is the A_{1g} mode [18].

There are three other peaks observed in the room temperature Raman spectrum of PST ceramic #1, occurring at 116 cm^{-1}, 266 cm^{-1}, and 521 cm^{-1}. These peaks, labeled as † in Figure 4.7, are plasma lines, which are an artefact of the incident laser. These peaks occur at the same positions in all spectra, and as such, these peaks were used as calibration lines in high temperature Raman scattering experiments. It is important to note that subsequent high temperature spectra were calibrated to two plasma lines, located at 77 cm^{-1} and 521 cm^{-1}

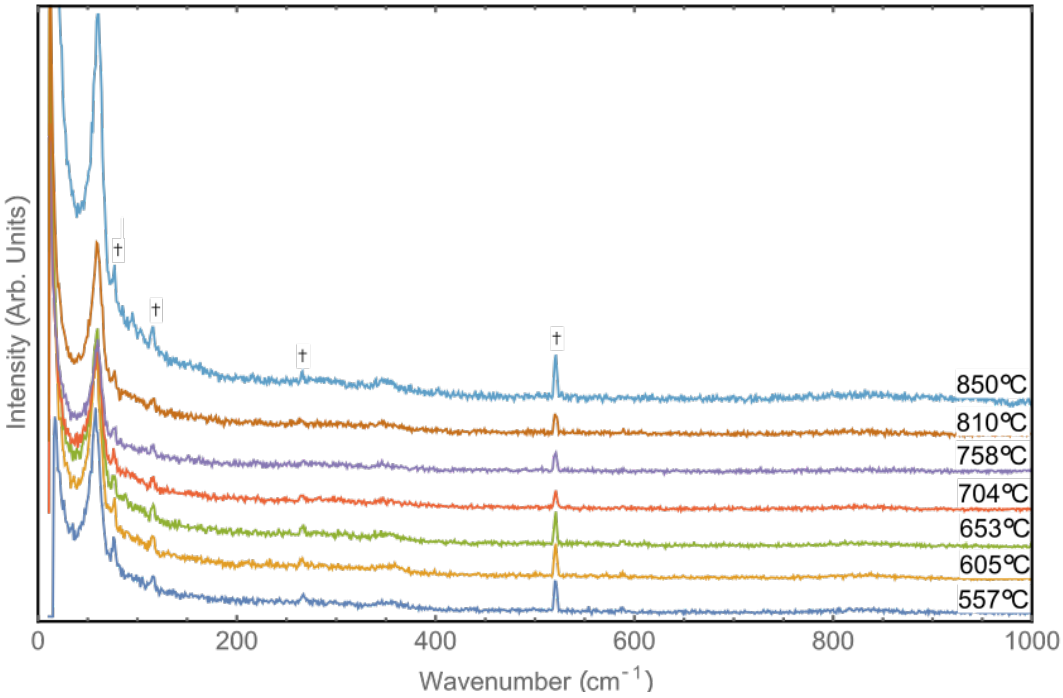

Figure 4.8: Raman spectra collected on PST ceramic at temperatures ranging from 557 °C to 850°C, over a range of 990 cm^{-1}. Peaks labeled with † are laser plasma lines.

High Temperature Raman Scattering

Raman light scattering experiments were also performed on PST ceramic #1 at temperatures ranging from 557 °C to 1200 °C. As with room temperature experiments, high temperature experiments were performed over a range 1000 cm^{-1}, starting from 19430 cm^{-1}. All spectra were collected under identical conditions. It is important to note that at temperatures greater than ∼800 °C, the W(5%Re) - W(26%Re) thermocouple used for temperature measurements became brittle, requiring that the analog scale on the high temperature unit be used to determine temperature for T > 800°C.

Spectra collected at temperatures between 557 °C and 850 °C are shown in Figure 4.8. In this temperature range, the F_{1g} peak, observed at 230 cm^{-1} at room temperature, was not present. This was not a surprising result, as the intensity of the F_{1g} mode decreases rapidly with temperature for crystalline PST for temperatures greater than 177°C [20]. This decrease in peak intensity in crystalline PST, and likely therefore polycrystalline ceramic PST, is caused by the formation of regions comprising off-centered BO_6 octahedra [20]. The F_{2u} peak was present in all of the spectra shown in Figure 4.8, however it was significantly weaker than in the room temperature spectrum. The A_{1g} peak was extremely weak, and was only observable in the spectra collected at 557 °C, 605 °C, and 704 °C. These peaks were much weaker than those found in the room temperature spectrum, and thus have a much larger associated uncertainty. Raman shifts for these peaks are provided in Table 4.5.

In the spectra shown in Figure 4.8, the F_{2g} mode shifted by $\sim 10\%$ when compared to the room temperature spectrum shown in Figure 4.7. The peaks corresponding to the F_{2g} mode in the high temperature spectra are also weaker than the F_{2g} peak in the room temperature spectrum. This behaviour is consistent with that of the same mode in crystalline PST [20]. Between 557 °C and 800 °C, there was an increase in shift of the F_{2g} peak with increasing temperature, however there was negligible change in peak intensity for the F_{2g} mode peak. In the spectrum collected at 850 °C, the peak is more intense than in the lower temperature spectra. This is further illustrated in Figure 4.9 which shows higher resolution spectra collected over a range of 100 cm^{-1} at 10 scans per wavenumber. The width of the F_{2g} mode in high temperature spectra is lower than that of the corresponding peak in the room temperature spectrum. Note that the peak located at 66 cm^{-1} is a laser plasma line.

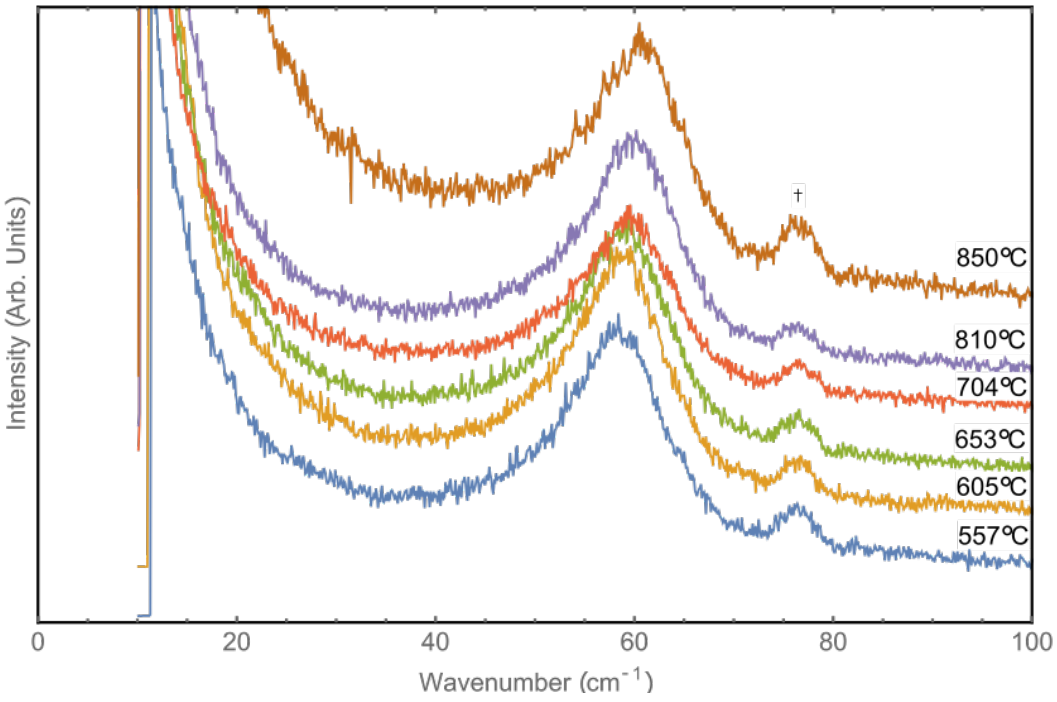

Figure 4.9: Raman spectra collected on PST ceramic at temperatures ranging from 557 °C to 850°C, over a range of 100 cm^{-1}. Peak labeled with † is a laser plasma line.

Table 4.5: Raman peak positions at all temperatures measured for PST ceramic #1.

Temperature (°C)	F_{2g} (cm^{-1})	F_{1g} (cm^{-1})	F_{2u} (cm^{-1})	A_{1g} (cm^{-1})
25	54 ± 2	230 ± 10	359 ± 5	835 ± 5
557	58 ± 1	-	355 ± 10	828 ± 20
609	59 ± 1	-	347 ± 10	836 ± 20
653	59 ± 1	-	345 ± 10	-
704	60 ± 1	-	347 ± 10	821 ± 20
758	60 ± 1	-	346 ± 10	-
810	59 ± 1	-	346 ± 10	-
850	60 ± 1	-	-	-
900	61 ± 1	-	-	-
960	65 ± 3	-	-	-
990	65 ± 3	-	-	-
1050	65 ± 3	-	-	-
1100	65 ± 3	-	-	-

Figure 4.10 shows spectra collected from PST ceramic #1 over temperatures ranging from 900 °C to 1100 °C. In these spectra, the only observable peak is the F_{2g} mode. The F_{2g} mode in this temperature range is significantly weaker than in lower temperature spectra. Furthermore, the intensity of the F_{2g} peak decreases significantly between 900 °C and 960°C. This is shown in greater detail in Figure 4.11. The Raman shifts of these peaks are also shown in Table 4.5. It was noted that the interior of the high temperature cell became coated with a thin grey film at temperatures greater than 990°. In the 1050°C and 1100°C spectra, there is an oscillation in the background signal. This is observable in both Figure 4.10 and Figure 4.11. The source of this signal oscillation is unknown, but may be related to this thin grey film.

In the 1050 °C and 1100°C spectra, there was significant noise at high Raman shifts. At these higher temperatures, the high temperature cell was glowing very brightly. This white glow coming from the cell (see Figure 4.12) was likely the cause

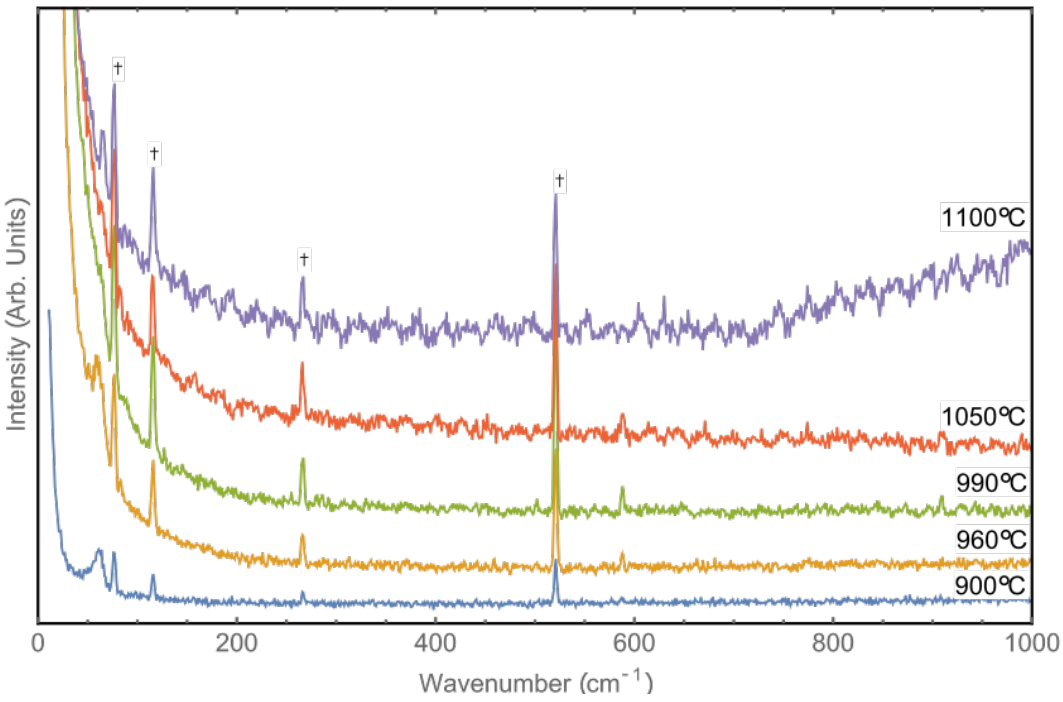

Figure 4.10: Raman spectra collected on PST ceramic at temperatures ranging from 900 °C to 1100°C, over a range of 990 cm^{-1}. Peaks labeled with † are laser plasma lines.

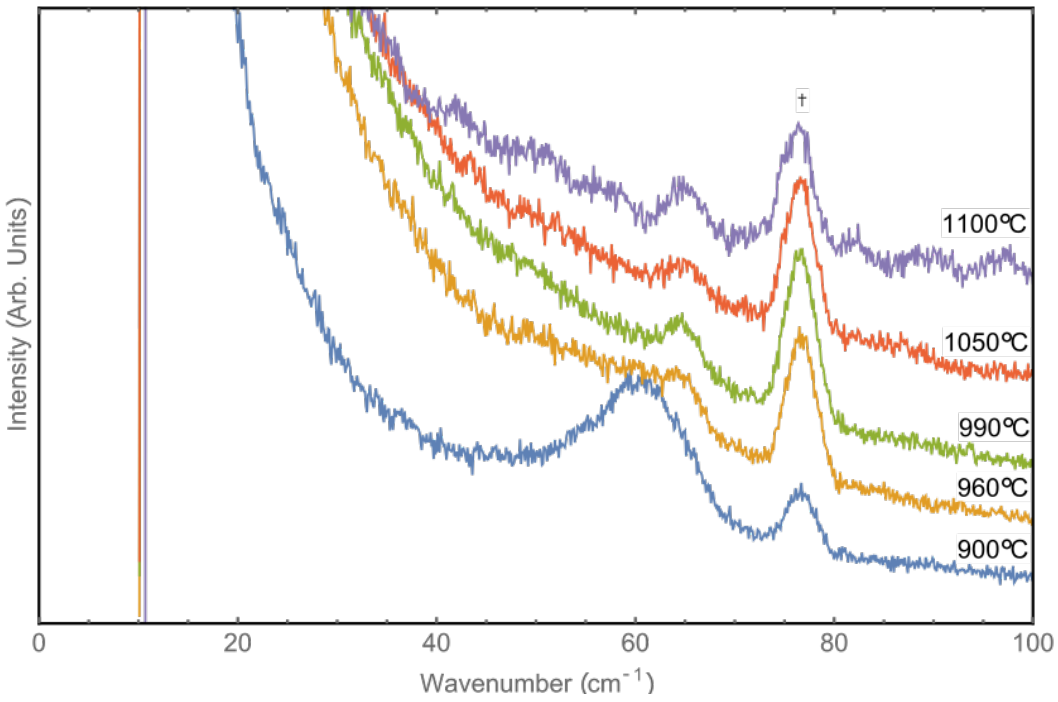

Figure 4.11: Raman spectra collected on PST ceramic at temperatures ranging from 900 °C to 1100°C, over a range of 100 cm^{-1}. Peak labeled with † is a laser plasma line.

of the noise at high shifts. Furthermore, the 1200 °C spectrum, shown in Figure 4.13, showed no Raman peaks for the full range investigated. It was at this temperature that the glow from the high temperature cell was strongest.

When the PST ceramic was removed from the high temperature cell, it was obvious that it had undergone a significant change. The ceramic, originally semi-transparent, was nearly solid white. The change of sample colour is shown in Figure 4.14. The dark colouring on the corner of the sample in the lower picture is an effect of the sample holder. As previously mentioned, when the sample was taken out of the high T cell, there was an unknown thin coating on the lens and the walls of the quartz crystal tube. By comparing our temperature range to the high temperature ordering-disordering properties provided by Setter *et al.* [6, 11], Groves *et al.* [4], and Stenger *et al.* [2, 15], it was determined that this change of colour was due to a loss of PbO from the ceramic in the high temperature region. The loss of Pb and O decreases the content of both in the sample which undoubtedly affects the F_{2g} mode frequency (the loss of PbO in the material disturbs the oxygen octahedron found in the unit cell of PST). This disturbance is likely the cause of the higher frequency shift of the F_{2g} mode in these spectra. The higher reflectivity of the white ceramic is the likely cause of the wide central peak (at 0 cm^{-1}) in the high temperature spectra in Figure 4.10.

Figure 4.15 shows a room temperature Raman spectrum taken on PST ceramic #1 after high temperature experiments. This spectrum was taken with five times the collection time used in the high temperature experiments, and there were no observable Raman peaks in the range investigated, providing further evidence that the sample was transformed in some manner. Three laser plasma lines were observed

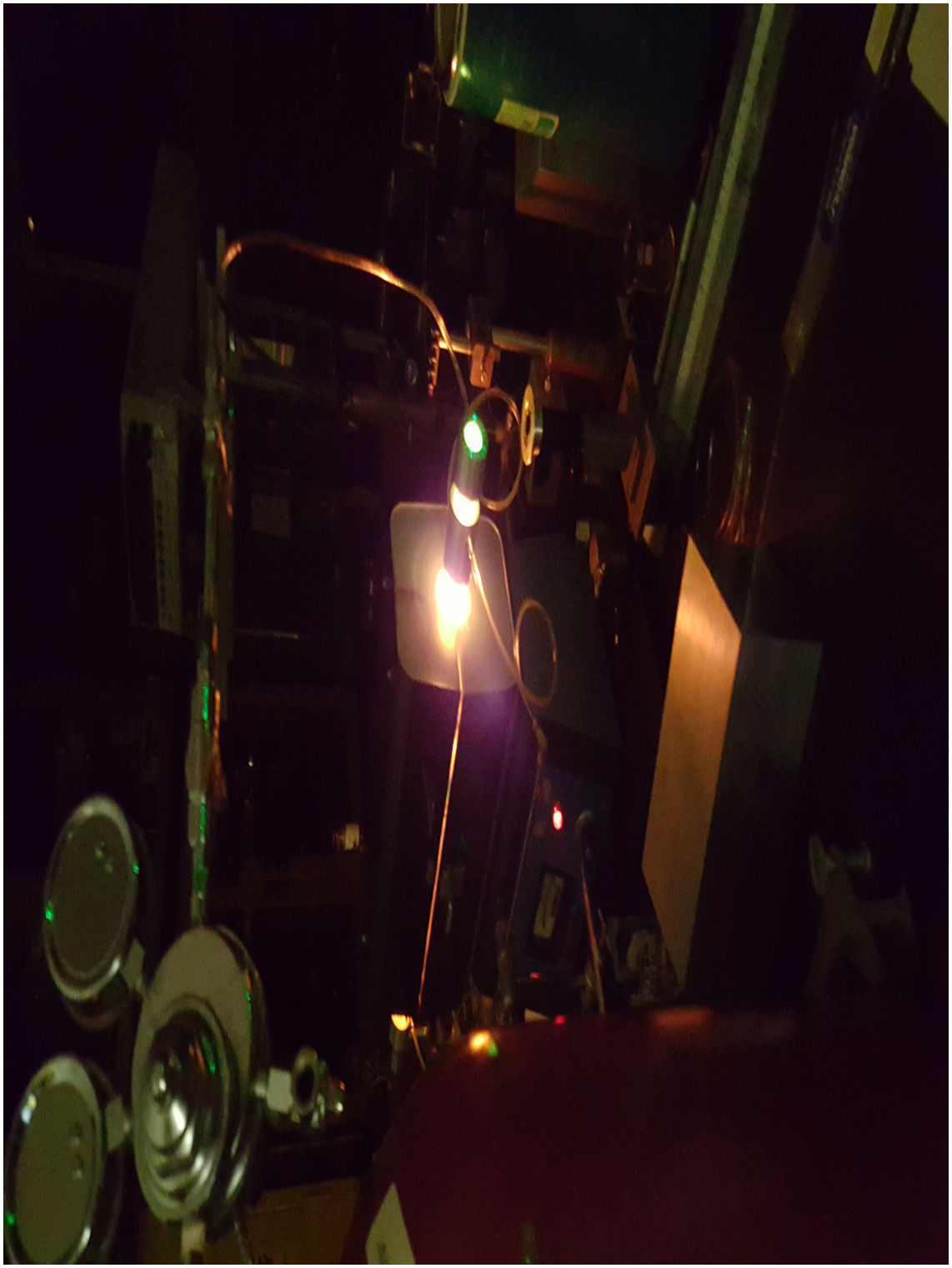

Figure 4.12: High temperature cell at ∼1100°C. Bright white glow is produced by the glowing of the heater coils surrounding the quartz tube.

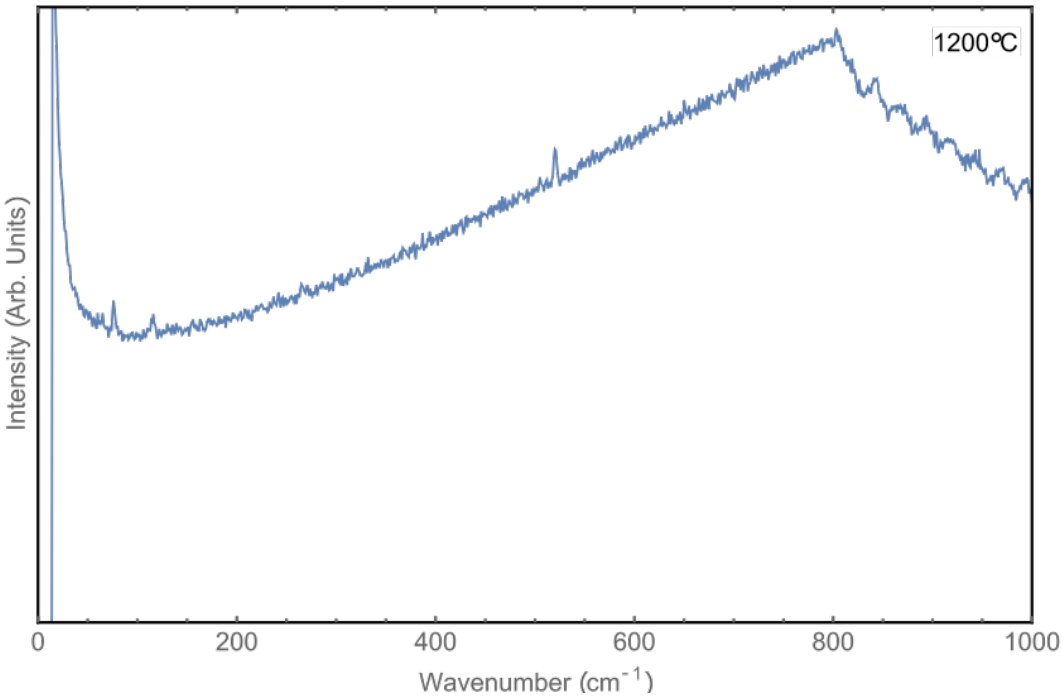

Figure 4.13: Raman spectra collected on PST ceramic at 1200°C, over a range of 990 cm^{-1}. Peaks labeled with † are laser plasma lines.

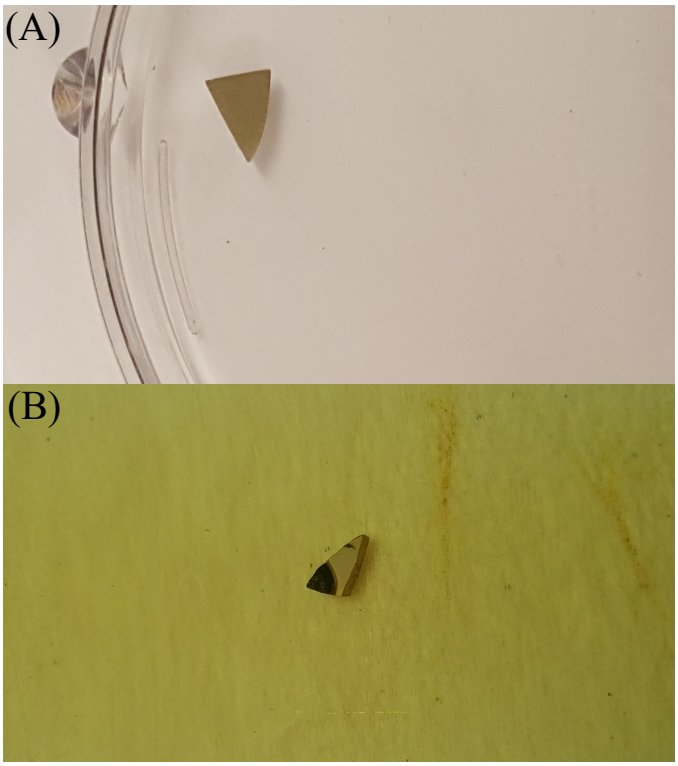

Figure 4.14: PST ceramic before high temperature experiments (A) and after high temperature experiments (B).

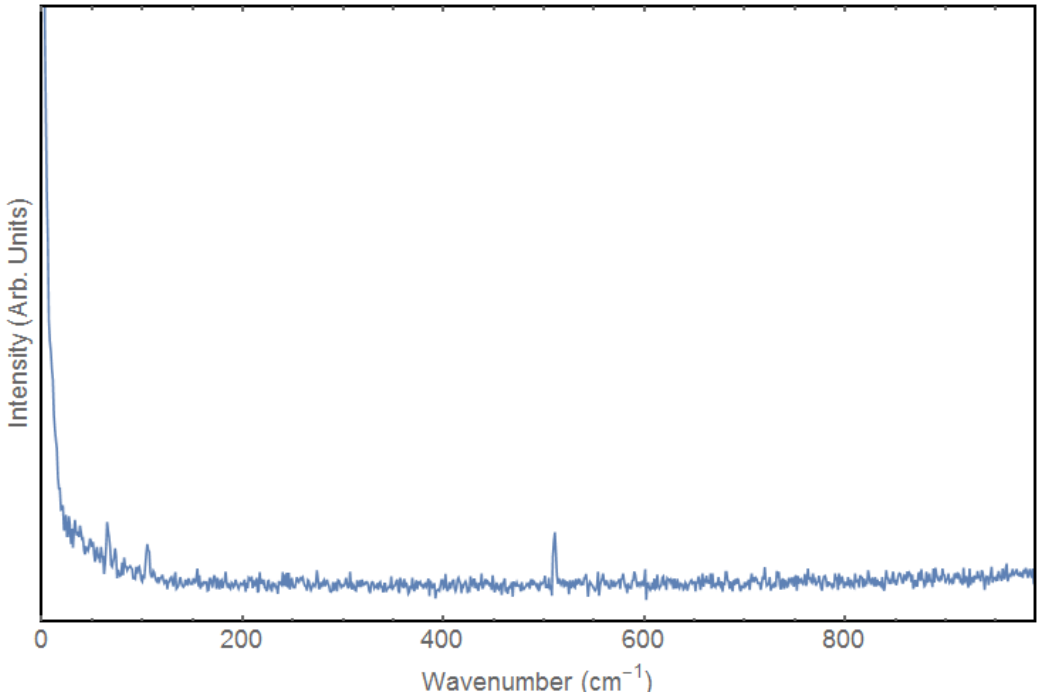

Figure 4.15: Room temperature Raman spectrum of PST ceramic #1 after completion of high temperature experiments. Collection time was five times that used in the high temperature Raman scattering experiments.

in this spectrum, with positions matching those in high temperature spectra.

4.2.2 PST Ceramic #2

Room Temperature Raman Scattering

Room temperature Raman scattering experiments were repeated on PST ceramic #2 under identical conditions to those used for PST ceramic #1. As with PST ceramic #1, this spectrum was taken over a range of 1000 cm^{-1}, starting with the wavenumber of the laser. This spectrum is shown in Figure 4.16. As with PST ceramic #1, four

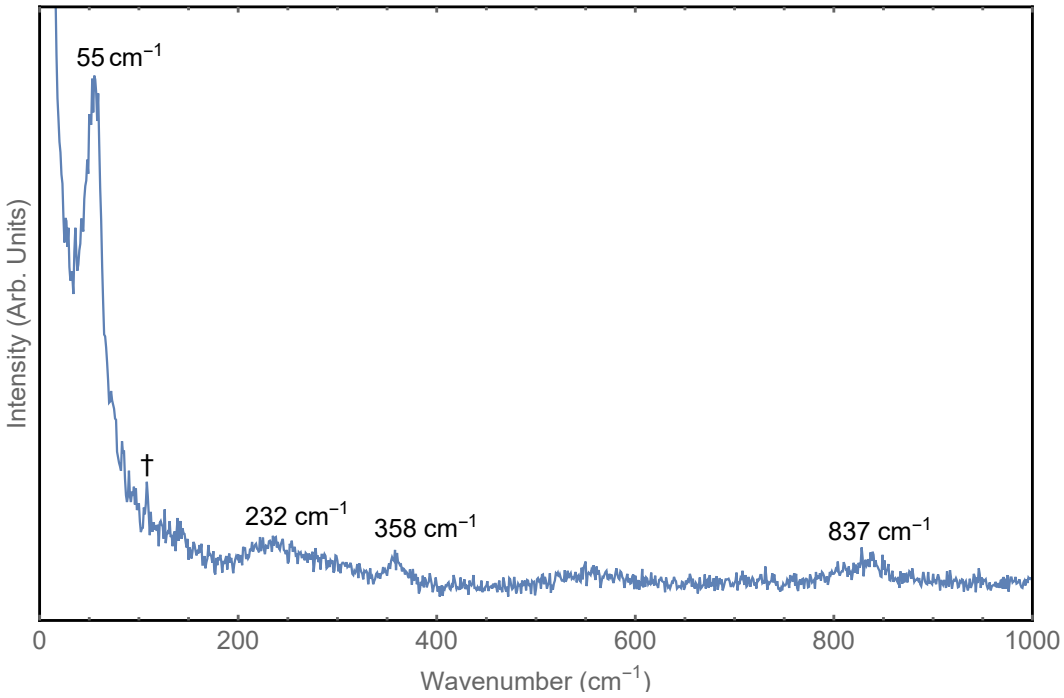

Figure 4.16: Raman spectra collected on PST ceramic #2 at room temperature. Peaks are labeled with Raman shift values, and peaks labeled with † are laser plasma lines.

peaks were found in this spectrum, and are listed in Table 4.4. The peak shifts were found to be very similar to those from PST ceramic #1, and are within 10% of the values for crystalline PST provided by Bismayer *et al*, with the exception of the F_{2g} mode. Interestingly, the plasma lines in this spectrum were significantly less pronounced than in the room temperature spectrum from PST ceramic #1, as there was only one strong plasma line, located around 110 cm^{-1}.

High Temperature Raman Scattering

Raman spectra were collected on PST ceramic #2 at temperatures ranging from 201°C to 653°C (see Figure 4.17). In these high temperature spectra, the F_{2g} mode was still the strongest peak. For this sample, the intensity of the F_{2g} mode in high temperature spectra was much closer to the intensity of the F_{2g} mode in the room temperature spectra, compared to PST ceramic #1. Furthermore, unlike PST ceramic #1, there was a decrease in peak intensity with increasing temperature, shown in Figure 4.18. Spectra shown in Figure 4.18 were collected with 1000 scans over a range of 100 cm^{-1}.

As with Raman shift, the linewidth of the F_{2g} peak of PST ceramic #2 is comparable to the linewidth of the F_{2g} PST ceramic #1, within their respective uncertainties, for overlapping temperature ranges.

Similar to PST ceramic #1, there were only three peaks observed in high temperature Raman scattering, as the F_{1g} peak was not observed. This is consistent with the results from PST ceramic #1. As is shown in Table 4.6, the Raman shift of the F_{2g} mode increased with increasing temperature, however the shift of the other peaks did not change significantly with temperature. From Figure 4.17, it can be seen that the intensity of the 358 cm^{-1} and 837 cm^{-1} peaks decreased with increasing temperature.

Unfortunately, once the high temperature cell reached 700°C, PST ceramic #2 exhibited signs of PbO loss. Upon removing the sample from the high temperature cell, the sample had changed colour, from a semi-transparent yellow-orange to a solid white colour. A comparison of colours is shown in Figure 4.19. Because of this, experiments on this sample concluded at 653°C.

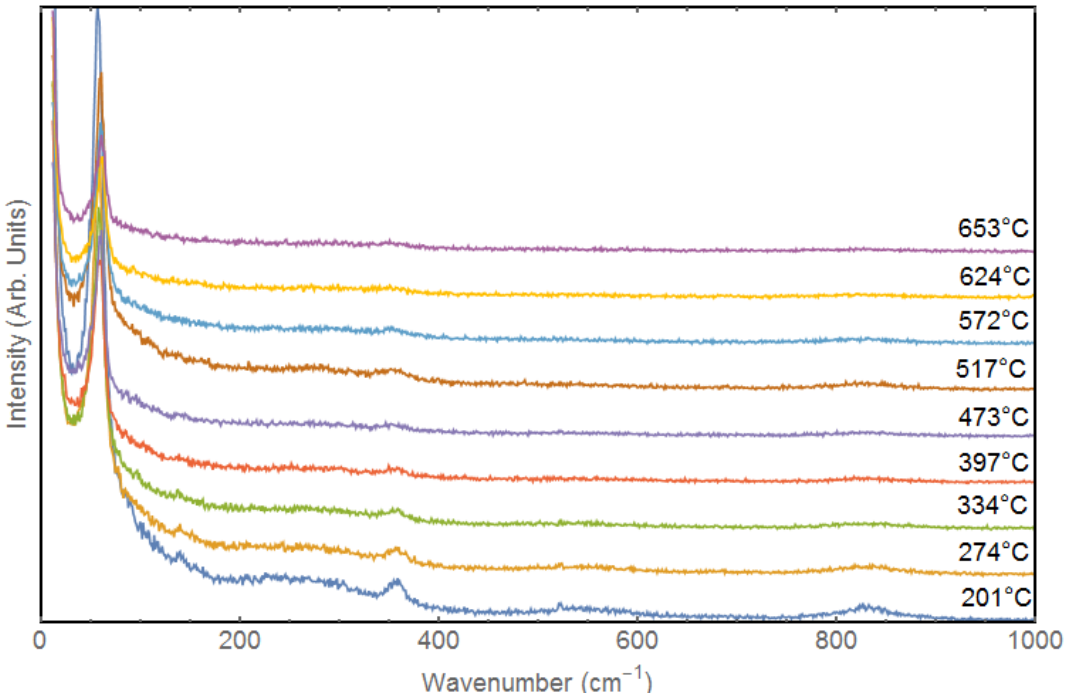

Figure 4.17: Raman spectra collected on PST ceramic #2 at temperatures ranging from 201 °C to 653°C, over a range of 990 cm^{-1}.

Table 4.6: Raman peak positions for PST #2 at all temperatures measured.

Temperature (°C)	F_{2g} (cm^{-1})	F_{1g} (cm^{-1})	F_{2u} (cm^{-1})	A_{1g} (cm^{-1})
25	55 ± 2	232 ± 10	358 ± 5	837 ± 10
201	56 ± 1	-	358 ± 3	832 ± 10
274	55 ± 1	-	356 ± 4	833 ± 10
340	57 ± 1	-	358 ± 3	839 ± 20
397	59 ± 2	-	349 ± 5	832 ± 20
453	60 ± 2	-	346 ± 10	835 ± 20
517	59 ± 2	-	351 ± 10	848 ±10
572	59 ± 2	-	353 ± 10	832 ± 20
624	60 ± 2	-	347 ± 10	-
653	60 ± 2	-	350 ± 10	-

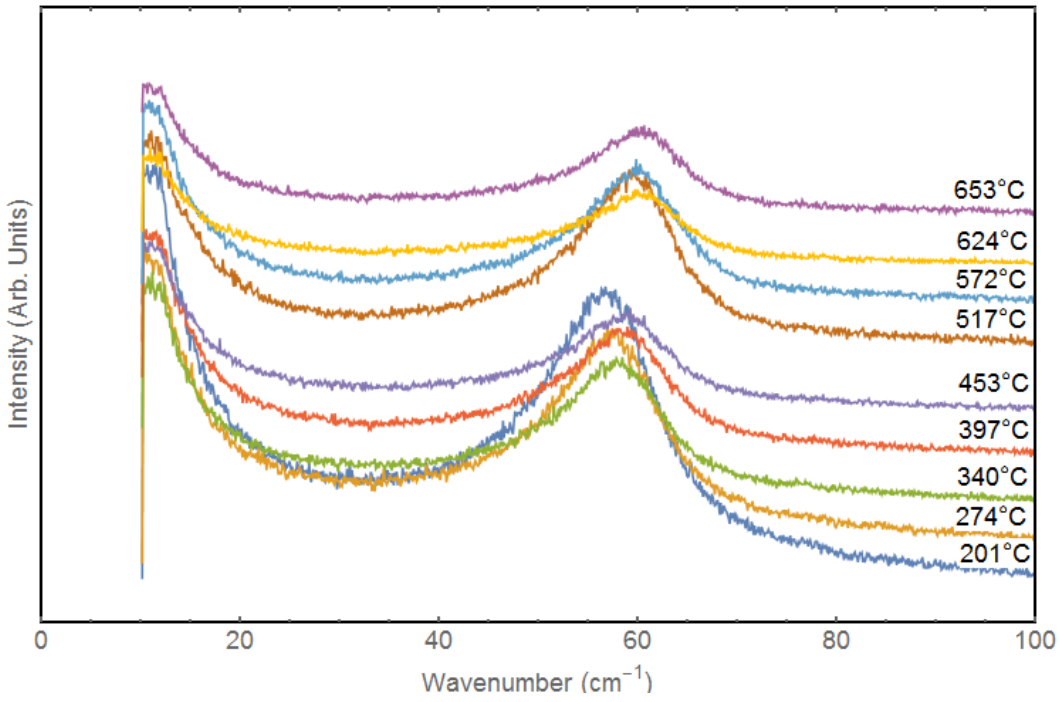

Figure 4.18: Raman spectra collected on PST ceramic #2 at temperatures ranging from 201 °C to 653°C, over a range of 100 cm^{-1}.

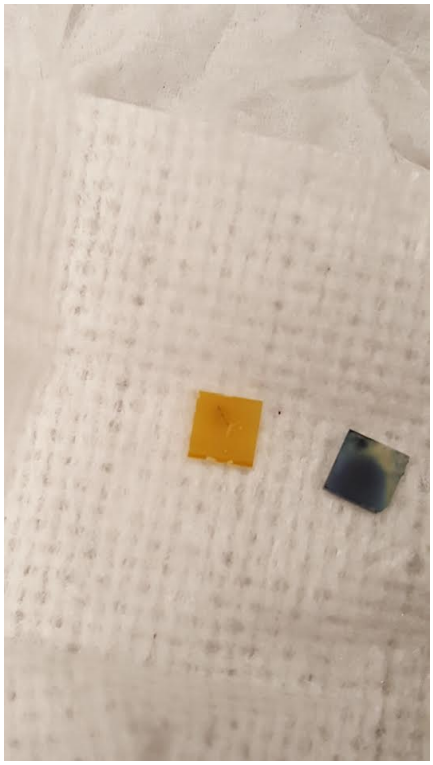

Figure 4.19: PST ceramic # 2 before high temperature experiments (left) and after high temperature experiments (right).

4.2.3 General Discussion

The F_{2g} mode peak positions of PST ceramic, shown in Figure 4.20, highlight the change in Raman shift with respect to temperature from room temperature to 1200°C. Between room temperature and ∼250°C, there is little change in Raman shift of the F_{2g} mode peak. The Raman shift of the F_{2g} mode of ceramic PST increased with increasing temperature between ∼250°C and ∼450°C. Between ∼450 °C and 900 °C, the frequency of the F_{2g} showed little change with temperature. Above 900 °C, there

was a large and abrupt increase in Raman shift of the F_{2g} mode peak. The intensity of this peak was significantly weaker in the spectra collected above 900°C, compared to lower temperature spectra. This gave rise to a much larger uncertainty associated with these peak positions. These changes in the F_{2g} mode peak have been attributed to the loss of PbO in the ceramic at high temperatures, as these effects were only observed at temperatures at which PbO loss was observed in the PST ceramic.

Figure 4.20 also shows Raman shifts of the F_{2g} mode collected from previous studies. For PST thin films [37] and crystalline PST [20, 14], Raman shift of the F_{2g} mode decreases with increasing temperature below 0°C. Above 0°C, the frequency shift of the F_{2g} mode from crystalline PST increases with increasing temperature [20]. This change in frequency shift with temperature is attributed to distortions of the lattice parameter. The temperature where frequency shift changes from decreasing with increasing temperature to increasing with increasing temperature corresponds to the paraelectric-ferroelecteric phase transition near 0°C.

The results collected from ceramic PST in this study were exclusively collected above the transition temperature. The change in Raman shift of the F_{2g} peak of ceramic PST with temperature shows the same general trend as those collected by Mihailova *et al*. at temperatures greater than 0°C.

The full width at half maximum of the F_{2g} mode for ceramic and crystalline PST is shown in Figure 4.21 for the temperature range -273°C - 1200 °C. As is shown, the Raman linewidth of the F_{2g} mode of the PST ceramic was smaller at high temperatures, compared to room temperature. Figure 4.21 shows a decrease in Raman peak linewidth of the F_{2g} mode of ceramic PST with increasing temperature for temperatures between room temperature and 900°C. Between 450 °C and 900 °C,

there was relatively little change in linewidth, where all values fell within the range of 11 cm^{-1} to 17 cm^{-1}. Interestingly, this sharp transition occurs at about the same temperature as the transition between increasing F_{2g} peak shift with temperature and relatively constant F_{2g} peak shift. At 900 °C and above, where the peak due to the F_{2g} mode was significantly weaker, the linewidth was noticeably smaller. For ceramic PST, the linewidth of the F_{2g} mode was significantly different than that measured on crystalline PST by Bismayer *et al.* for temperatures between room temperature and 200°C [14]. The linewidth of this mode from the previous study increased with increasing temperature from -173°C to room temperature. As with Raman shift, at temperatures larger than room temperature, the linewidth remained relatively constant. This occurred for both ordered crystalline PST and disordered crystalline PST.

At low temperatures (-171°C - 0°C), Bismayer *et al.* observed two additional peaks on the shoulders of the F_{2g} mode peak [14]. These peaks became hidden as temperature increased, and the F_{2g} mode peak intensity increased, and were not observed at room temperature. This splitting of the F_{2g} mode peak was also observed in polarized Raman spectra collected by Mihailova *et al* [20]. These peaks were not observed in any Raman spectra collected on PST ceramics, as the temperature range was larger than the temperatures at which these peaks were seen. This is likely the cause of the difference between the linewidth of the F_{2g} mode peak in ceramic PST and the F_{2g} mode peak in crystalline PST from Bismayer *et al.* [14].

Figure 4.22 shows the Raman shift of the F_{2u} peak at temperatures ranging from room temperature to 850 °C. In the work by Setter *et al.* on crystalline PST, the Raman shift of this peak remained constant after various heat treatments [19]. As

was shown in Figure 4.17, the intensity of these peaks decreased with increasing temperature. As such, at high temperatures, these peaks were significantly weaker and wider than in the room temperature spectrum, making it impossible to obtain reliable estimates of full width at half maximum.

Figure 4.23 shows Raman shift of the A_{1g} mode at temperatures ranging from room temperature to 704°C for PST ceramics. Over this temperature range, the Raman shift of the peak remained relatively unchanged. The shift values are comparable to the values measured on crystalline PST by Mihailova *et al*, where the Raman shift of this peak also remained constant over a temperature range of 157°C - 467°C. In crystalline PST, this mode is generated by symmetric stretching of the BO_6 octahedra. Since the ceramic is polycrystalline, the crystal grains which form the ceramic experience the same bond stretching. As with the F_{2u} mode, the intensity of the A_{1g} mode was significantly smaller at high temperatures, compared to room temperature, therefore the full width at half maximum could not be measured.

In high temperature spectra (T > 200°C), the intensity of the F_{2g}, F_{2u}, and A_{1g} peaks was less than observed at room temperature. The cause of this decrease in relative intensity is unknown. It should be noted, however, that the intensity of the F_{2g} mode for crystalline PST was shown by Lushnikov *et al*. to decrease with increasing temperature [17]. It is possible that the reason for this decrease in intensity is similar to that for the F_{1g} mode peak, as previously discussed.

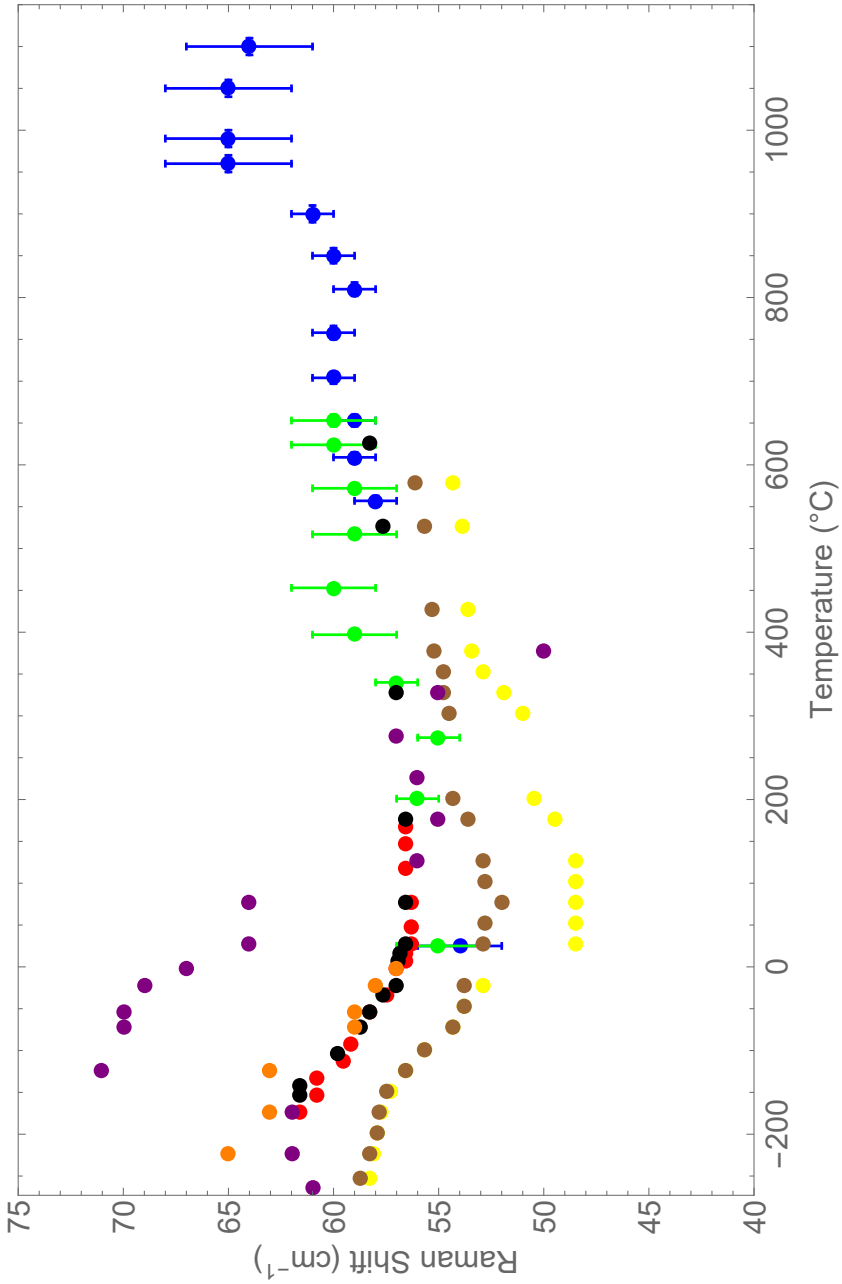

Figure 4.20: Raman shift of the F_{2g} mode of PST at temperatures ranging from -273 °C to 1100 °C. Blue - Ceramic #1 (Present Work), Green - Ceramic #2 (Present Work), Red - Ordered Crystal [14], Black - Disordered Crystal [14], Yellow - Crystal (Parallel Polarized) [20], Brown - Crystal (Cross Polarized) [20], Orange - 78% Ordered Film [37], Purple - Disordered Film [37].

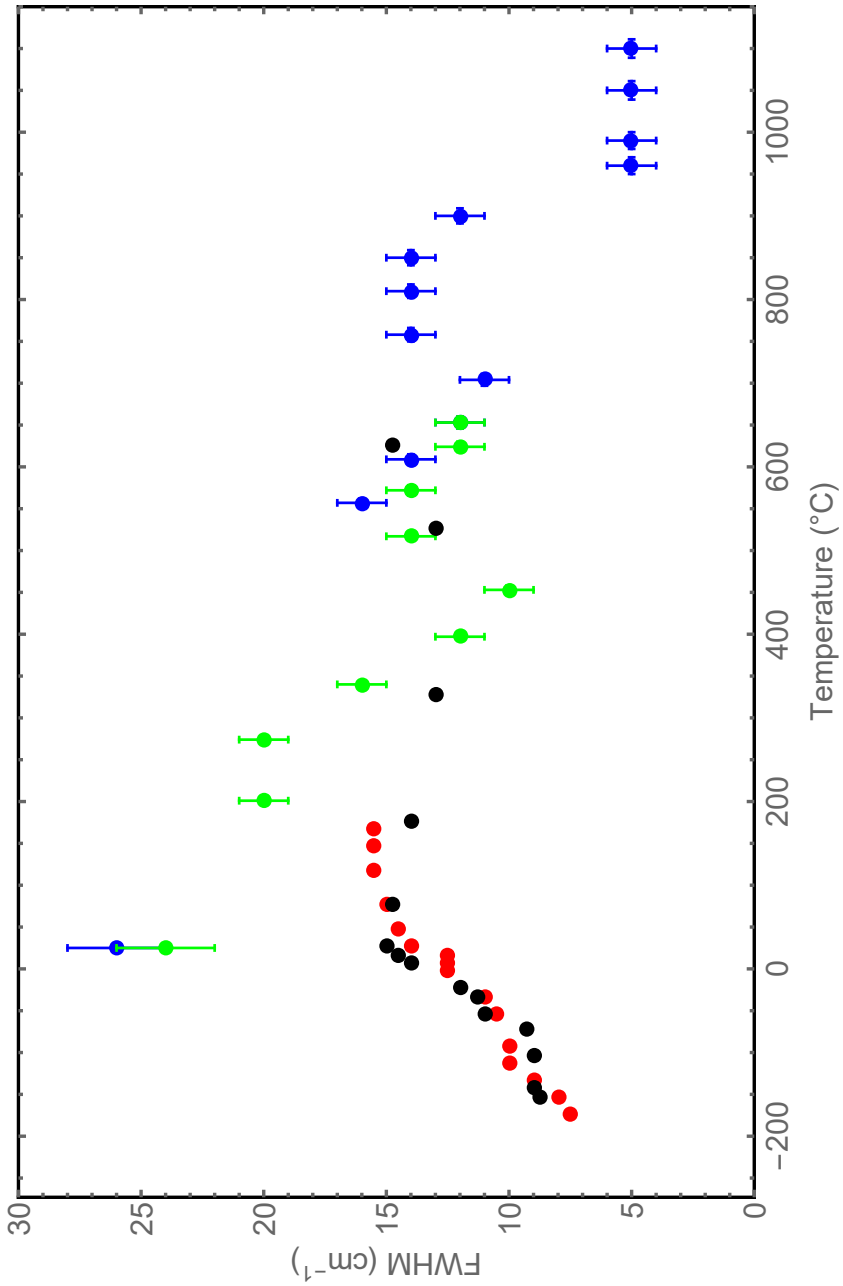

Figure 4.21: FWHM of the F_{2g} mode of PST at temperatures ranging from -273 °C to 1100 °C. Blue - Ceramic #1 (Present Work), Green - Ceramic #2 (Present Work), Red - Ordered Crystal [14], Black - Disordered Crystal [14].

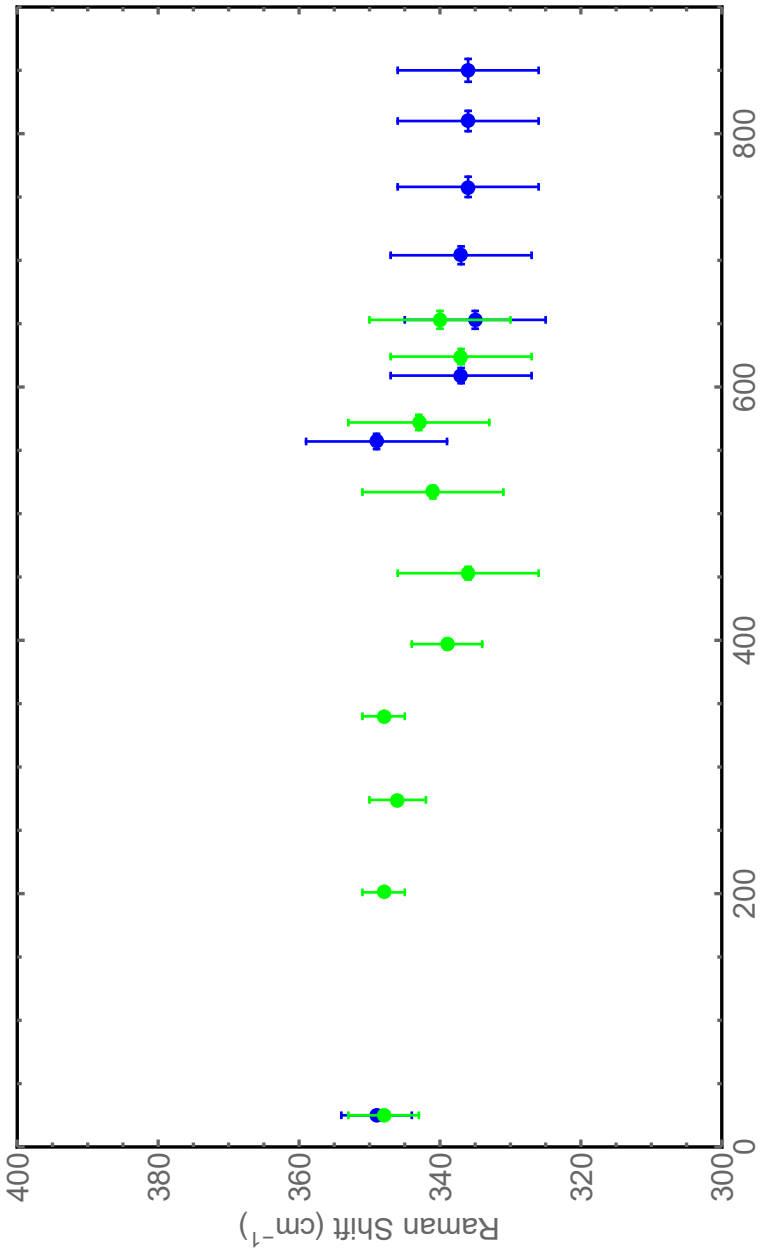

Figure 4.22: Raman shift of the 349 cm^{-1} F_{2u} mode of ceramic PST#1 (Blue) and 348 cm^{-1} F_{2u} mode of ceramic PST#2 (Green) at temperatures ranging from room temperature °C to 850 °C.

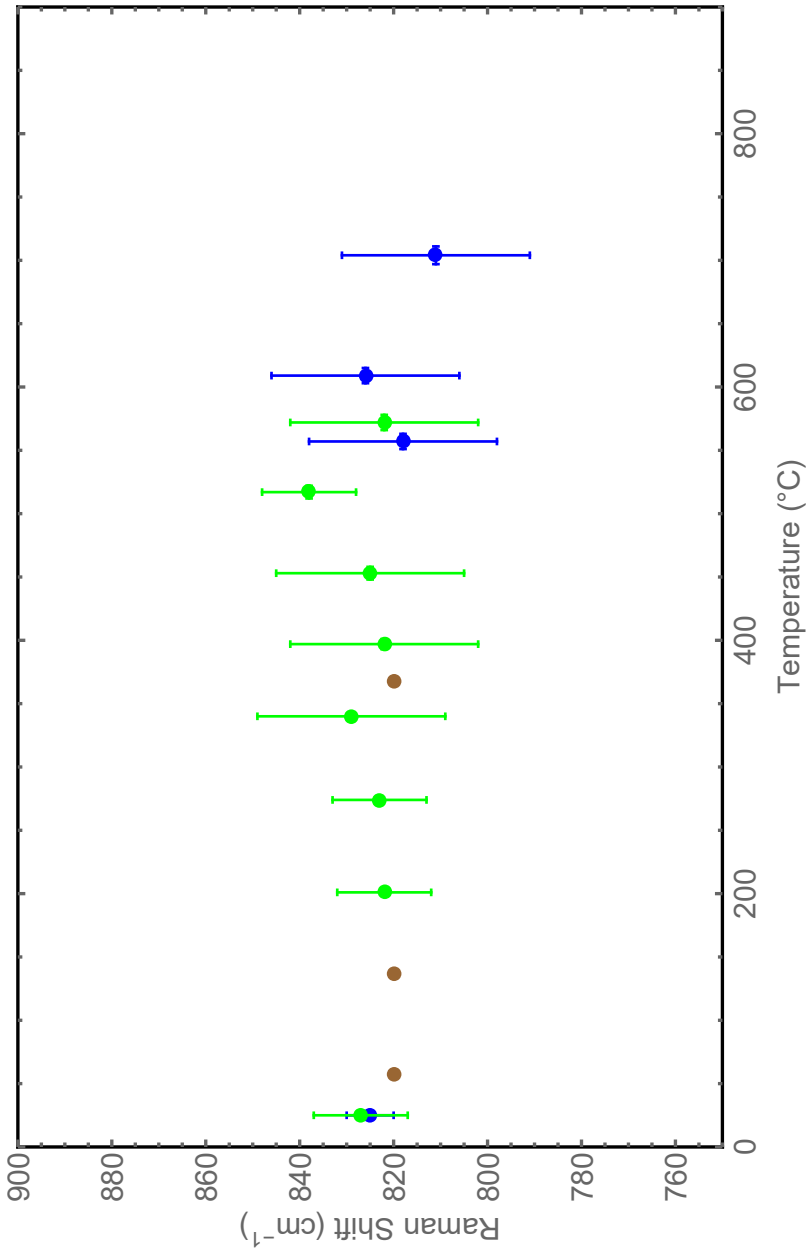

Figure 4.23: Raman shift of the 825 cm^{-1} A_{1g} mode of ceramic PST#1 (Blue), 827 cm^{-1} A_{1g} mode of ceramic PST#2 (Green), and the 850 cm^{-1} A_{1g} mode of crystalline PST (Brown) [20] at temperatures ranging from room temperature to 850 °C.

Chapter 5

Conclusion

5.1 Summary

Inelastic light scattering studies were performed on PST ceramic samples over a range of temperatures. Brillouin light scattering was used to probe acoustic phonons at room temperature and Raman light scattering was used to probe optical phonons at room temperature and higher temperatures.

Brillouin light scattering experiments were performed on PST ceramics with angles of incidence ranging from 20° to 70°. Two peaks were found in these spectra. The frequency shift of these peaks showed no dependence on angle of incidence, therefore both of these Brillouin peaks were determined to be due to bulk modes. The peak with lower frequency shift was determined to be due to the transverse bulk mode, and the peak with the higher frequency shift was determined to be due to the longitudinal bulk mode.

Using the average frequency shift of the respective bulk modes for PST ceramic

#1, Equation (2.16) was used to calculate the velocity of the respective phonons. The velocity for the transverse bulk mode was found to be $v_T = 2600 \pm 100$ m/s, and the velocity of the longitudinal bulk mode was found to be $v_L = 4600 \pm 100$ m/s. These values were comparable to values provided by literature for crystalline PST. Using the relations provided in Equations (2.30) and (2.31), respectively, independent elastic constants were calculated to be $c_{11} = 198 \pm 8$ GPa and $c_{44} = 61 \pm 5$ GPa. Due to the isotropy of the material, Equation (2.32) was used to calculate elastic constant, $c_{12} = 70 \pm 20$ GPa. The values for the three elastic constants were all similar to the values provided by literature for PST crystals.

For PST ceramic #2, average frequency shift of the bulk modes was used to calculate the bulk mode velocities of the respective modes. The velocity of the transverse bulk mode was calculated to be $v_T = 2750 \pm 90$ m/s. This value is lower than the values for crystalline PST from literature, however it is within uncertainty of the value calculated for the PST ceramic #1. The longitudinal bulk mode velocity was found to be $v_L = 4700 \pm 100$ m/s. This value is also within uncertainty of the value calculated for PST #1, and is comparable to values for crystalline PST provided by literature. The values for transverse and longitudinal bulk mode velocities were used to calculate independent elastic constants c_{44} and c_{11}, respectively. The values calculated were $c_{11}= 200 \pm 9$ GPa and $c_{44} = 68 \pm 4$ GPa. These values are similar to the values calculated for PST ceramic #1, however only the value for c_{11} is similar to the values provided by literature for crystalline PST. These values were then used to calculate $c_{12} = 60 \pm 20$ GPa, which is within uncertainty of the value calculated for PST ceramic #1.

The similarities between the elastic constants calculated for the PST ceramics from

this study and PST crystals used in previous studies comes from the polycrystalline nature of the ceramic (consisting of crystalline grains with random orientation).

PST ceramic was coated with a 40 nm layer of aluminum by vacuum deposition using a commercial DC magnetron sputtering system. Brillouin light scattering experiments were performed on this coated ceramic to attempt to observe surface acoustic modes. Spectra collected from this sample showed an additional Brillouin doublet located at $f_R = \pm 10.71$ GHz, which was not seen in uncoated samples. The velocity of this possible surface mode was calculated to be $v_R = 3317$ m/s. Due to degradation of the Al coating, this possible surface mode could not be further explored.

Raman light scattering experiments were performed at room temperature on PST ceramic #1. Four peaks, due to the F_{2g}, F_{1g}, F_{2u}, and A_{1g} modes, were observed in the room temperature spectrum, the latter three of which were within 10% of the values given by literature for PST crystals. The peak with the smallest Raman shift was determined to be the F_{2g} mode and was significantly more intense than the latter three peaks.

Room temperature Raman light scattering experiments were also performed on PST ceramic #2. Four peaks were also found in this spectrum, were very similar to the frequency shifts found for PST ceramic #1. Furthermore, high temperature experiments were performed on this sample, ranging from 201°C to 653°. Similar to PST ceramic #1, the peak found at 232 ± 10 cm^{-1} at room temperature was not observed in any spectra. Over this temperature range, the frequency shift of the F_{2g} mode noticeably increased and its linewidth decreased with increase in temperature, however there was no change in frequency shift for the peaks found at 358 ± 5 cm^{-1} and 837 ± 10 cm^{-1} in the room temperature spectrum.

Considering the data for both PST ceramic samples as a whole, the Raman shift of the F_{2g} mode showed four distinct regions with increasing temperature. Between room temperature and 250°, there was little change in Raman shift with change in temperature. Between 250°C and 450°C, the Raman shift of the F_{2g} mode increased with increasing temperature. From 450°C and 900°C, Raman shift remained relatively constant with increasing temperature. This is comparable to results from previous studies on crystalline PST at temperatures above the phase transition temperature. This increase in frequency shift is caused by distortions in the lattice parameter. The final region, above 900°C showed a large increase in Raman shift, caused by the loss of PbO in the sample.

Full width at half maximum was measured for the F_{2g} mode of PST. Full width at half maximum decreased with increasing temperature from room temperature to 450°C. Between 450°C and 900°, the full width at half maximum showed no significant change with increasing temperature. The values calculated for ceramic PST were characteristically less than values provided for crystalline PST, which has been attributed to the existence of two shoulder peaks of the F_{2g} mode. Above 900°C, the full width at half maximum dropped significantly. This was attributed to PbO loss in the ceramic.

The F_{1g} mode, located at 230 $\pm$ 10 cm^{-1} and 232 $\pm$ 10 cm^{-1} for PST ceramics #1 and #2, respectively, were not observed at high temperatures. This result is not unexpected, as the intensity of the F_{1g} mode decreases significantly with increasing temperature.

The frequency of the F_{2u} mode remained constant at all temperatures for both samples. This Raman shift peak has been shown, in previous work, to remain constant

through various heat treatments.

The shift of the peak located at ∼835 cm^{-1} in Raman spectra from PST ceramics, the A_{1g} mode, also remained constant through all temperatures in ceramic PST. The Raman shift of this peak overlapped with frequencies found for the A_{1g} mode in crystalline PST at various temperatures.

5.2 Future Work

Due to the open-ended nature of temperature dependent studies, there are many experiments that can be done to complement this work. Firstly, Brillouin light scattering experiments can be performed on PST ceramics over the temperature range performed in Raman experiments to observe the change in the elastic properties at high temperatures. Raman scattering experiments can be performed at higher temperatures, in a PbO rich environment to avoid loss, to further observe the high temperature evolution of the F_{2g} mode. Furthermore, Raman scattering experiments can be performed on PST ceramics in an attempt to observe the behaviour of the F_{2g} mode at temperatures below the ferroelectric-paraelectric phase transition, at ∼20°C. Finally, the experiments performed in this work can be performed on PST crystals to compare to the results obtained from ceramics.

Appendix A

PST#1 Spectra

A.1 Brillouin Spectra

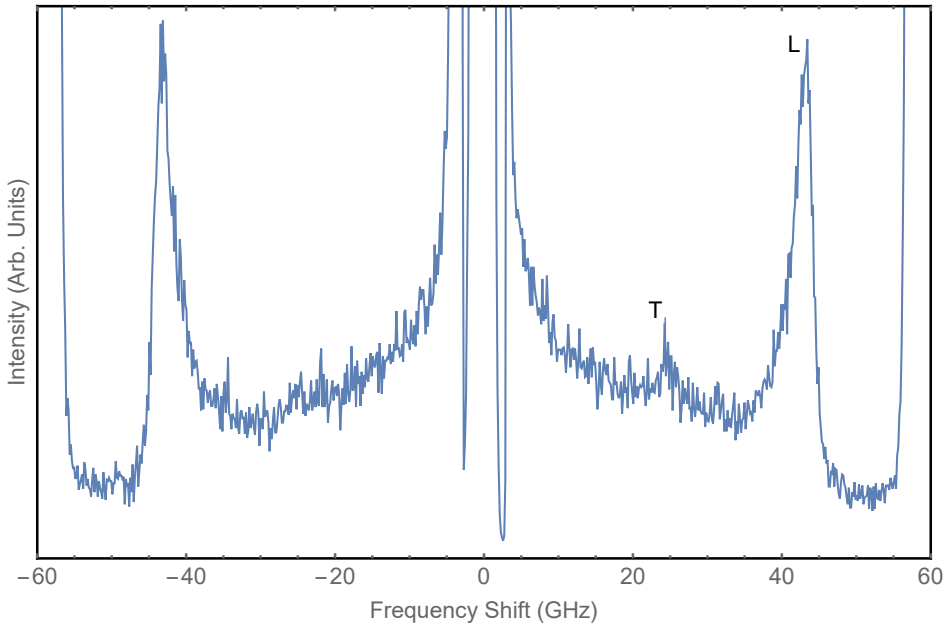

Figure A.1: Brillouin spectrum collected on PST ceramic #1 with an angle of incidence of 20°, from Figure 4.1.

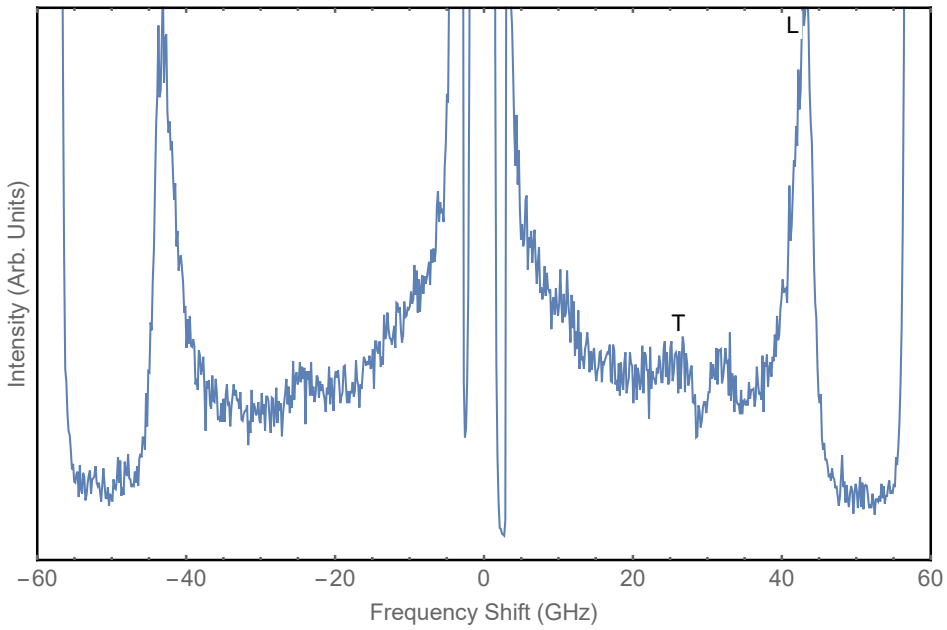

Figure A.2: Brillouin spectrum collected on PST ceramic #1 with an angle of incidence of 30°, from Figure 4.1.

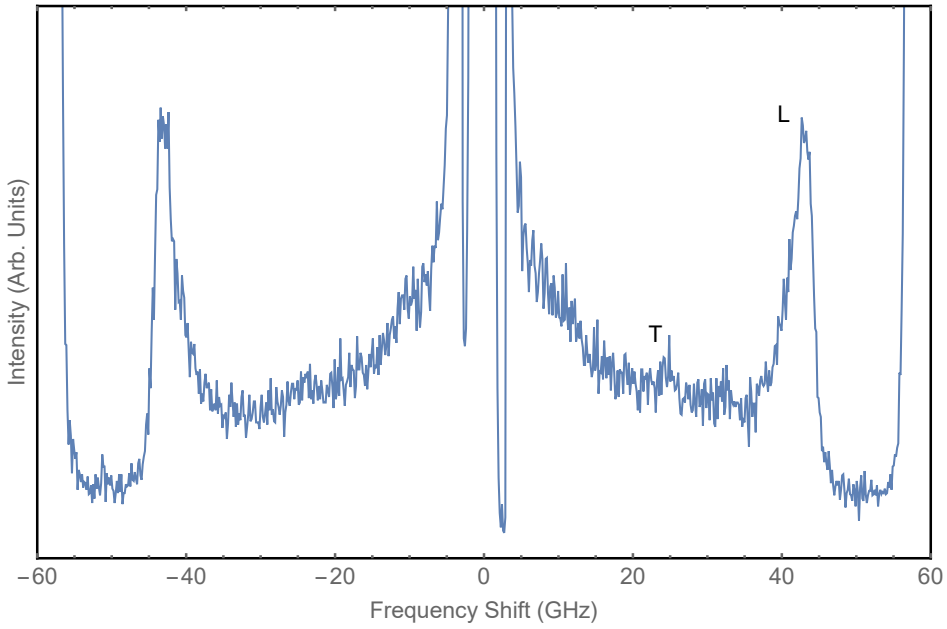

Figure A.3: Brillouin spectrum collected on PST ceramic #1 with an angle of incidence of 40°, from Figure 4.1.

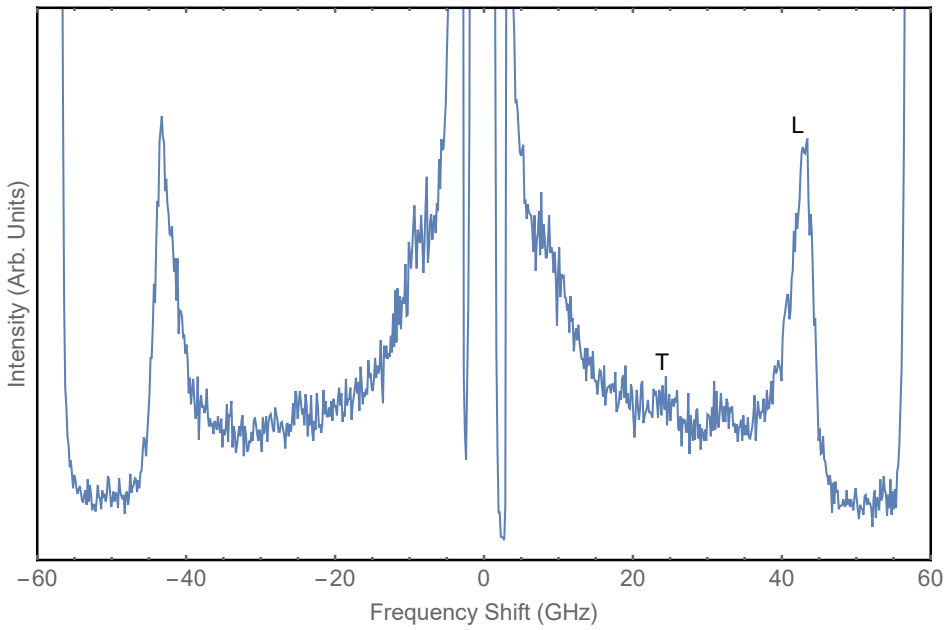

Figure A.4: Brillouin spectrum collected on PST ceramic #1 with an angle of incidence of 50°, from Figure 4.1.

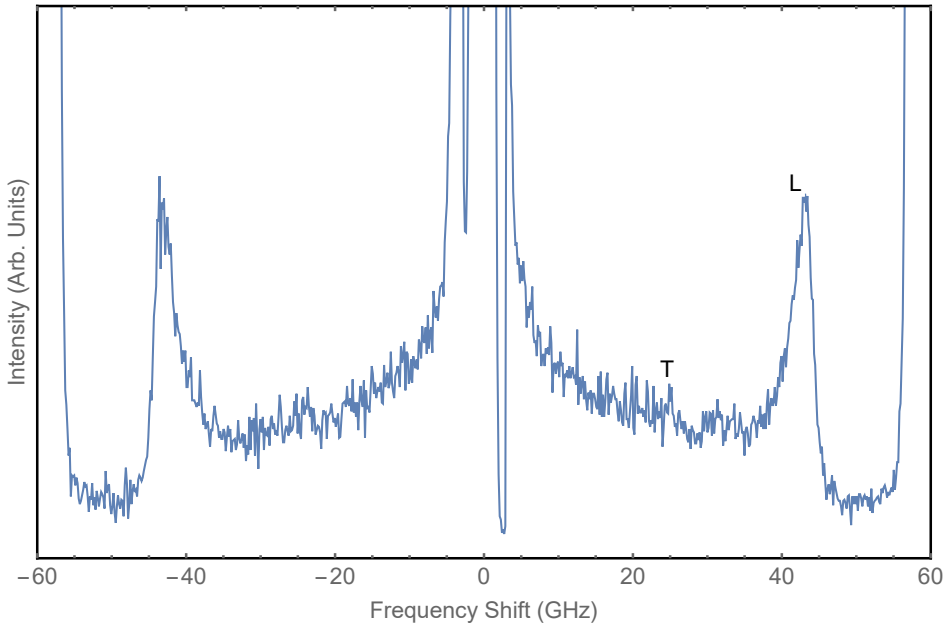

Figure A.5: Brillouin spectrum collected on PST ceramic #1 with an angle of incidence of 60°, from Figure 4.1.

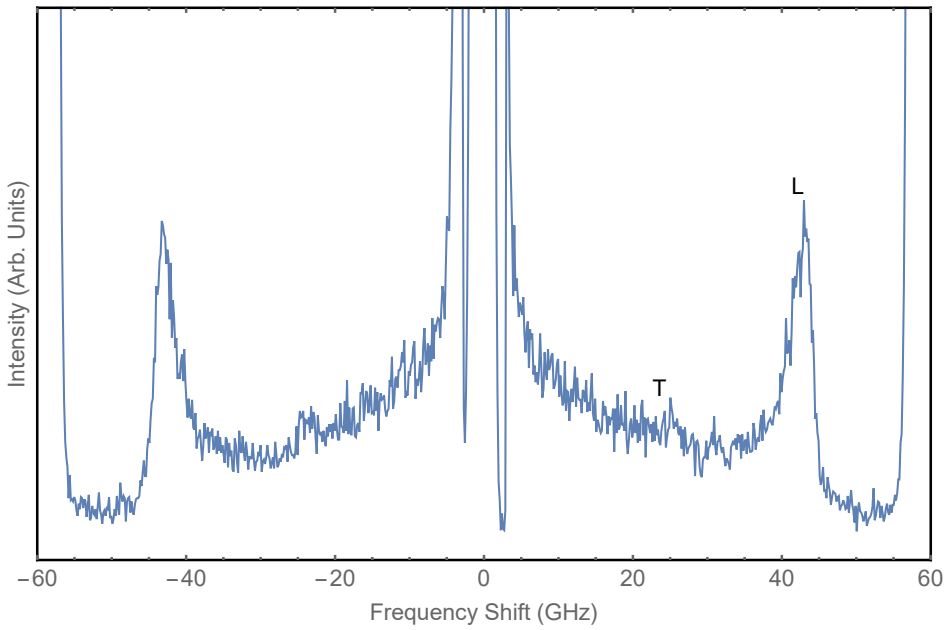

Figure A.6: Brillouin spectrum collected on PST ceramic #1 with an angle of incidence of 70°, from Figure 4.1.

A.2 Raman Spectra

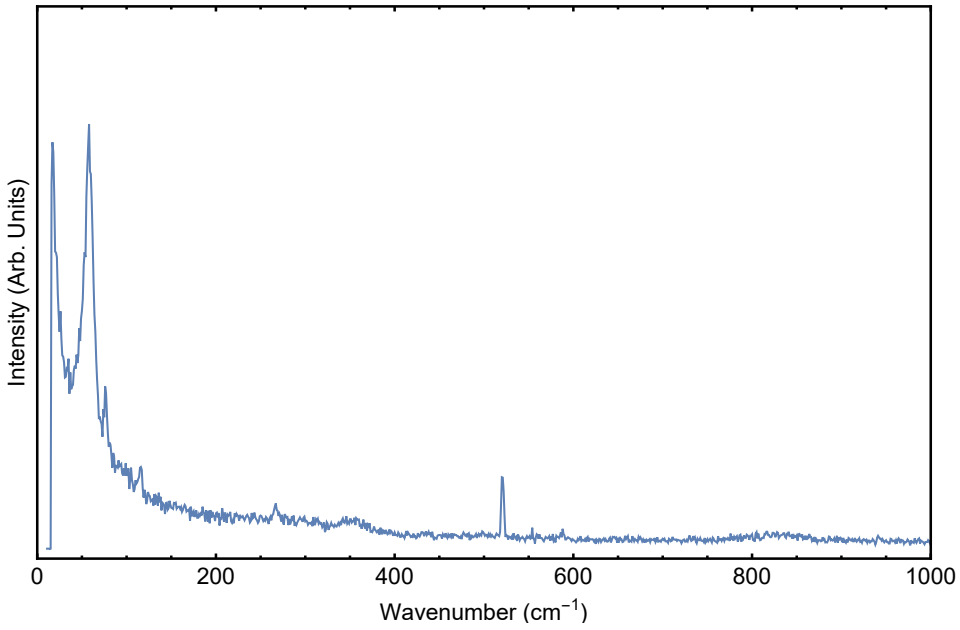

Figure A.7: Raman spectrum collected on PST ceramic #1 at 557°C, from Figure 4.8.

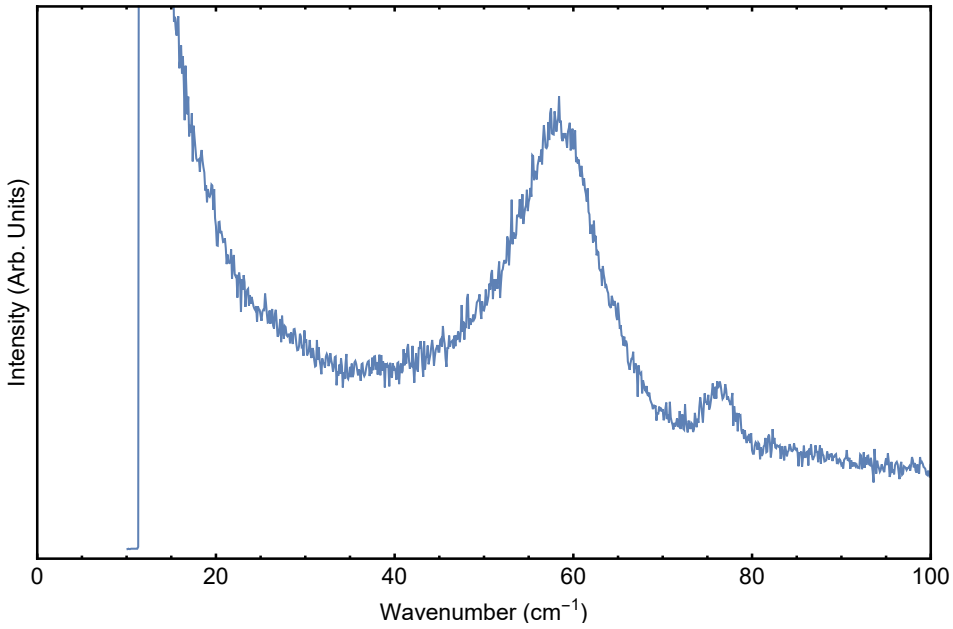

Figure A.8: Raman spectrum collected on PST ceramic #1 at 557°C, from Figure 4.9.

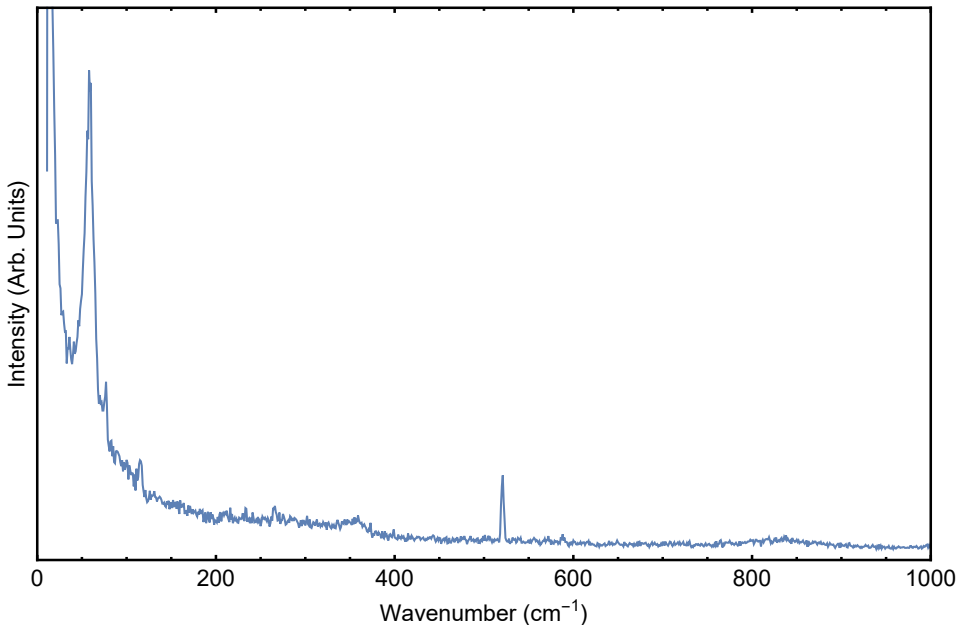

Figure A.9: Raman spectrum collected on PST ceramic #1 at 605°C, from Figure 4.8.

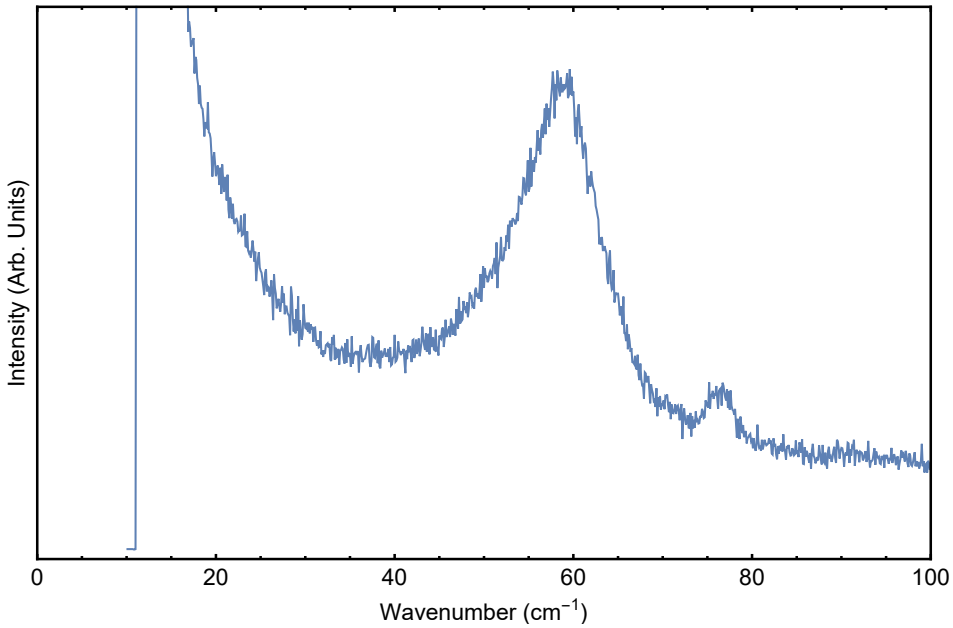

Figure A.10: Raman spectrum collected on PST ceramic #1 at 605°C, from Figure 4.9.

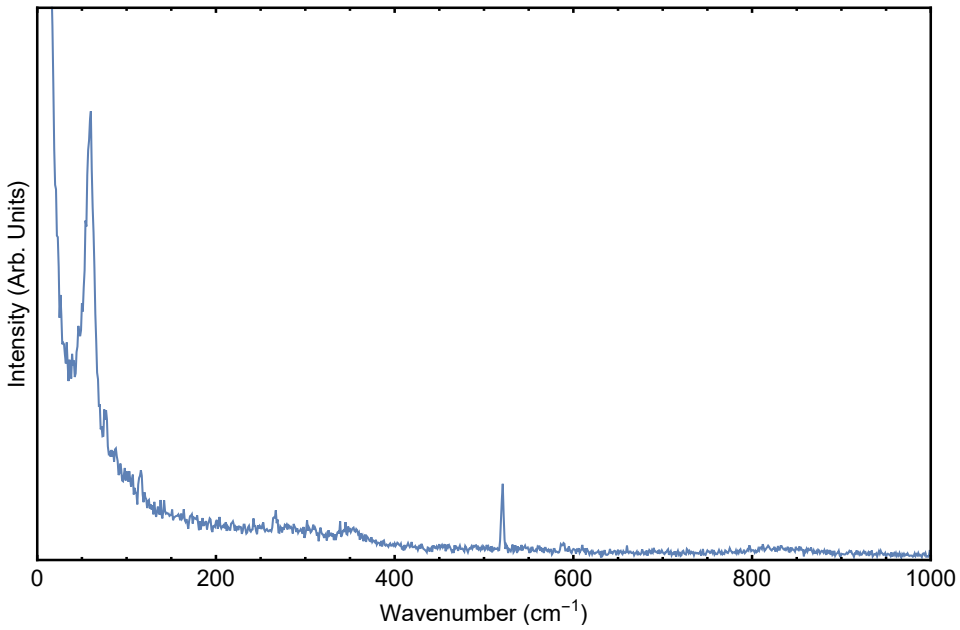

Figure A.11: Raman spectrum collected on PST ceramic #1 at 653°C, from Figure 4.8.

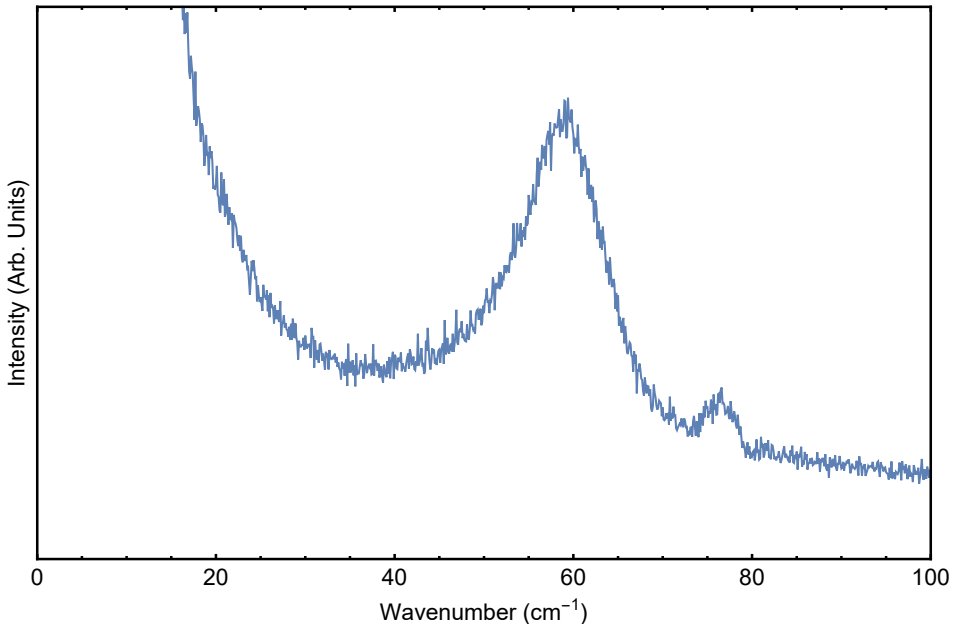

Figure A.12: Raman spectrum collected on PST ceramic #1 at 653°C, from Figure 4.9.

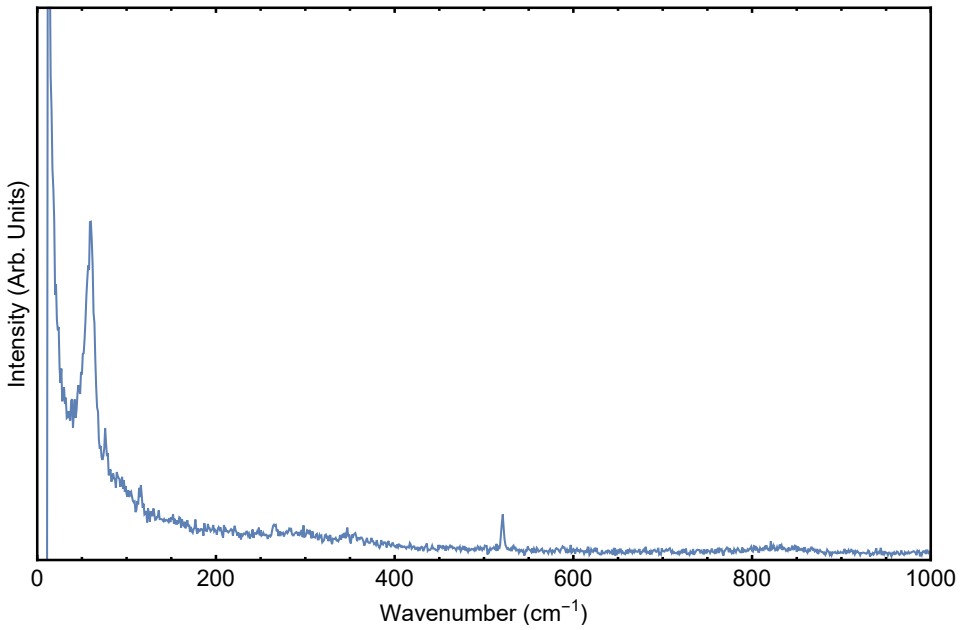

Figure A.13: Raman spectrum collected on PST ceramic #1 at 704°C, from Figure 4.8.

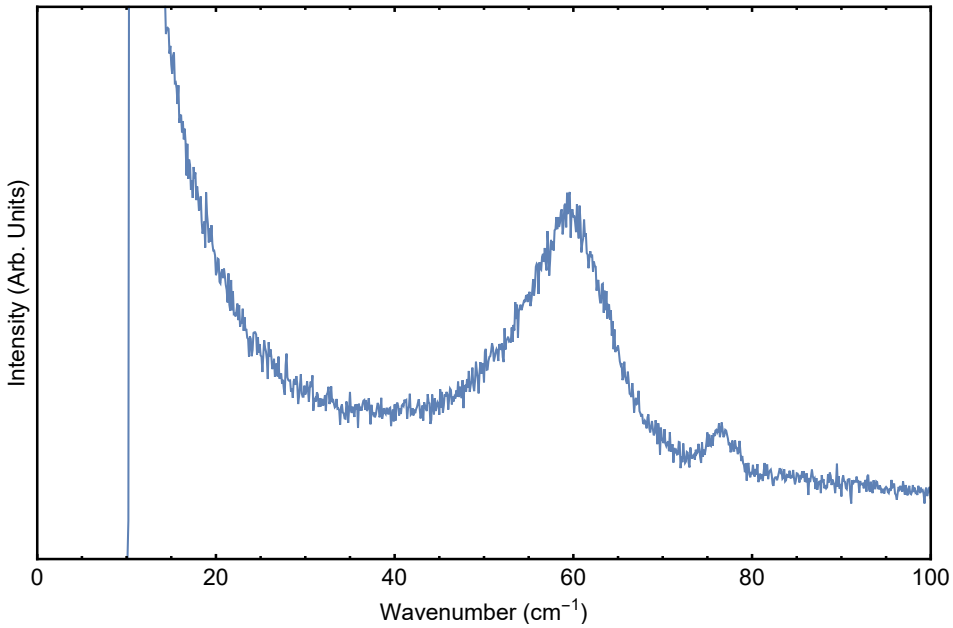

Figure A.14: Raman spectrum collected on PST ceramic #1 at 704°C, from Figure 4.9.

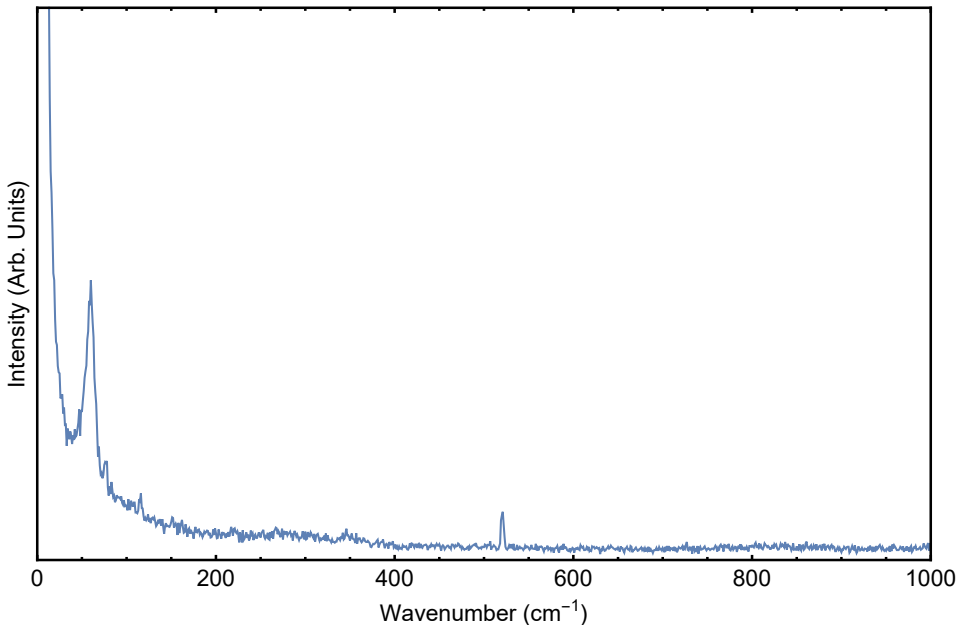

Figure A.15: Raman spectrum collected on PST ceramic #1 at 758°C, from Figure 4.8.

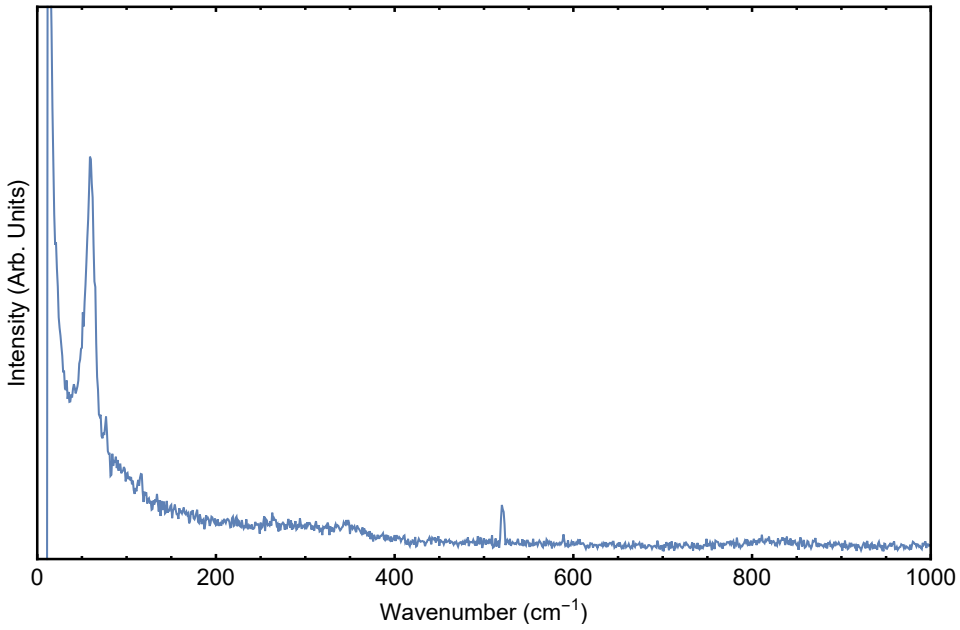

Figure A.16: Raman spectrum collected on PST ceramic #1 at 810°C, from Figure 4.8.

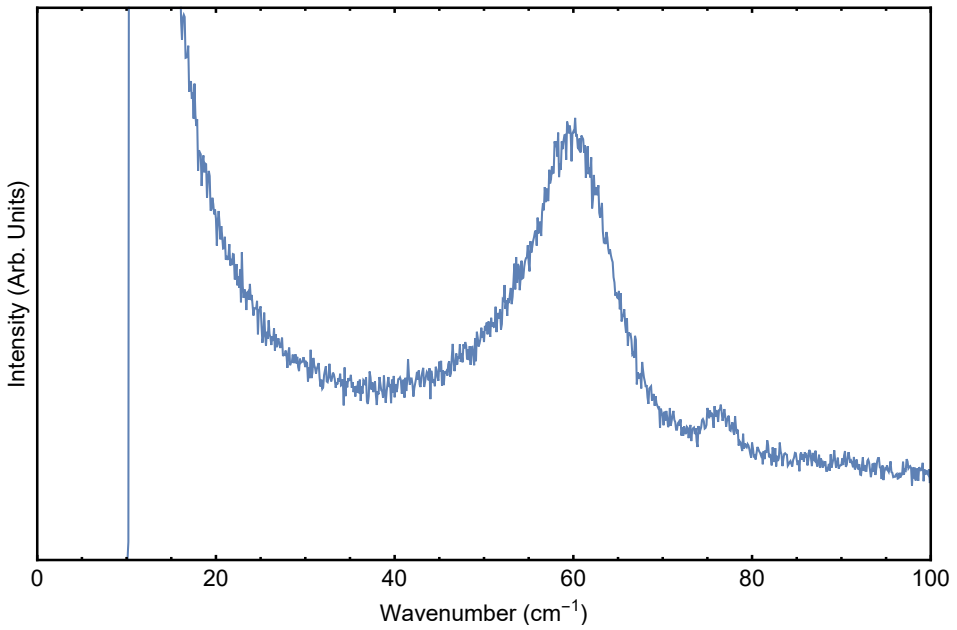

Figure A.17: Raman spectrum collected on PST ceramic #1 at 810°C, from Figure 4.9.

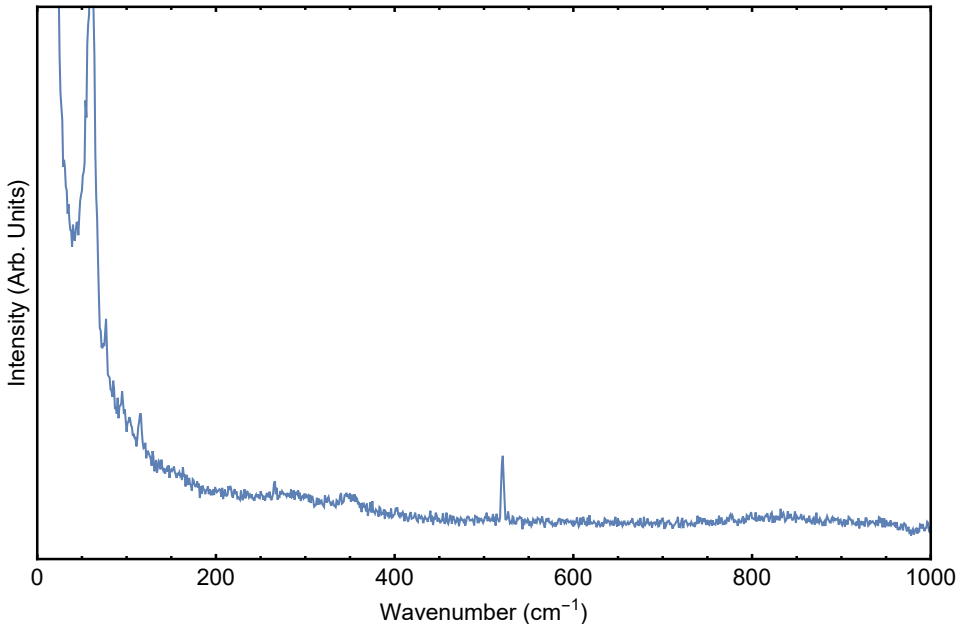

Figure A.18: Raman spectrum collected on PST ceramic #1 at 850°C, from Figure 4.8.

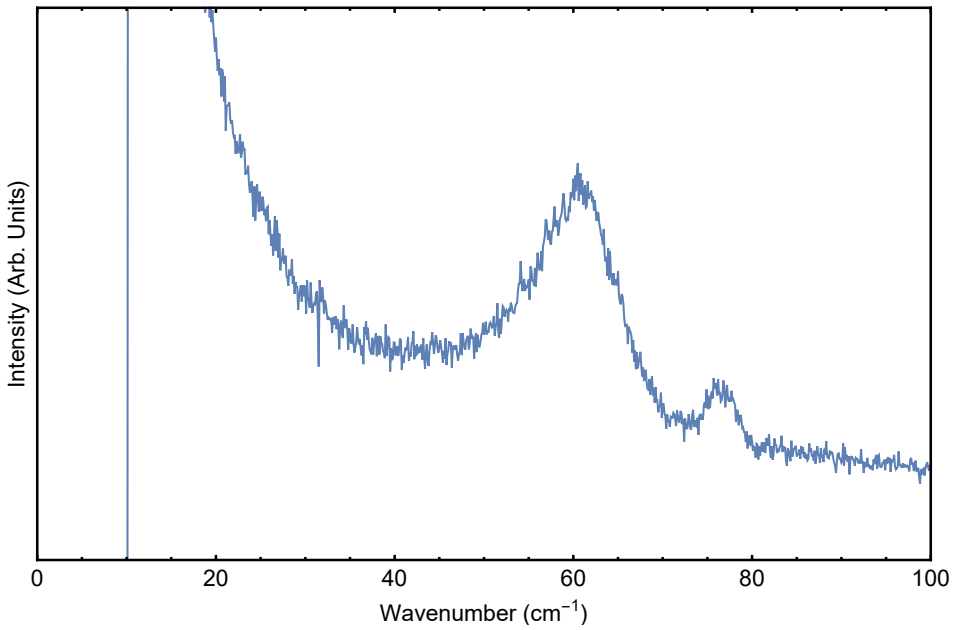

Figure A.19: Raman spectrum collected on PST ceramic #1 at 850°C, from Figure 4.9.

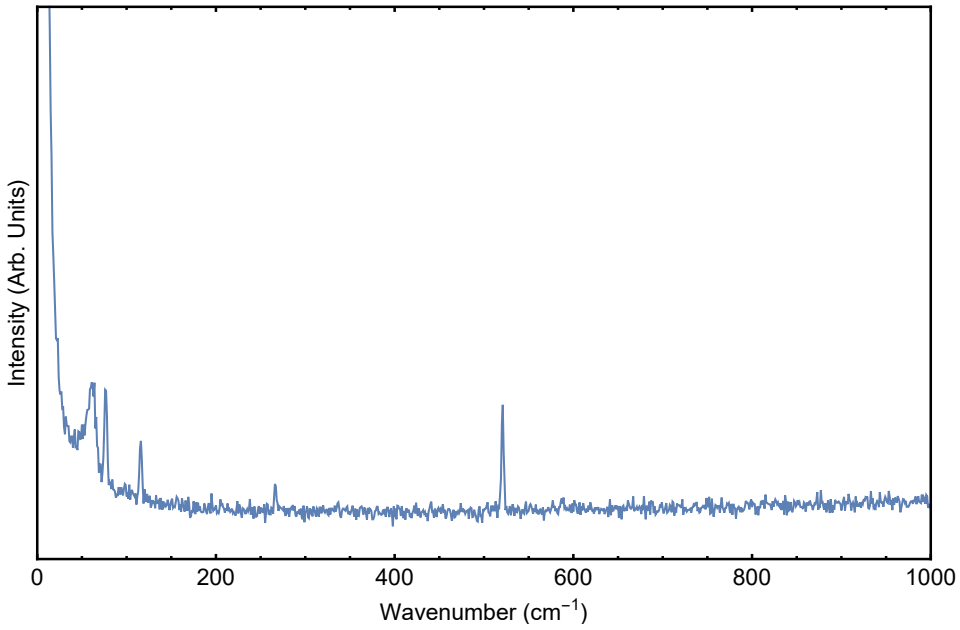

Figure A.20: Raman spectrum collected on PST ceramic #1 at 900°C, from Figure 4.10.

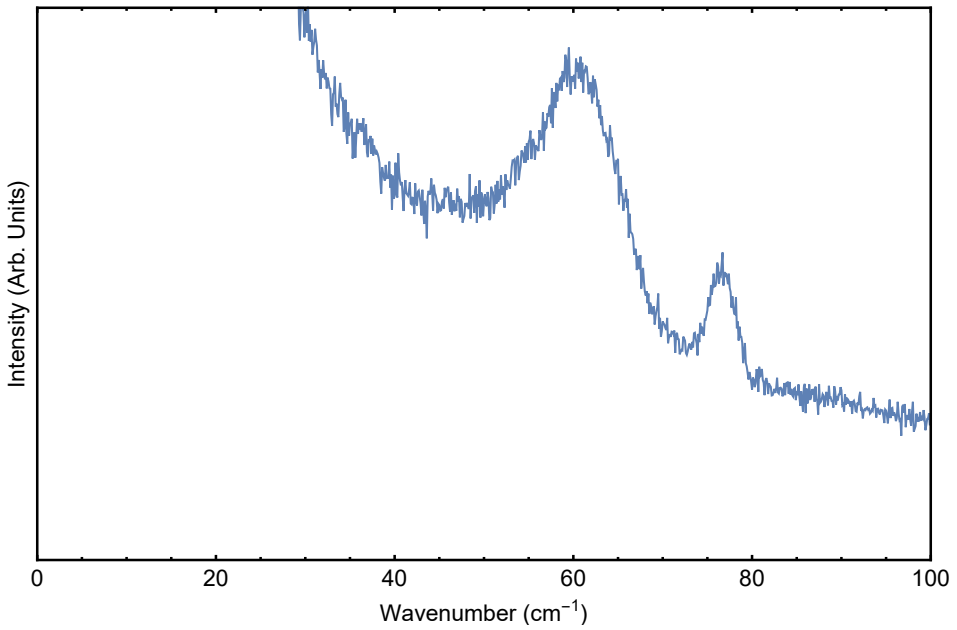

Figure A.21: Raman spectrum collected on PST ceramic #1 at 900°C, from Figure 4.11.

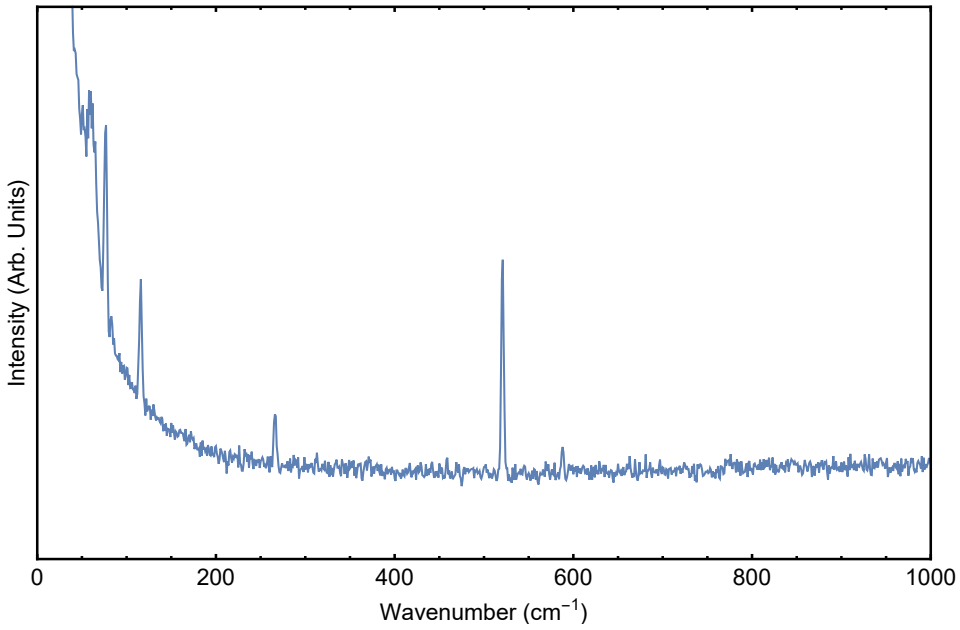

Figure A.22: Raman spectrum collected on PST ceramic #1 at 960°C, from Figure 4.10.

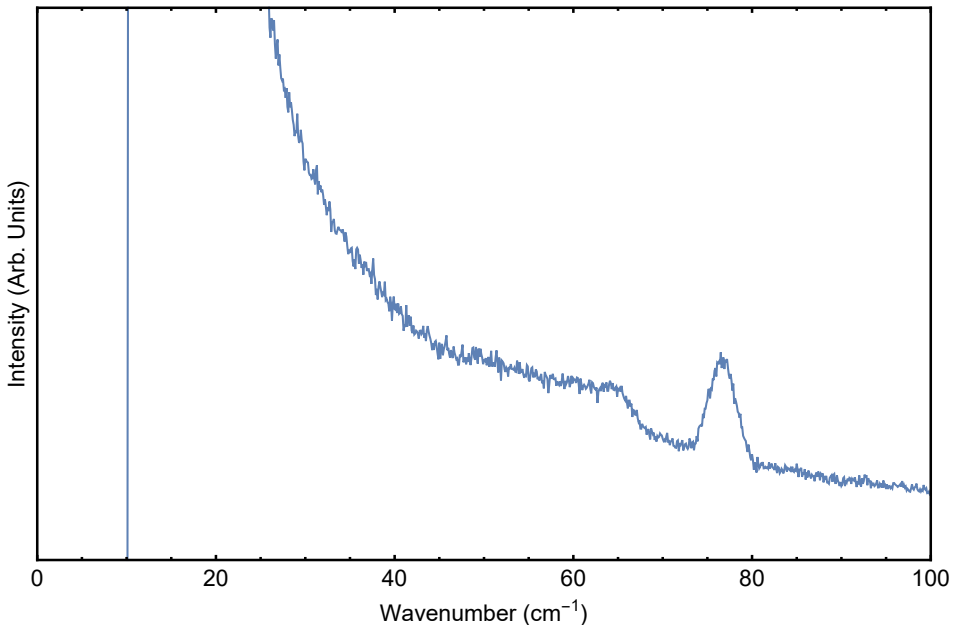

Figure A.23: Raman spectrum collected on PST ceramic #1 at 960°C, from Figure 4.11.

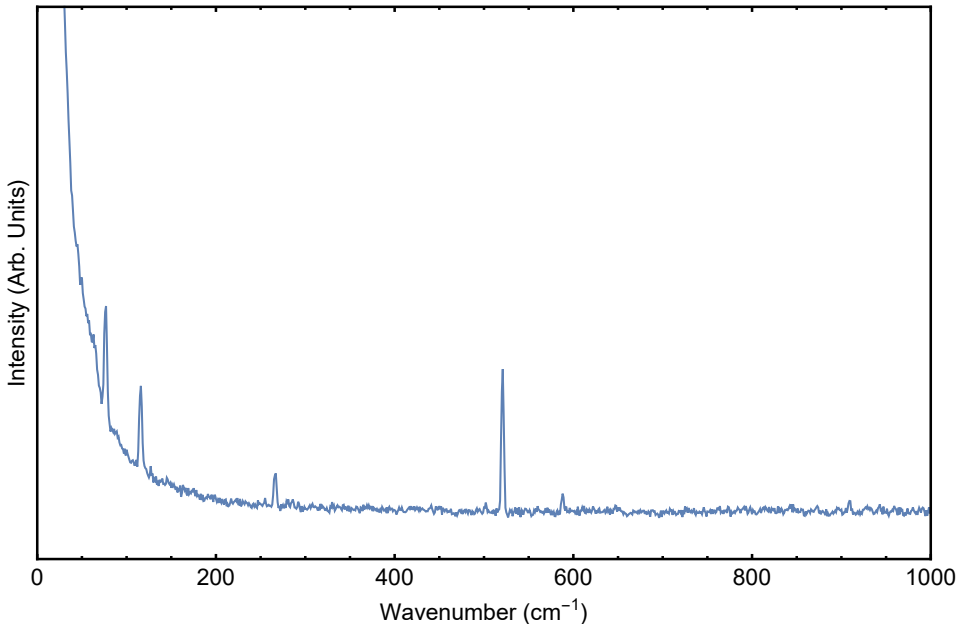

Figure A.24: Raman spectrum collected on PST ceramic #1 at 990°C, from Figure 4.10.

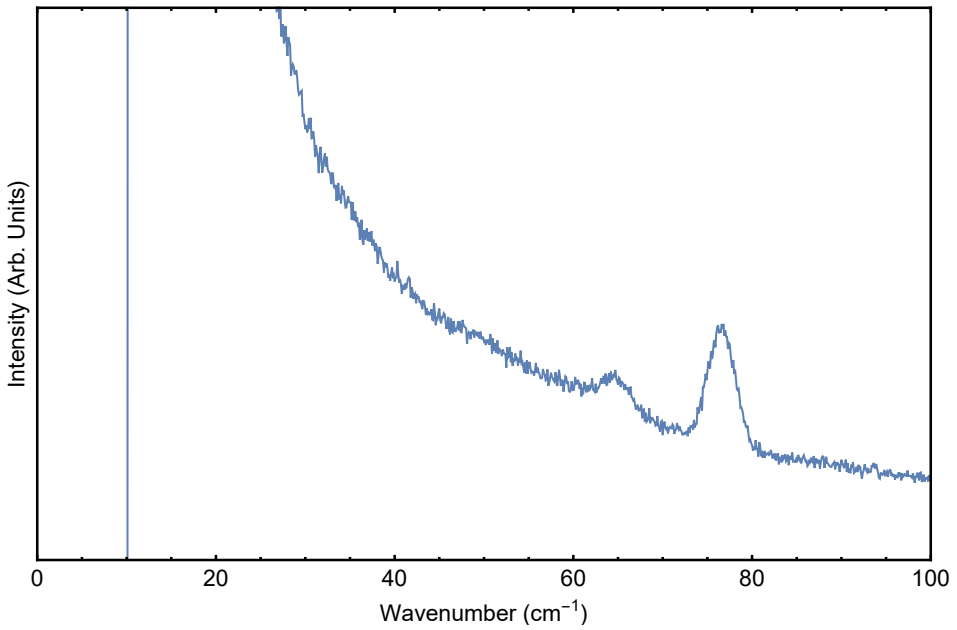

Figure A.25: Raman spectrum collected on PST ceramic #1 at 900°C, from Figure 4.11.

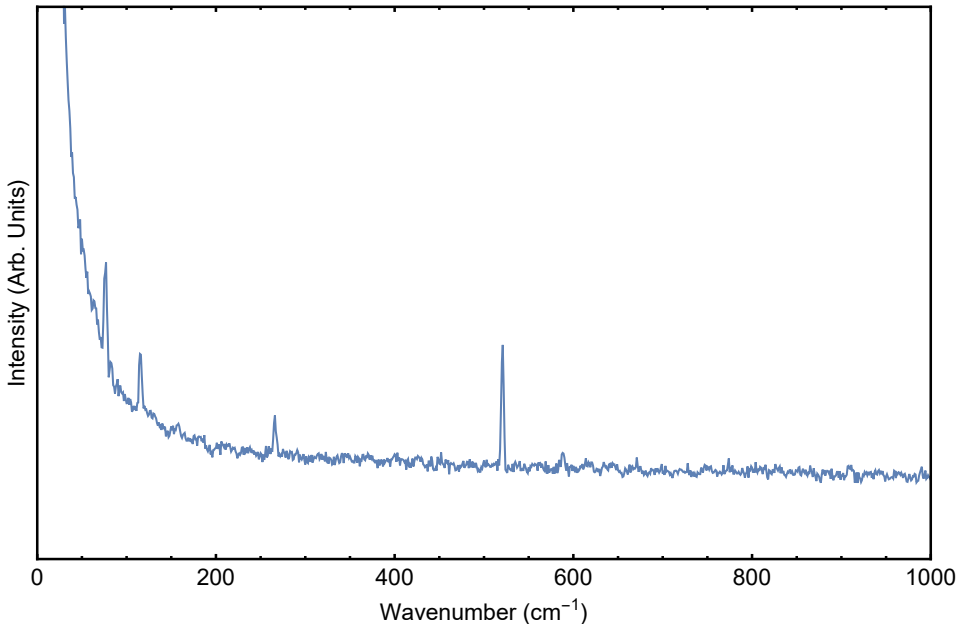

Figure A.26: Raman spectrum collected on PST ceramic #1 at 1050°C, from Figure 4.10.

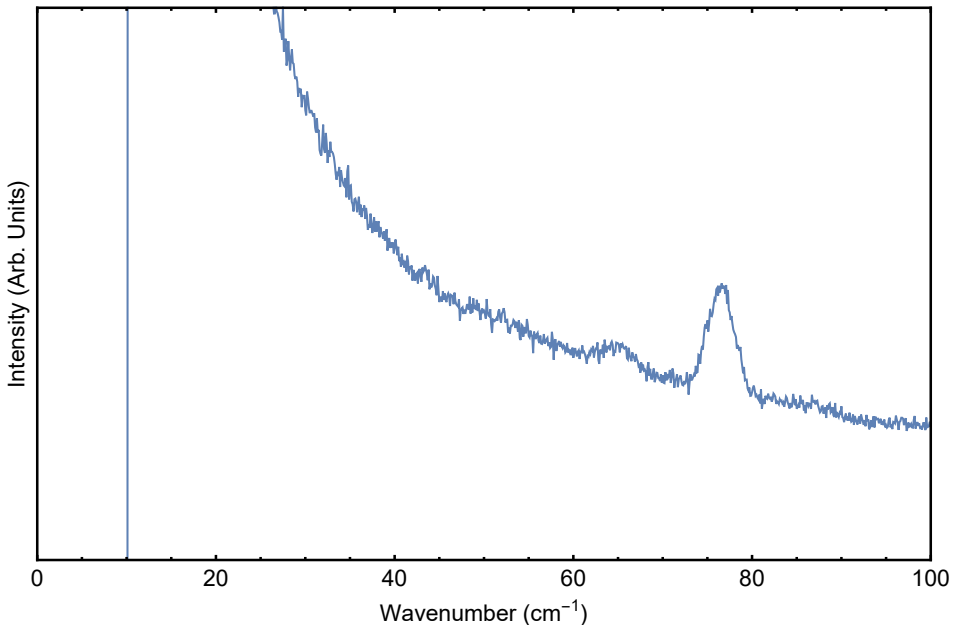

Figure A.27: Raman spectrum collected on PST ceramic #1 at 1050°C, from Figure 4.11.

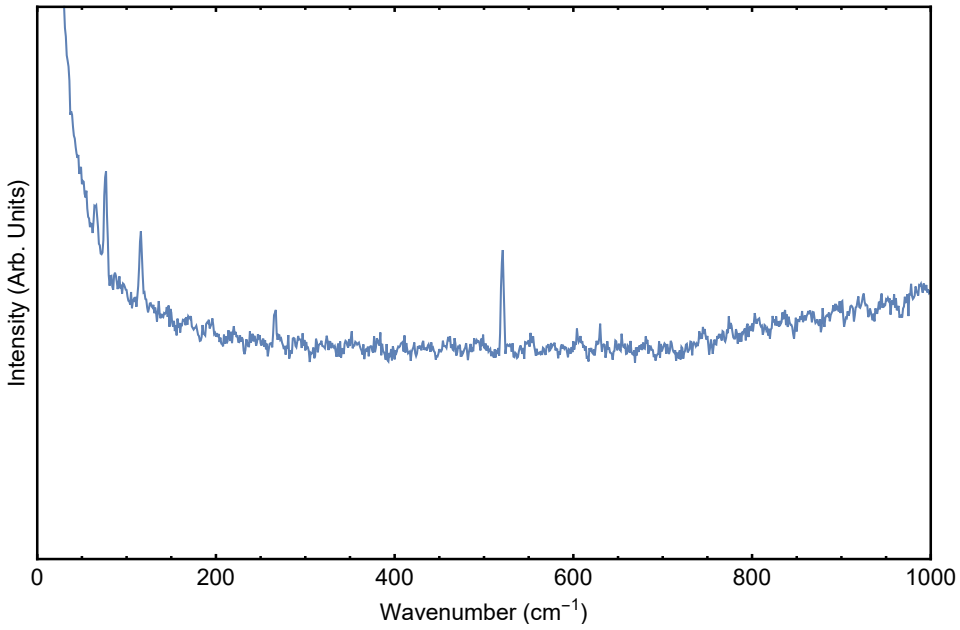

Figure A.28: Raman spectrum collected on PST ceramic #1 at 1100°C, from Figure 4.10.

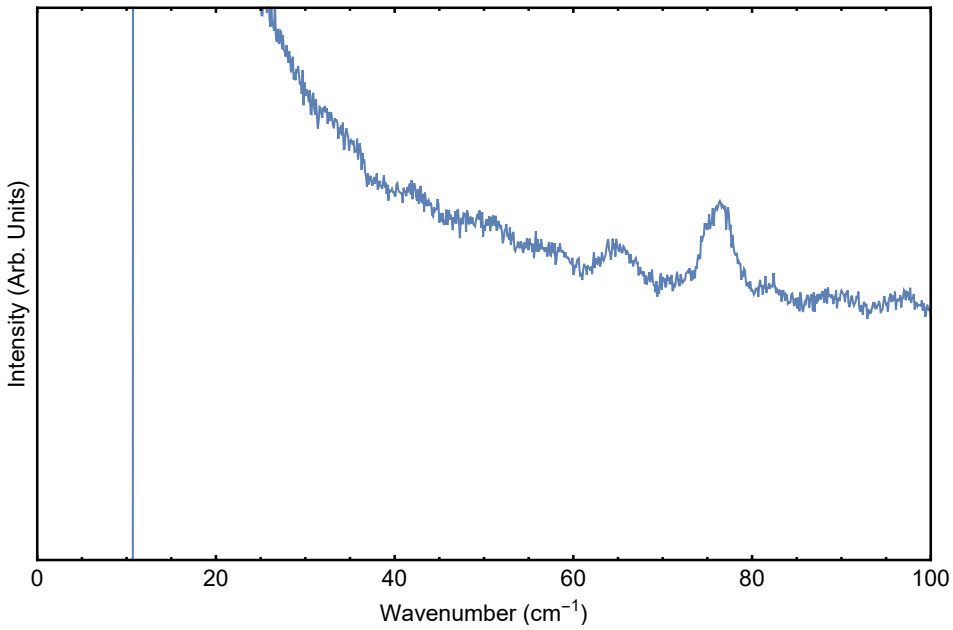

Figure A.29: Raman spectrum collected on PST ceramic #1 at 1100°C, from Figure 4.11.

Appendix B

PST#2 Spectra

B.1 Brillouin Spectra

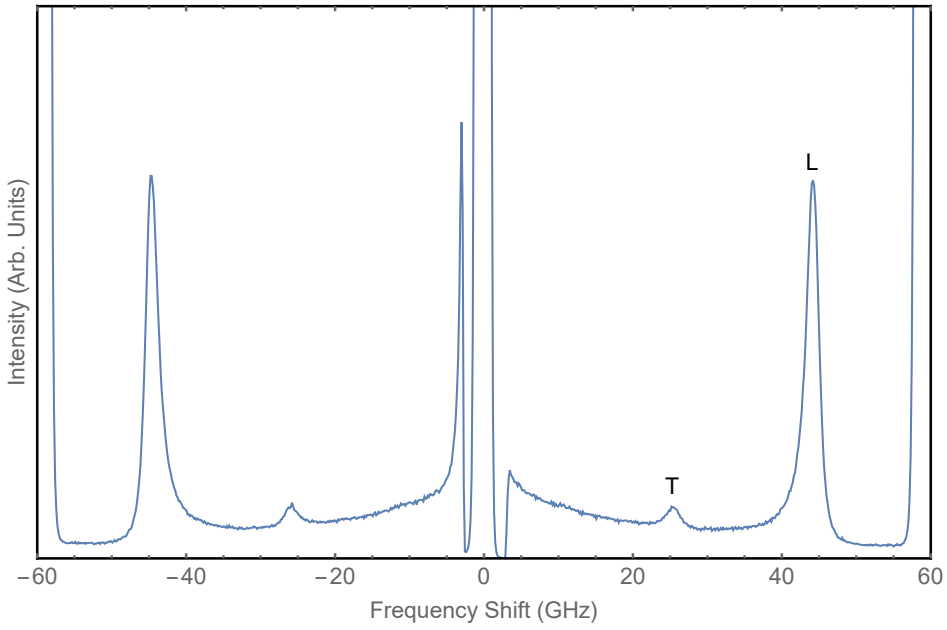

Figure B.1: Brillouin spectrum collected on PST ceramic #2 with an angle of incidence of 20°, from Figure 4.3.

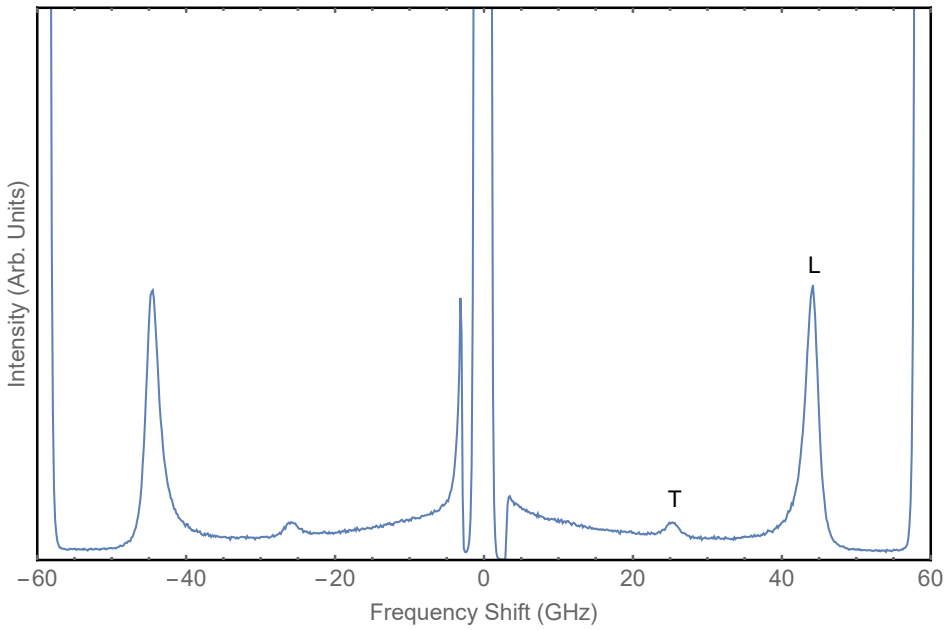

Figure B.2: Brillouin spectrum collected on PST ceramic #2 with an angle of incidence of 30°, from Figure 4.3.

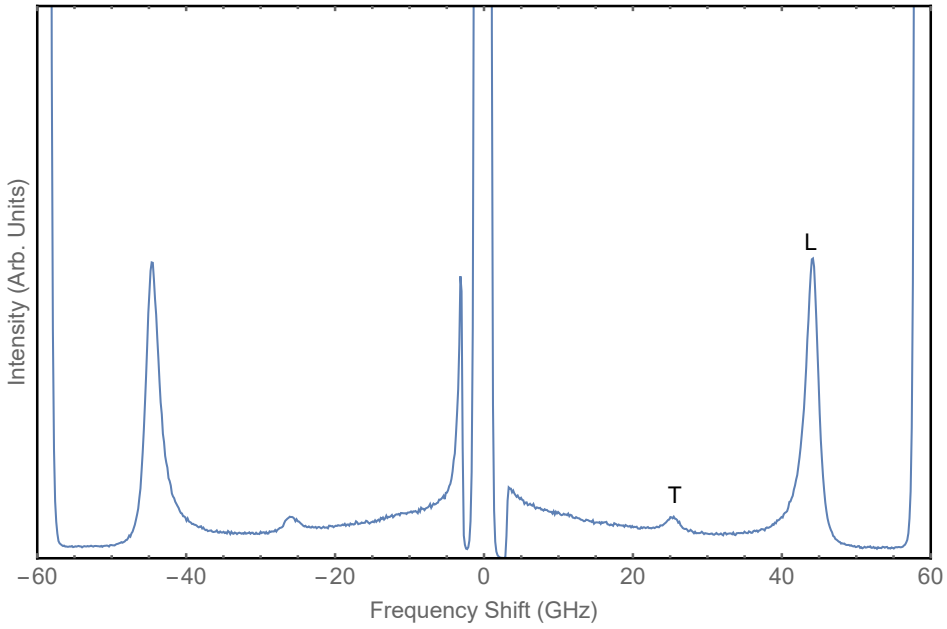

Figure B.3: Brillouin spectrum collected on PST ceramic #2 with an angle of incidence of 40°, from Figure 4.3.

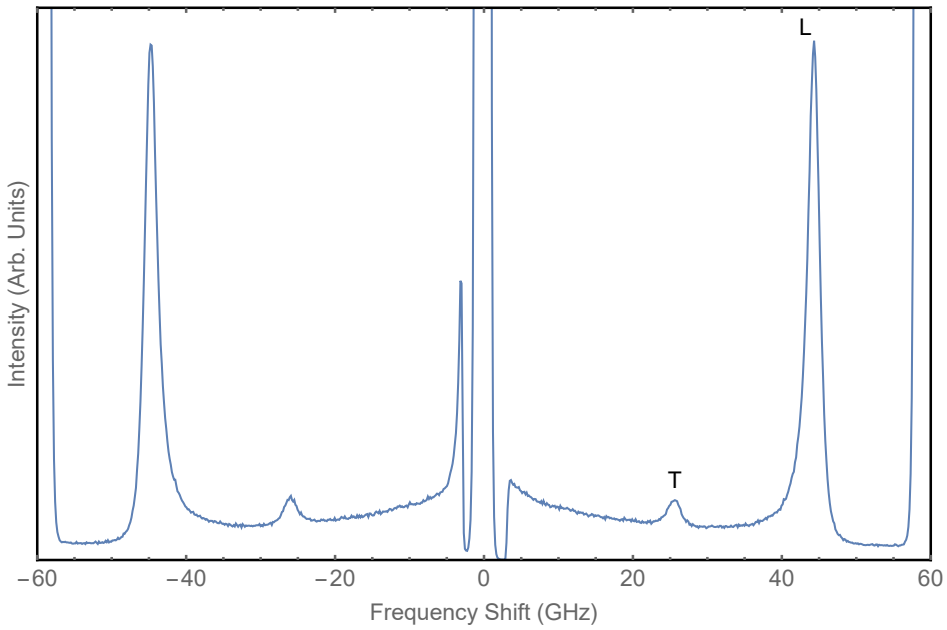

Figure B.4: Brillouin spectrum collected on PST ceramic #2 with an angle of incidence of 50°, from Figure 4.3.

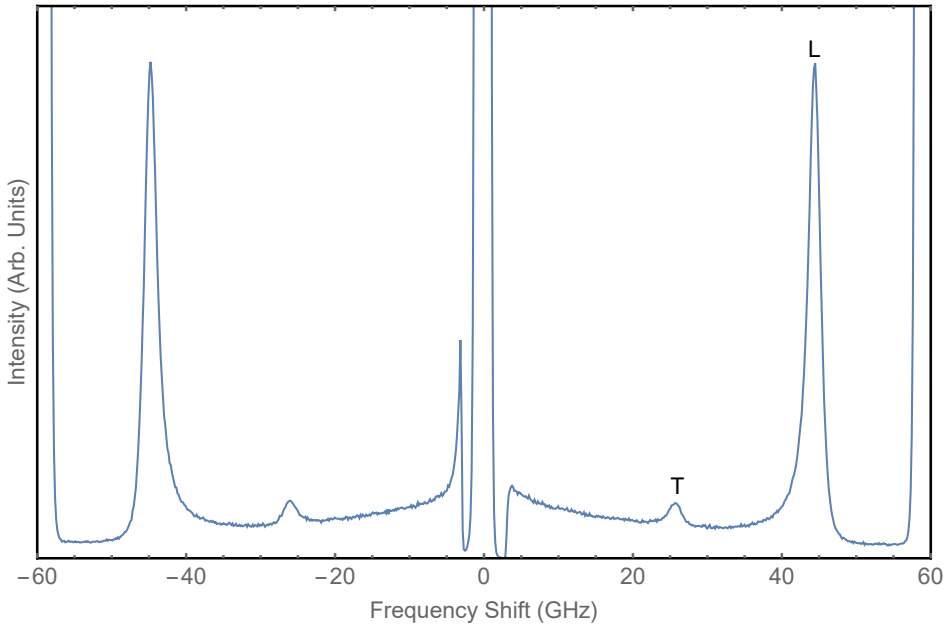

Figure B.5: Brillouin spectrum collected on PST ceramic #2 with an angle of incidence of 60°, from Figure 4.3.

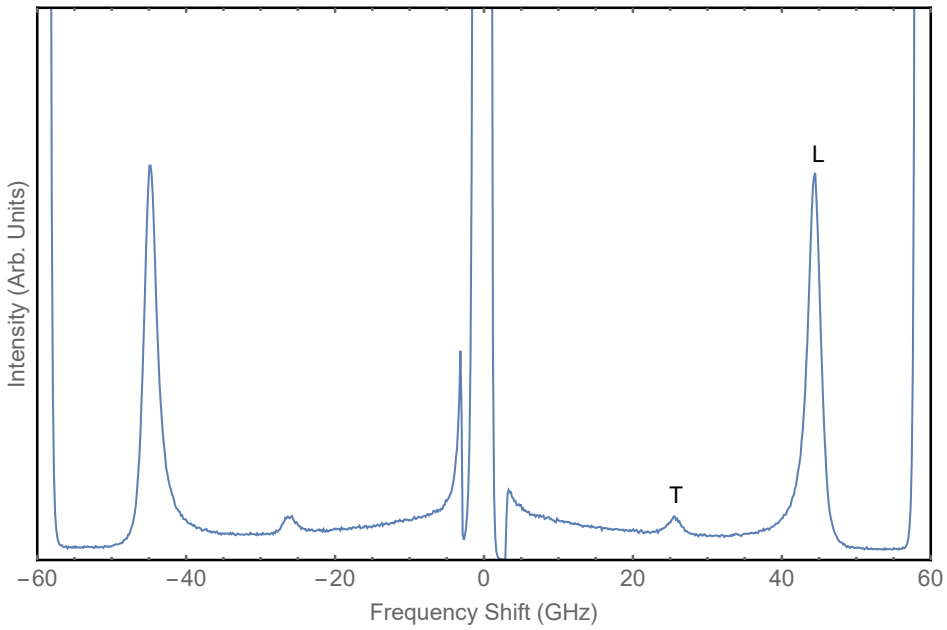

Figure B.6: Brillouin spectrum collected on PST ceramic #2 with an angle of incidence of 70°, from Figure 4.3.

B.2 Raman Spectra

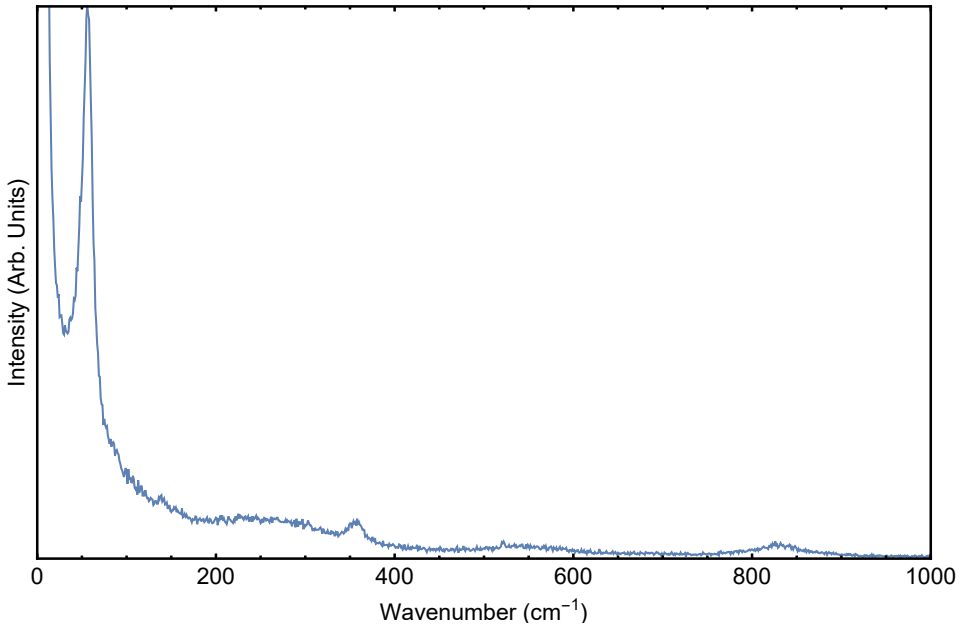

Figure B.7: Raman spectrum collected on PST ceramic #3 at 201°C, from Figure 4.17.

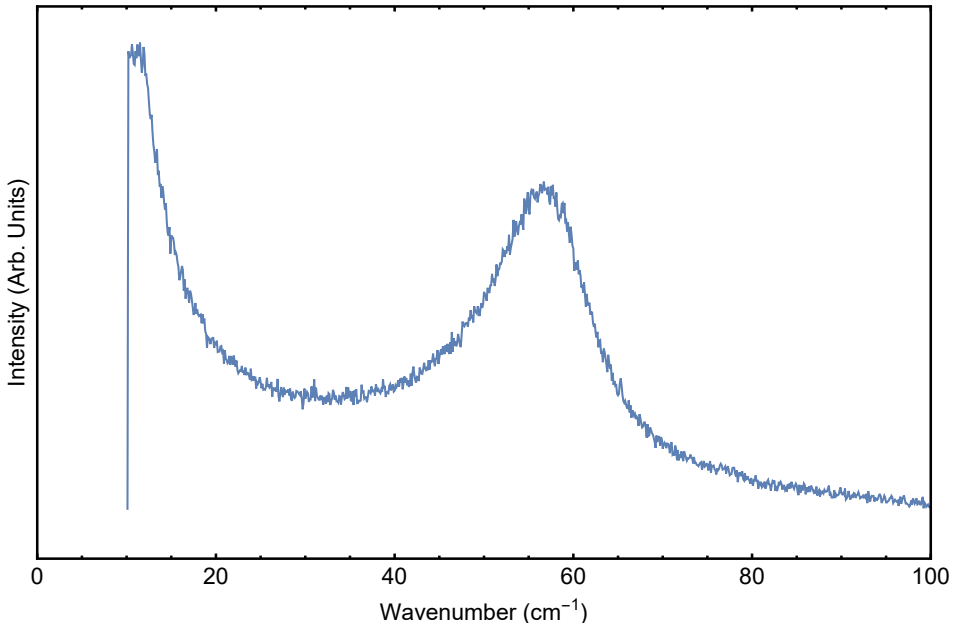

Figure B.8: Raman spectrum collected on PST ceramic #3 at 201°C, from Figure 4.18.

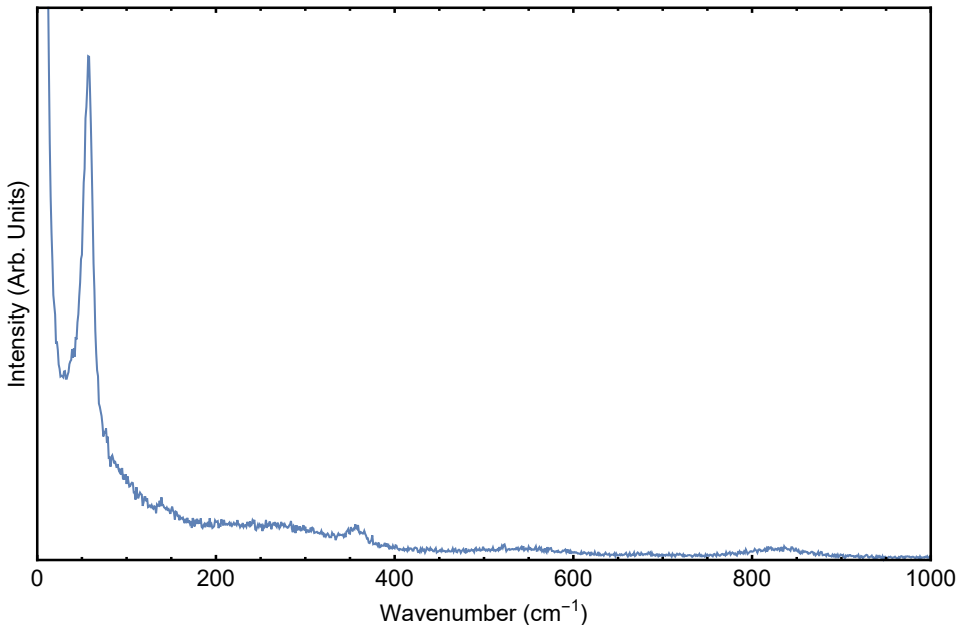

Figure B.9: Raman spectrum collected on PST ceramic #3 at 274°C, from Figure 4.17.

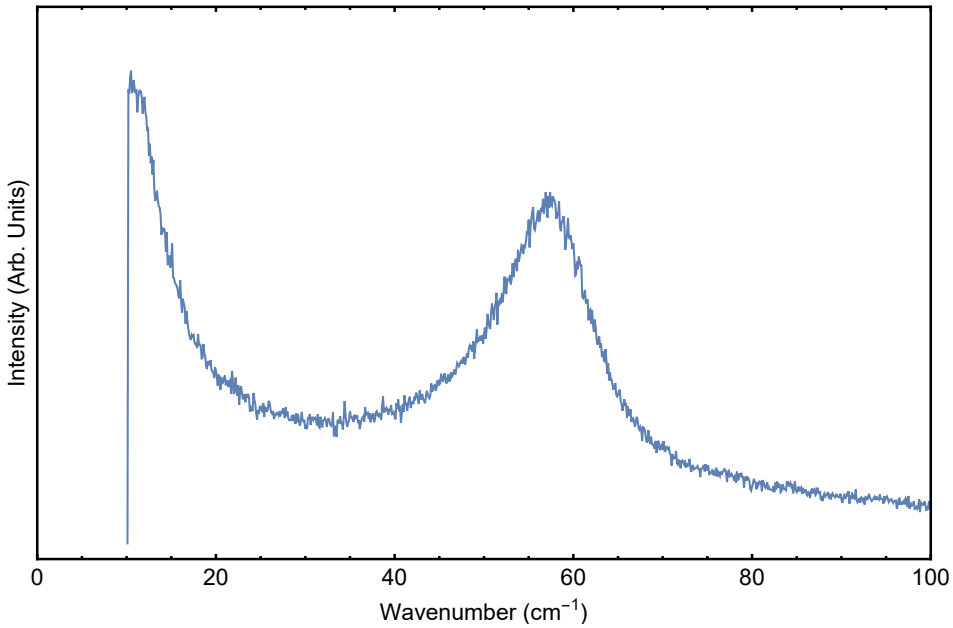

Figure B.10: Raman spectrum collected on PST ceramic #3 at 274°C, from Figure 4.18.

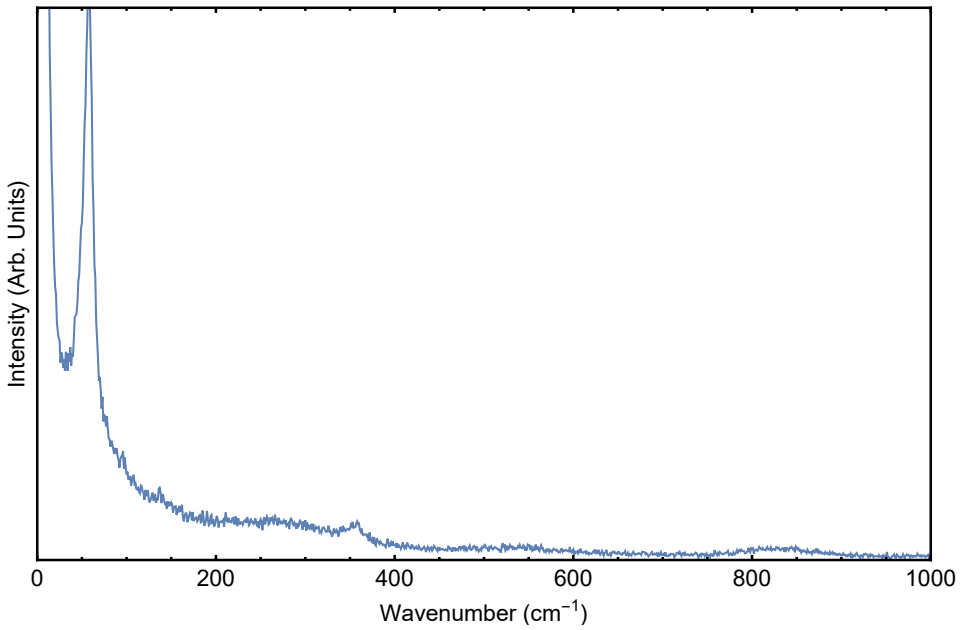

Figure B.11: Raman spectrum collected on PST ceramic #3 at 340°C, from Figure 4.17.

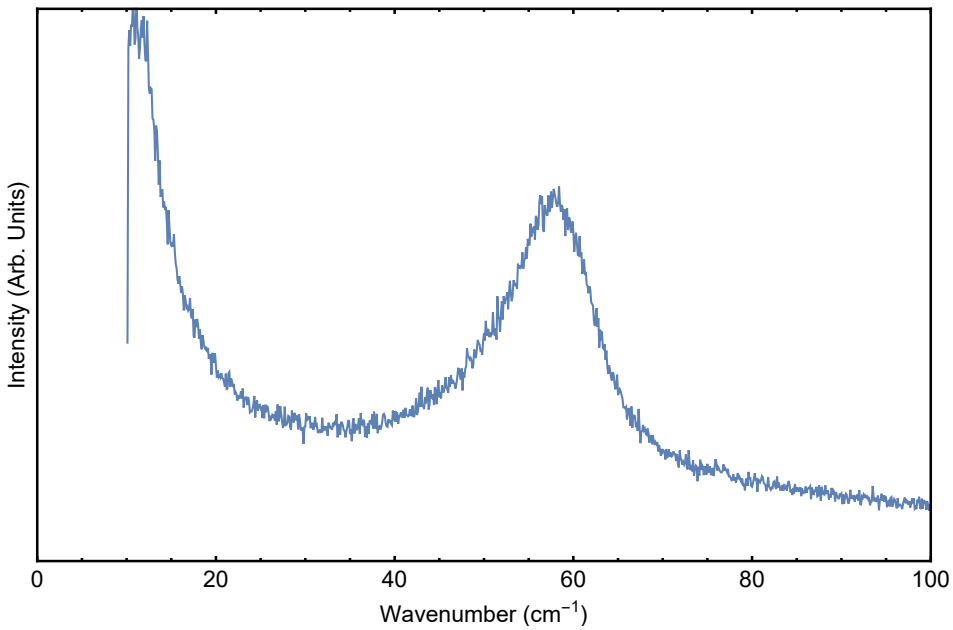

Figure B.12: Raman spectrum collected on PST ceramic #3 at 340°C, from Figure 4.18.

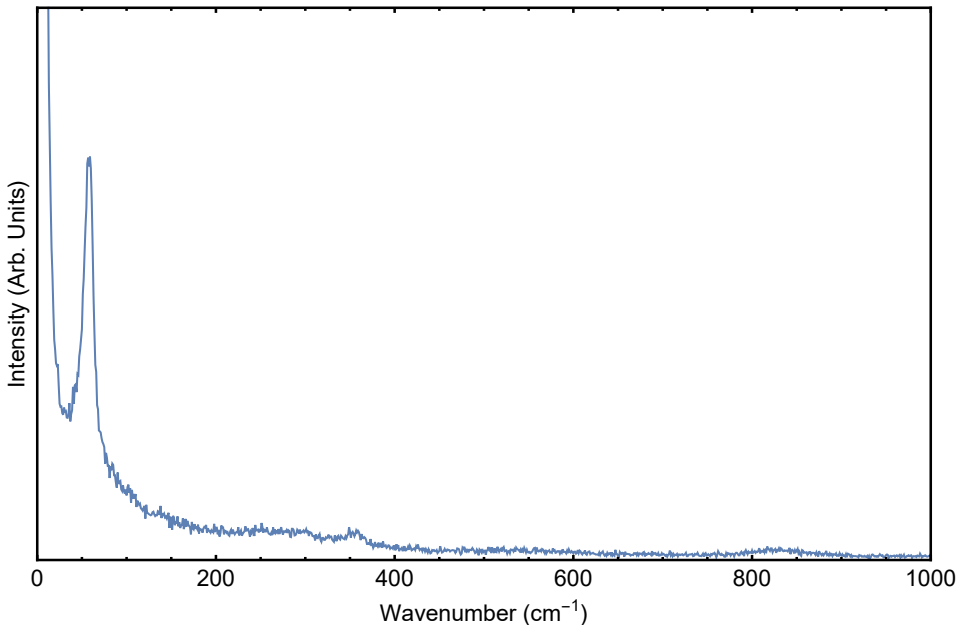

Figure B.13: Raman spectrum collected on PST ceramic #3 at 397°C, from Figure 4.17.

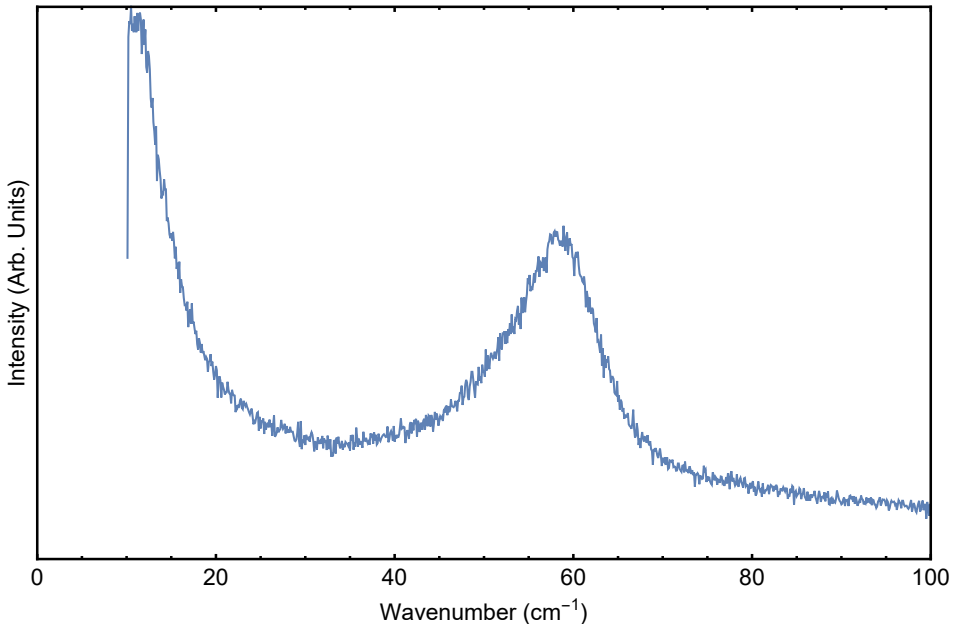

Figure B.14: Raman spectrum collected on PST ceramic #3 at 397°C, from Figure 4.18.

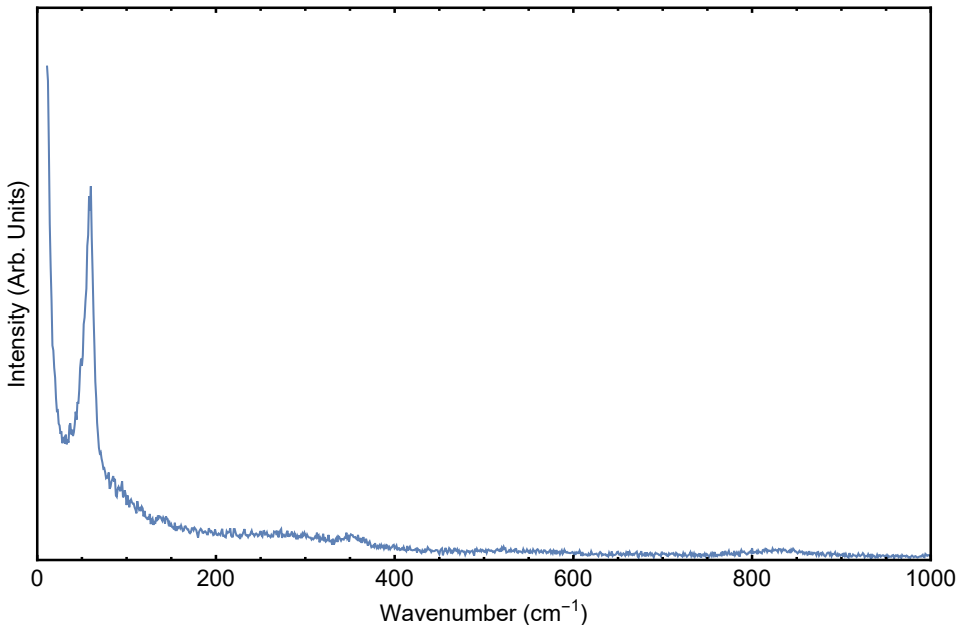

Figure B.15: Raman spectrum collected on PST ceramic #3 at 453°C, from Figure 4.17.

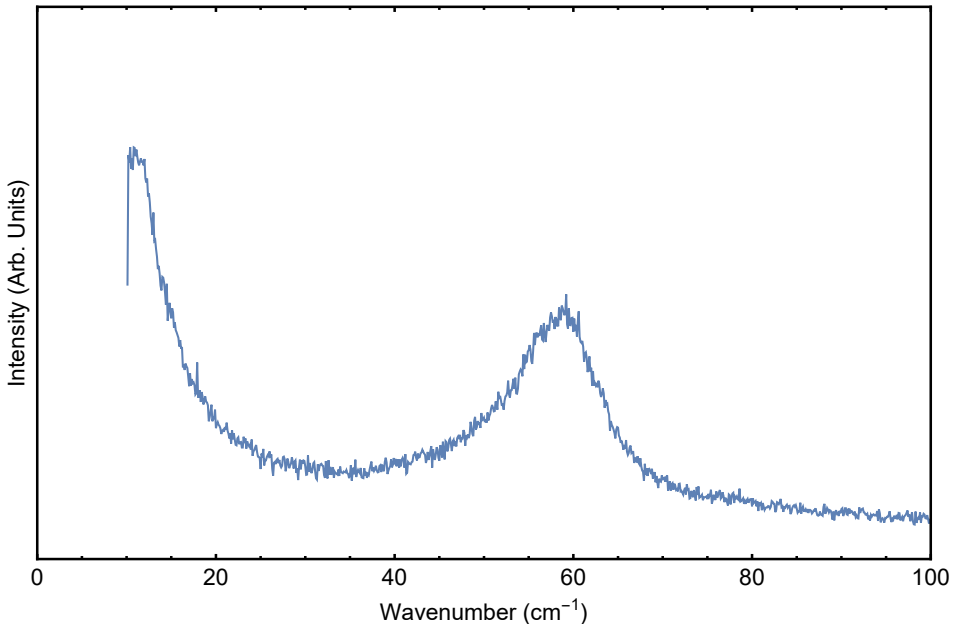

Figure B.16: Raman spectrum collected on PST ceramic #3 at 453°C, from Figure 4.18.

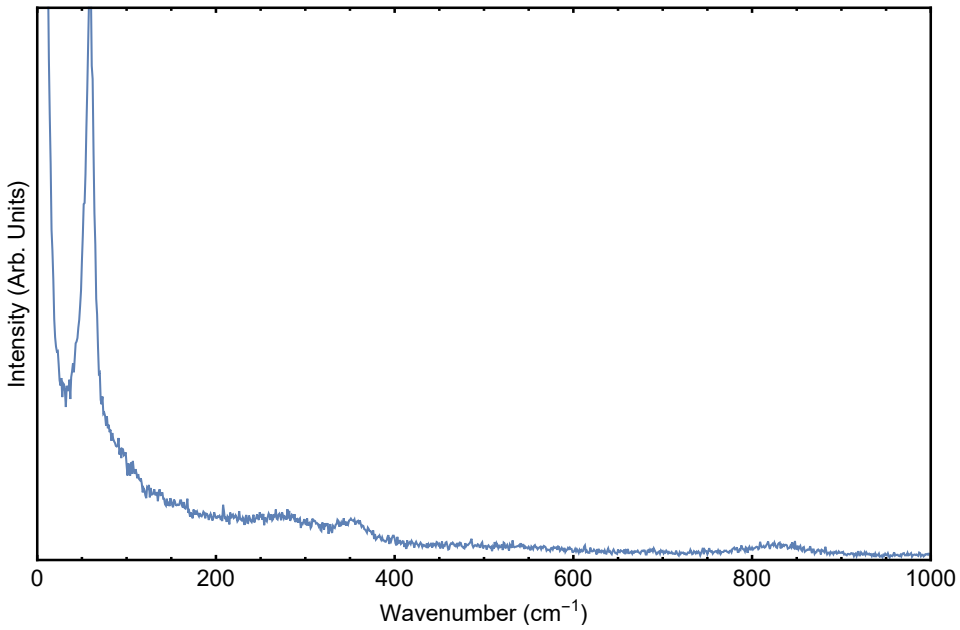

Figure B.17: Raman spectrum collected on PST ceramic #3 at 517°C, from Figure 4.17.

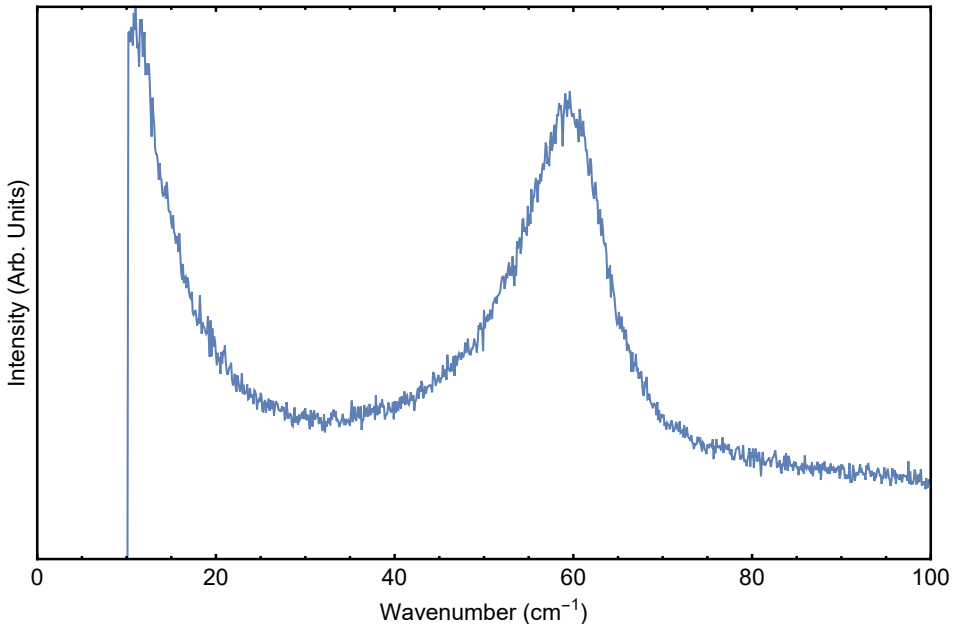

Figure B.18: Raman spectrum collected on PST ceramic #3 at 517°C, from Figure 4.18.

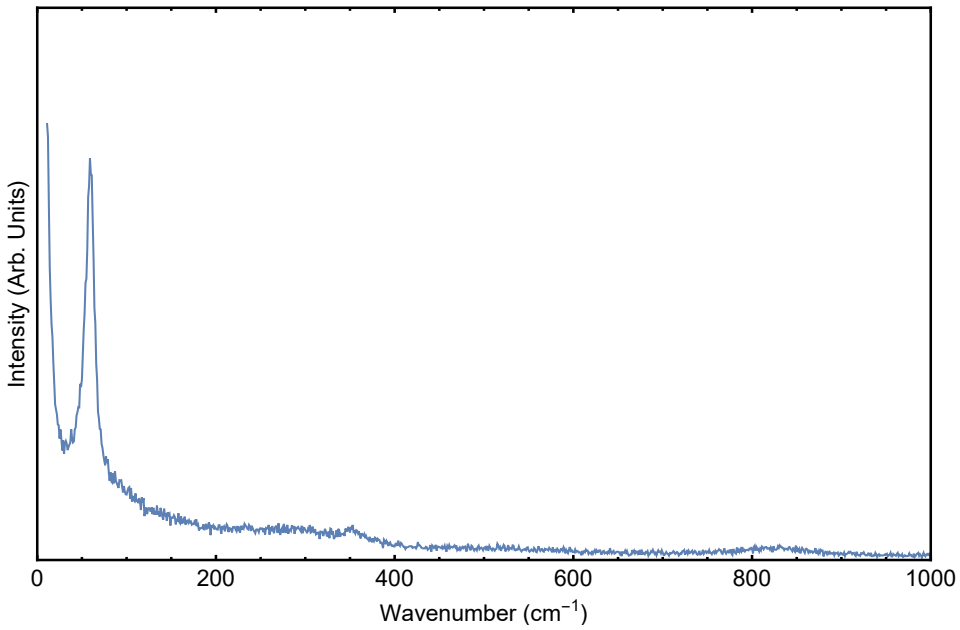

Figure B.19: Raman spectrum collected on PST ceramic #3 at 572°C, from Figure 4.17.

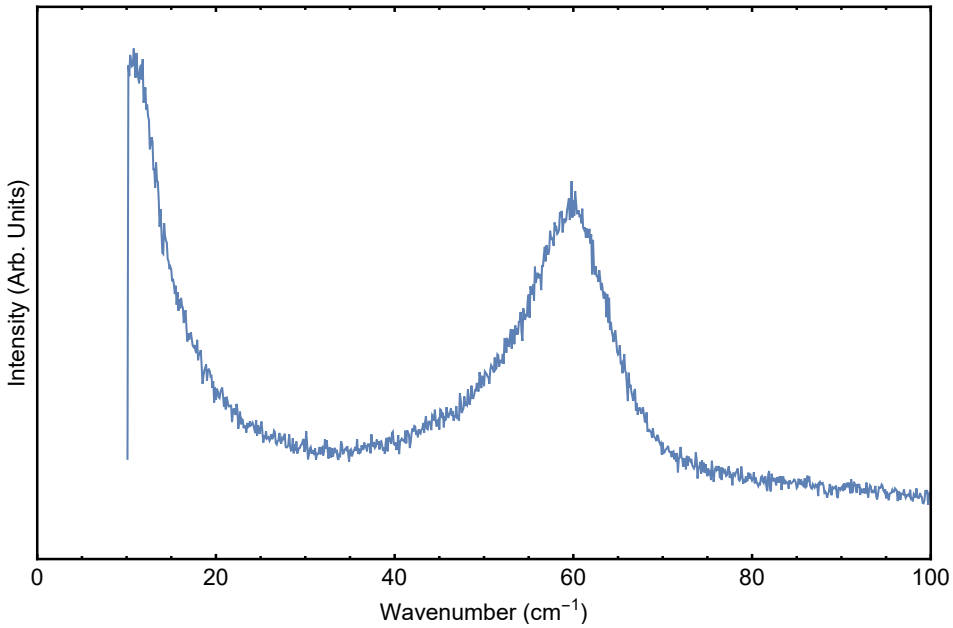

Figure B.20: Raman spectrum collected on PST ceramic #3 at 572°C, from Figure 4.18.

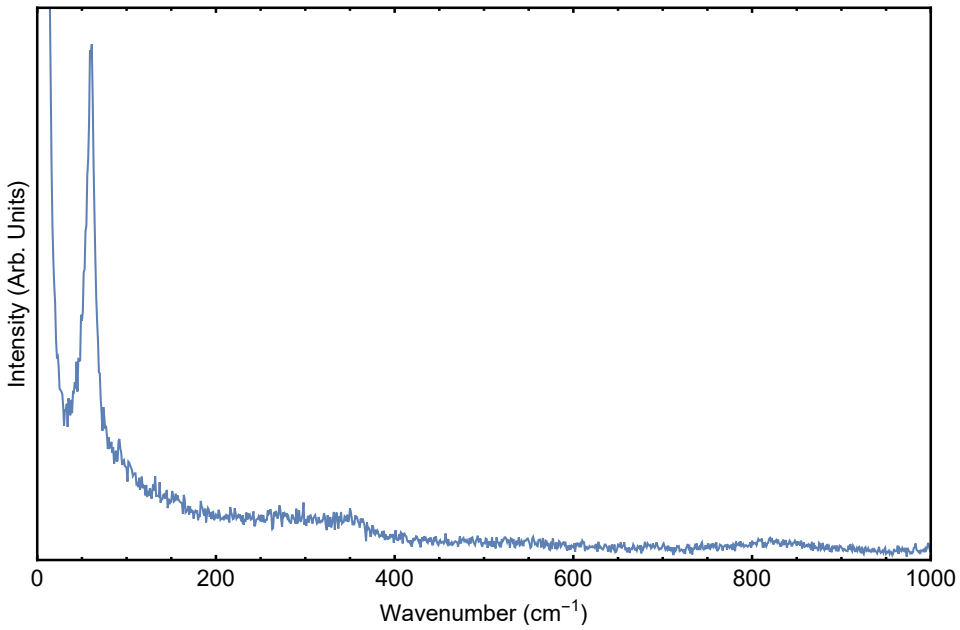

Figure B.21: Raman spectrum collected on PST ceramic #3 at 624°C, from Figure 4.17.

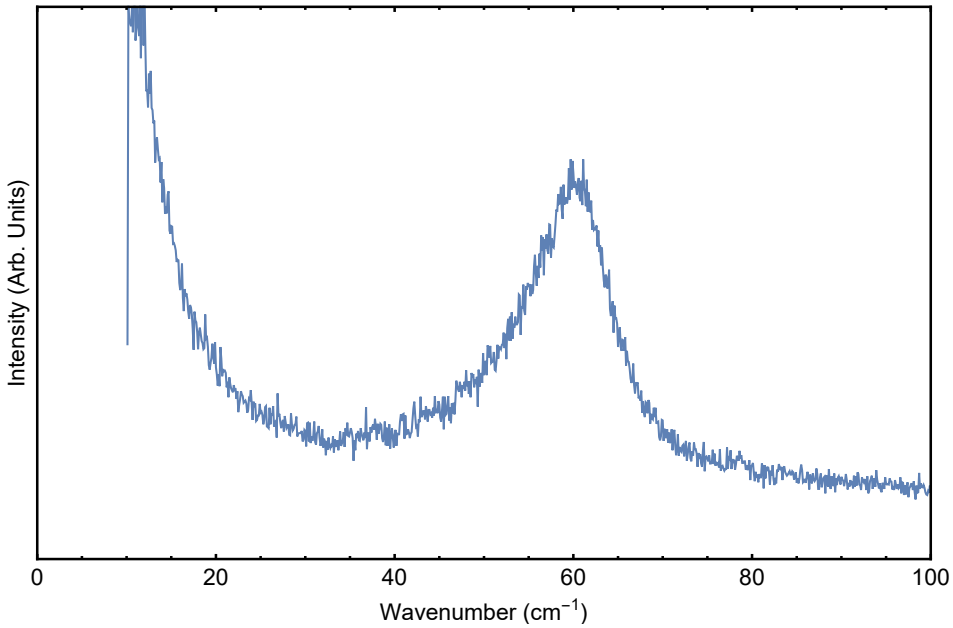

Figure B.22: Raman spectrum collected on PST ceramic #3 at 624°C, from Figure 4.18.

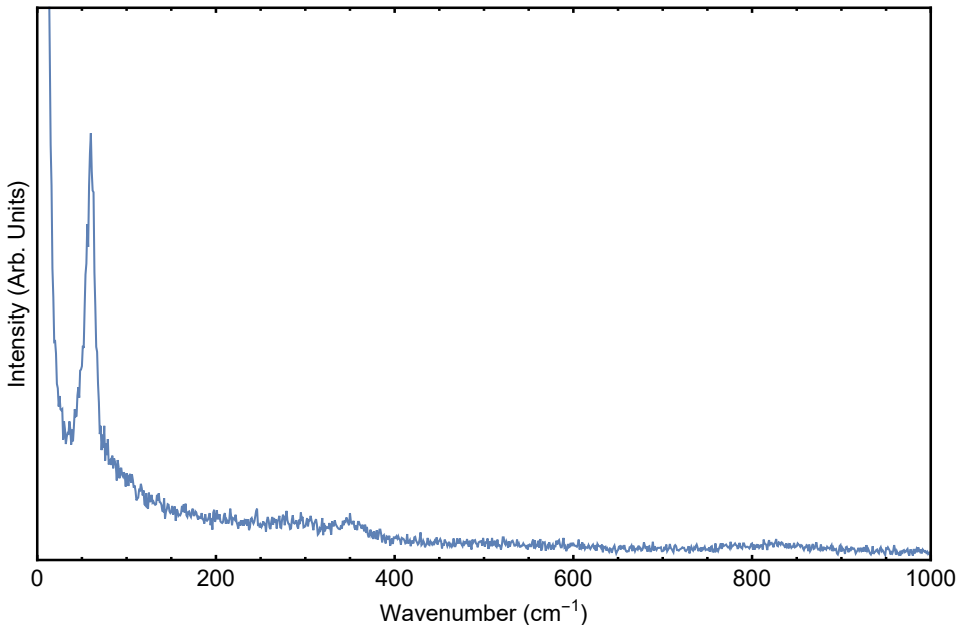

Figure B.23: Raman spectrum collected on PST ceramic #3 at 653°C, from Figure 4.17.

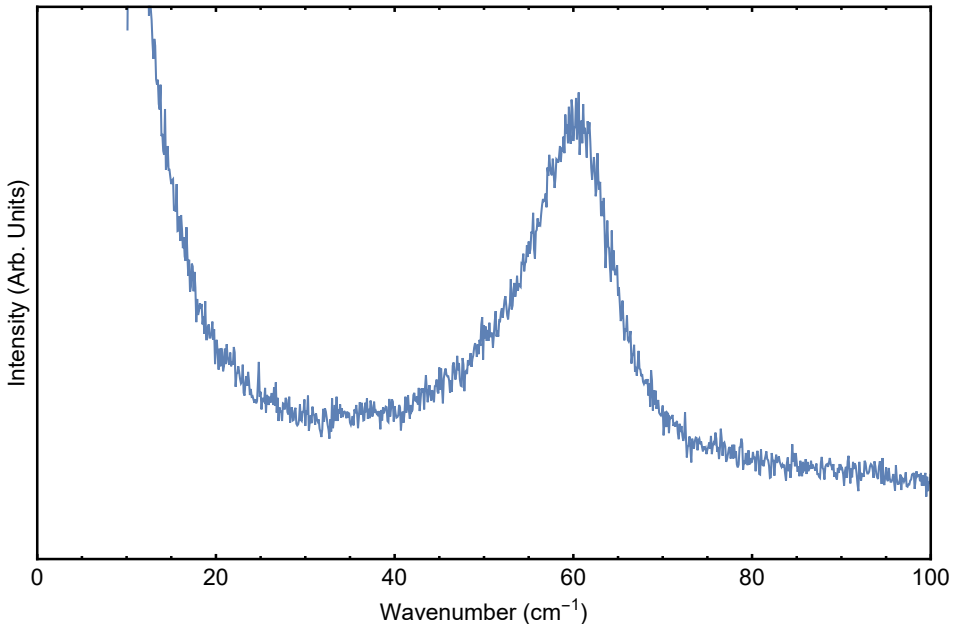

Figure B.24: Raman spectrum collected on PST ceramic #3 at 653°C, from Figure 4.18.

Bibliography

[1] AI Fedoseev, SG Lushnikov, SN Gvasaliya, and S Kojima. *Physics of the Solid State*, 48(6):1102–1105, 2006.

[2] CGF Stenger and AJ Burggraaf. *Physica Status Solidi A: Applied Research*, 61(1):275–285, 1980.

[3] E Salje and U Bismayer. *Journal of Physics: Condensed Matter*, 1(39):6967, 1989.

[4] P Groves. *Journal of Physics C: Solid State Physics*, 18(34):L1073, 1985.

[5] H Wang and W Schulze. *Journal of the American Ceramic Society*, 73(5):1228–1234, 1990.

[6] N Setter and LE Cross. *Journal of Applied Physics*, 51(8):4356–4360, 1980.

[7] A Fundora, A Vázquez, J Portelles, F Calderón, and JM Siqueiros. *Journal of Non-Crystalline Solids*, 235:567–569, 1998.

[8] NM Shorrocks, RW Whatmore, and PC Osbond. *Ferroelectrics*, 106(1):387–392, 1990.

[9] LS Kamzina and AL Korzhenevskii. *Ferroelectrics*, 131(1):91–95, 1992.

[10] A Pietraszko, A Trzaskowska, A Hilczer, and Z Tylczyński. *Ferroelectric Letters*, 34(5-6):139–148, 2007.

[11] N Setter and LE Cross. *Journal of Materials Science*, 15(10):2478–2482, 1980.

[12] M Harmer, A Bhalla, B Fox, and LE Cross. *Materials Letters*, 2(4):278–279, 1984.

[13] L Eric Cross. *Ferroelectrics*, 151(1):305–320, 1994.

[14] U Bismayer, V Devarajan, and P Groves. *Journal of Physics: Condensed Matter*, 1(39):6977, 1989.

[15] CGF Stenger and AJ Burggraaf. *Physica Status Solidi (a)*, 61(2):653–664, 1980.

[16] F Jiang, J Ko, S Lushnikov, and S Kojima. *Japanese Journal of Applied Physics*, 40(9S):5823, 2001.

[17] SG Lushnikov, FM Jiang, and S Kojima. *Solid State Communications*, 122(3):129–133, 2002.

[18] B Mihailova, U Bismayer, B Güttler, M Gospodinov, and L Konstantinov. *Journal of Physics: Condensed Matter*, 14(5):1091, 2002.

[19] N Setter and I Laulicht. *Applied Spectroscopy*, 41(3):526–528, 1987.

[20] B Mihailova, B Maier, C Paulmann, T Malcherek, J Ihringer, M Gospodinov, R Stosch, B Güttler, and U Bismayer. *Physical Review B*, 77(17):174106, 2008.

[21] A Patel. In *Ferroelectric Thin Films II: Symposium Held December 2-4, 1991, Boston, Massachusetts, USA*, volume 243, page 67. Cambridge Univ Press, 1992.

[22] M Born and K Huang. *Dynamic Theory of Crystal Lattice, Clarendon*. Oxford, 1954.

[23] MP Marder. *Condensed Matter Physics*. John Wiley & Sons, 2010.

[24] H. Z. Cummings and P. E. Schoen. *Light Scattering from Thermal Fluctuations*, volume 2. John Wiley and Sons, North-Holland, New York, 1972.

[25] LD Landau and EM Lifshitz. *Course of Theoretical Physics*, volume 7. Elsevier, 2013.

[26] W Hayes and R Loudon. *Scattering of Light by Crystals*. Courier Corporation, 1978.

[27] A. Yariv and P. Yeh. *Photonics: Optical Electronics in Modern Communications*, volume 2. Oxford University Press, Oxford, United Kingdom, 2007.

[28] B.E.A. Saleh and M.C. Teich. *Fundamentals of Photonics*. Wiley, 1991.

[29] FL Pedrotti, LS Pedrotti, and LM Pedrotti. *Introduction to Optics*. 2007.

[30] K. Akintola. Phonon Dynamics of Exotic Materials $Bi_2 2Se_3$, Bi_2Te_3, Sb_2Te_3 and WSe_2. Master's thesis, Memorial University of Newfoundland, Canada, 2012.

[31] PC Osbond and RW Whatmore. *Journal of Materials Science*, 28(5):1377–1384, 1993.

[32] B Mroz and S Mielcarek. *Journal of Physics D: Applied Physics*, 34(3):395, 2001.

[33] VI Zinenko, NG Zamkova, EG Maksimov, and SN Sofronova. *Journal of Experimental and Theoretical Physics*, 105(3):617–625, 2007.

[34] J Sandercock. *Solid State Communications*, 26:547–551, 1978.

[35] R Laiho, T Levola, SD Prokhorova, IG Siny, AK Tagantsev, and W Windsch. *Ferroelectrics*, 80(1):181–184, 1988.

[36] IG Siny and TA Smirnova. *Ferroelectrics*, 90(1):191–194, 1989.

[37] S Kamba, M Berta, M Kempa, J Petzelt, K Brinkman, and N Setter. *arXiv preprint cond-mat/0504755*, 2005.